Division of Pharmaceutical Chemistry and Technology
Faculty of Pharmacy
University of Helsinki
Finland

Non-linear Label-free Optical Imaging of Cells, Nanocrystal Cellular Uptake and Solid-State Analysis in Pharmaceutics

by

Jukka Saarinen

ACADEMIC DISSERTATION

To be presented, with the permission of the Faculty of Pharmacy of the University of Helsinki, for public examination in Auditorium 1041 at Biocenter 2 (Viikinkaari 5E, Helsinki) on March 2nd 2018, at 12.00 noon.

Helsinki 2018

Supervisors Associate Professor Clare J. Strachan
Division of Pharmaceutical Chemistry and Technology
Faculty of Pharmacy
University of Helsinki
Finland

Associate Professor Hélder A. Santos
Division of Pharmaceutical Chemistry and Technology
Faculty of Pharmacy
University of Helsinki
Finland

Docent Leena Peltonen
Division of Pharmaceutical Chemistry and Technology
Faculty of Pharmacy
University of Helsinki
Finland

Doctor Antti Isomäki
Biomedicum Imaging Unit
Faculty of Medicine
University of Helsinki
Finland

Reviewers Professor Andreas Zumbusch
Department of Chemistry
Physical Chemistry
University of Konstanz
Germany

Assistant Professor Andrea Heinz
Department of Pharmacy
Nanomedicine
University of Copenhagen
Denmark

Opponent Dr. ir. Herman Offerhaus
Optical Sciences Group
Department of Applied Physics
Twente University
The Netherlands

ISBN 978-951-51-4055-5 (Print)
ISBN 978-951-51-4056-2 (Online)
ISSN 2342-3161 (Print)
ISSN 2342-317X (Online)
Helsinki University Printing House Helsinki 2018

Abstract

In the pharmaceutical industry, novel microscopy analytical techniques are required, especially in the preclinical phases of drug development, to gain important insights about new drug candidates and their formulations as early as possible. This information can be used to develop more efficient, safe and also economically profitable medicines.

Nanoparticles are often used nowadays in drug development to achieve, for example, targeted drug delivery for cancer treatment. Therefore, suitable imaging techniques are crucial to image the fate of these nanoparticles in cells and tissues and ensure the safety and efficient use of these nanomedicines. On the other hand, pharmaceutical solid-state forms also play an important role in drug development. New active pharmaceutical ingredient (API) molecules tend to be poorly water-soluble. By using so called amorphous forms, in which the API molecules are not organized in a repeated unit cell (as is the case for crystalline material), it is possible to achieve faster dissolution. However, amorphous forms tend to crystallize over time. Therefore solid-state monitoring of the API is very important in drug development and during storage. In this Thesis, the overall aim was to evaluate the capability of non-linear optical imaging, especially coherent anti-Stokes Raman scattering (CARS), second harmonic generation and more generally sum-frequency generation (SHG and SFG) microscopies, in the above-mentioned pharmaceutical applications including imaging of live cells, nanoparticle cellular uptake and pharmaceutical solid-state analysis.

First, the capability of CARS microscopy to image live cell cultures on pharmaceutically relevant membrane inserts was evaluated. These cell cultures are used in drug permeability studies. It was found that, label-free CARS microscopy can be used to image Caco-2 cells grown on PTFE inserts in a non-destructive manner. CARS imaging was also used to probe lipid droplets in cells. The number and size of the lipid droplets increased substantially over a 21-day culturing period, which is important in the context of drug permeation studies, since lipid content of the cells will influence drug permeation.

Cellular uptake of non-fluorecent drug nanocrystals was subsequently investigated using CARS microscopy. CARS microscopy was successfully used to probe nanocrystals in cells in a label-free and chemically-specific manner. The analytical technique was further developed by combining CARS microscopy with transmission electron microscopy to form a correlative coherent anti-Stokes Raman scattering (CARS) and electron microscopy (C-CARS-EM) platform that was used to image exactly the same cells with both of the techniques. By using this method, drug nanocrystals could be chemically-specifically probed in the cells utilizing CARS microscopy and EM was used to reveal the subcellular localization of the internalized nanocrystals with (sub)nanometer spatial resolution.

In the final study, multimodal CARS and SHG/SFG imaging was used to visualize the distribution of amorphous, gamma and alpha indomethacin on tablet surfaces. Further, the same techniques were successfully used to follow the surface crystallization of amorphous indomethacin with high sensitivity. The combined use of CARS and SHG in a single instrument can improve image interpretation confidence, since the two non-linear microscopy methods, relying on different mechanisms (detection of molecular vibrations (CARS) and SFG signal produced by non-centrosymmetric crystals), can support each other.

In summary, it was demonstrated that non-linear optical imaging can be a very useful tool in pharmaceutical applications including imaging of live cells, nanoparticle cellular uptake and solid-state analysis. The results were obtained by using a commercially available microscope, which suggests that there is plenty of potential in these techniques to be applied on a wider scale. The use of these techniques is likely to increase with further instrument commercialization in the near future.

Acknowledgements

Now that the scientific part of the Thesis is ready, it is time to sit down with a cup of coffee, while listening to "Smoke on the Water" and write the Acknowledgements. I have now spent approximately 10 years in the Faculty of Pharmacy. I remember when I was starting my Master's Thesis and I went to talk with Professor Jouko Yliruusi, who directed me to talk to Professor Clare Strachan. Jouko explained that Clare is from New Zealand. I was a bit worried about my English, but I understood something about the project description — it involved CARS imaging of cells. Well, that sounded interesting and the road led to this point. It must have been a good choice, I guess. After all, I still have my strong accent in English, but I have learnt that it doesn't matter. Everybody speaks English in the scientific world differently.

At the beginning of my PhD studies I had e-mail discussions with the doctoral program coordinator. He told me to think twice before starting a PhD. According to him it would be a very frustrating path. Plenty of long days with a slave salary and most of the experiments going wrong and so on he continued. He was right and already at that time I kind of had a feeling of what it was going to be like. And to be honest, I had some difficult times during this project. However, as my mother told me once, I have never said I will quit. Well, I think I have said that many times, but not seriously. Sometimes (actually quite often), I have thought, what is the point of all this. Then I realize that it is actually pretty cool to achieve a doctoral degree. I have always aimed for that basically just for myself. Wouldn't it be nice to be a rock star like Brian May and still have a doctoral degree.

After all, it has been a nice opportunity to do my PhD at the University of Helsinki in the Doctoral Program in Drug Research and the Division of Pharmaceutical Chemistry and Technology. It is good to keep in mind, especially now when Finland just celebrated its 100th year of independence, that it is also a priviledge that in Finland basically everybody can study as much as they want. You can achieve the highest education, no matter what your background. "I started at the bottom, but I am headed to the top" as Saxon sings.

First of all I want to acknowledge my supervisors. I remember that at the after party of my cousin's PhD defence, one of the supervisors told my cousin that although he had three supervisors, he wouldn't have needed any. I had four supervisors and I have needed every single one of them. I would like to thank Professor Clare Strachan for all her help and guidance during the PhD project (well, actually it all started with the Master's thesis). You have been absolutely very supportive and always helpful and it has been a joy to work under your supervision. I am also happy that you have introduced me to the topic of vibrational spectroscopy and related imaging applications with all your knowledge. I have become more and more interested in that research area. In addition to your purely scientific help, I also thank you and your parents for proof-reading the Thesis (I know, as my English teacher once told me, my English is a bit strange sometimes). I want to thank Professor Hélder Santos for his supervision. I like your positive attitude, and you have always encouraged me. I remember when I started my Master's Thesis and Clare told me that there is this one Portuguese supervisor named Hélder Santos. For some reason, I got a picture of an old professor with curly grey hair in my mind. Well, I was a bit wrong, you are a young and talented scientist with a passion for science. I want to thank my supervisor Docent Leena Peltonen for her help and support. Your help has been also essential during my PhD project. Especially your knowledge of nanocrystal research has been very important, but I also want to thank you for your general support — you have also always been very positive. I also want to thank my fourth supervisor Doctor Antti Isömäki for his valuable help since the beginning of my Master's Thesis. It is very difficult to imagine how I could have done my work without your expertise on non-linear optics and CARS microscopy. You have also been very supportive and positive always. In conclusion, I think that my supervision was really good. All the supervisors had their own research specialities and I could benefit from this broad knowledge. I must also say that I am really happy that all of you also feel like friends to me!

A PhD project is something that you cannot do alone. It is a massive project that involves plenty of collaborations. I would like to thank everyone who has somehow helped me in my research. I would like to thank all the co-authors of my publications. Especially I would like to thank Doctor Nicolas Darville. We had a really good collaboration at the beginning of my PhD project that resulted in a good publication. I also want to thank Erkan Sözeri. Your work formed the basis for one of the publications. Doctor Sara J. Fraser-Miller, you have also been very important in my publications, I want to thank you. I also want to thank Professor Timo Laaksonen. I want to thank staff in the electron microscopy unit, especially Doctor Eija Jokitalo and Mervi Lindman. I want to thank my collaborators at Kiel University, Professor Regina Scherließ and Friederike Gütter. I also want to thank collaborators in Copenhagen and all the other co-authors.

I want to thank all my colleagues in the Division of Pharmaceutical Chemistry and Technology. I want to thank all the Professors including Jouni Hirvonen (Dean of the Faculty), Jouko Yliruusi and Anne Juppo and University Lecturers including Doctor Mia Siven and Doctor Henrik Ehlers. I want to thank Clare's group and all the FIP group, especially Dunja Novakovic (in addition to friendship, thank you for your great scientific co-operation that has resulted in publications), Jaana Koskela, Tiina Lipiäinen, Pilvi Myllymäki, Emmi Palomäki, Doctor Jenni Pessi, Doctor Jaana Hautala, Jernej Štukelj, Emma Hokkala, Doctor Mikael Agopov and Sanna Sistonen. I want to thank everybody in the NAMI group as well. I could mention everybody by name, because everyone is kind and helpful. Especially, I would like to thank the following persons for their scientific help at some stage of my research, but also for their friendship: Alexandra Correia, Doctor Mónica Ferreira, Doctor Dongfei Liu, Doctor Neha Shrestha, Doctor Francisca Araújo, Doctor Bárbara Herranz-Blanco, Eloy Ginestar, Doctor Mohammad-Ali Shahbazi, Flavia Fontana, Doctor Hongbo Zhang, Patrícia Figueiredo, Nazanin Ezazi, Feng Zhang, Doctor Chang-Fang Wang, Zehua Liu, Doctor Vimalkumar Balasubramanian (pity that I didn't have money to buy your house at the moment), Doctor Antti Rahikkala and Markus Selin. I want to also thank all the colleagues from the Chemistry side.

Now you see that doing a PhD is quite international. I have had the opportunity to travel a lot during my PhD project. According to my memory now, I have visited Lubljana, Düsseldorf (especially Emmi thanks for your great company), Copenhagen (with Doctor Mohammad Imran Niazi and Kristian Semjonov, thanks for your company), Paris (Châtenay-Malabry, maybe Doctor Mónica Ferreira, Doctor Elisa Lazaro Ibañez, Patrick Almeida, Doctor Sami Svanbäck and Doctor Jenni Pessi remembers my great pronunciation, thanks for your company), Kiel (sailing city, thanks Regina and Friederike for your hospitality), Ghent, Glasgow, Stockholm and Gothenburg. One definite benefit of doing a PhD is this internationality and the possibility to travel (let's hope this is still possible in the future despite Brexit and other stupid things going on) and meet people from different cultures. I think that the Portuguese culture has been one of the most prominent cultures in our laboratories. I have met many great Portuguese people like Tomás Ramos, João Martins, Alexandra Correia, Patricia Figueiredo, Ricardo Rosa, Sérgio Almeida, Mónica Ferreira and Patrick Almeida. Thanks for your energy! The Portuguese are really kind people, but it is not always easy to survive with you, since Finnish and Portuguese cultures are quite different (introvert versus extrovert). Especially, Patrick Almeida, you are a really good Portuguese friend of mine, thanks for your friendship.

Acknowledgements

I want to thank reviewers of this Thesis, Professor Andrea Heinz and Professor Andreas Zumbusch. Your comments helped me greatly to improve the content of this Thesis.

I want to thank Doctor Osmo Antikainen and Heikki Räikkönen (manager). You are not just all-round scientists, but great persons with whom I have had good conversations regarding a broad range of topics from boat engines to air currents to Deep Purple (and also work-related topics sometimes).

I want especially thank Doctor Tatu Rojalin, Sami Svanbäck and Tuomas Saarinen. You have become really good friends of mine. I think it has been really important to be able to talk with you about important topics such as football (or basketball as Tuomas prefers) and music. With Tatu I have spent numerous hours on a treadmill. Despite very important discussions related to Rock 'N' Roll we have also discussed a lot about spectroscopy, which has been an important aspect in understanding this Thesis topic. Thank you Tatu (it is a bit of a pity that you are in California now, despite Graham Bonnet singing in California Air (Better Here Than There): "It's slowly killing me, but it's better here than there, next to the cold North Sea". I started to play the guitar with Sami a few years ago and it has been a really nice way to relieve stress. I have noticed this also with the classical guitar, which I started to play when I was nine years old. If you want to play a song without major mistakes you have to focus carefully and then you don't have time to worry. Now, we have a band and playing in a band gives me a whole new level of joy. With Sami I have traveled to concerts abroad. By now, we have seen Rainbow in Loreley, Bietigheim-Bissingen, Glasgow and Birmingham while simultaneously driving across the countries. Those road trips have been awesome. I can tell the readers that these trips are real culture trips. I have plenty of good memories (in Rock) from those trips and can't wait for the next destination: Saint Petersburgh.

I thought that it is a quick task to write this, but I needed to go to sauna in between and change the music to Rainbow. Some of the readers (and people close to me) might have noticed that music is a really important part of my life. Hobbies are good for your mental health. For me, music and running are important (I have run two marathons despite my grandmother once advising me not to run a marathon, because it is too tough). With music I have had a chance to get involved in many great things. Deep Purple and Uriah Heep fan clubs in Finland, Perfect Strangers of Finland and Uriah Heep Suomi Finland are a kind of musical family to me with kind people. My band (Doctor Doctor) mates (Frank Takkinen, Tuukka Eerikkälä, Kari Martikainen, Martin Törnudd, Timo Tanner and Sami of course) are important too.

Last but not the least I want to greatly thank the most important people in my life, my parents, my mother Tarja and my father Jouko, and my sister Stina. I am sorry that I have been talking to you so much about my research lately — it must have been boring. Thank you for listening and supporting. Without you I couldn't have done anything, starting from your financial support in the beginning of my studies. My father has given me much great advice, for example he has told me: "Do not lose your temper". My father has also always been interested in science and therefore understands scientists. I have also discussed with my sister so many times about the problems and challenges of PhD studies that she probably will not start a PhD in the future, because I have scared her so thoroughly. I am sure though that you could do it if you would like, that's for sure. I really envy your energy. You can do anything. I believe that architecture is a good career choice even though you sometimes think that architecture studies are not a proper way to study (the students just wait for inspiration when other students do proper homework). It is also important that we get along well together. My mother has always taken really good care of me and it is difficult not to gain weight when I visit home :).

Long Live Rock 'N' Roll, On a dark winter evening, January 12, 2018, Jukka Saarinen

Jukka Saarinen

Acknowledgements

The following words (and music of course) give me energy:

”Kouriisi sylje ja kiristä vyösi,

kirkkain otsin onnes loit.

Tartu toimeen ja hoida työsi,

niin että sourassa seistä voit.”

- Arto Järvinen, **Teräsbetoni**

Acknowledgements

”Never surrender,
When you're up against the world,
Never surrender,
Stand up fight them all.”

-Peter “Biff” Byford”, Steve Dawson,
Peter Gill, Paul Quinn,
Graham Oliver, **Saxon**

”Legends have taught, battles fought,
this lion has no fear at heart.
Lion come forth, come from the north,
come from the north.”

-Joakim Brodén,
Pär Sundström, **Sabaton**

”By moonlight we ride, ten thousand side by side.
With swords drawn, held high, our whips and armour shine.
Hail to thee, our infantry, still brave beyond the grave.
All sworn the eternal vow, the time to strike is now.”

-Joseph G. Maio “Joey DeMaio”,
Ross “Ross the Boss” Friedman, **Manowar**

” If you suddenly see, what has happened to me,
you should spread the word around.
And tell everyone here, that it's perfectly clear,
they can sail above it all on what they've found.
It cries for you, it's the best that you can do, like a sound that's everywhere.
I can hear it screaming through the air, Long live rock and roll.”

-Ronnie James Dio, Ritchie Blackmore, **Rainbow**

” The world ain’t all sunshine and rainbows. It’s a very mean and nasty place, it will beat you to your knees and keep you there permanently if you let it. But it ain’t about how hard you hit, it’s about how hard you can get hit and keep moving forward. That’s how winning is done.”

-Rocky Balboa / Sylvester Stallone

To my family

Table of contents

Abstract ..... **i**

Acknowledgements ..... **ii**

Table of contents ..... **viii**

List of original publications ..... **x**

List of additional publications ..... **xi**

Abbreviations and symbols ..... **xii**

1 Introduction **1**

2 Review of the literature **3**

- 2.1 Solid-state forms 3
  - 2.1.1 Pharmaceutical importance of solid-state forms 3
  - 2.1.2 Techniques of detecting solid-state forms of API 4
- 2.2 Imaging of cells and drug delivery 5
- 2.3 Spectroscopy 10
  - 2.3.1 Raman spectroscopy and microscopy 12
  - 2.3.2 Spontaneous Raman imaging of biological samples and pharmaceuticals 16
- 2.4 Non-linear spectroscopy and imaging 19
  - 2.4.1 Theory and instrumentation of CARS microscopy 20
  - 2.4.2 Theory of SFG and SHG microscopy 23
  - 2.4.3 Hyperspectral imaging with multivariate data-analysis methods 23
  - 2.4.4 Non-linear optical imaging of biological samples and pharmaceuticals 25
- 2.5 Conclusion of the literature review 35

3 Aims of the study **36**

4 Experimental **37**

- 4.1 Materials 37
  - 4.1.1 Materials in cell experiments (**I-III**) 37
  - 4.1.2 Drug materials (**II-III**) 37
  - 4.1.3 Histological sections (**II**) 37
- 4.2 Methods 37
  - 4.2.1 Cell culturing (**I-III**) 37
  - 4.2.2 Preparation of nanocrystal suspensions (**II-III**) 38
  - 4.2.3 Preparation of indomethacin solid-state forms (**IV**) 38
  - 4.2.4 Preparation and storage of indomethacin tablets (**IV**) 38
  - 4.2.5 Scanning electron microscopy (SEM) (**III-IV**) 39
  - 4.2.6 Fourier-transform infrared spectroscopy (FTIR) (**IV**) 39
  - 4.2.7 Raman spectroscopy (**II-IV**) 39
  - 4.2.8 Cell viability tests for nanocrystal uptake studies (**II-III**) 40
  - 4.2.9 Sample preparation for cellular uptake studies (**II**) 40
  - 4.2.10 Multimodal imaging (**I-IV**) 41
    - 4.2.10.1 Microscope setup (**I-IV**) 41
    - 4.2.10.2 Non-linear spectroscopy (**I-IV**) 42
    - 4.2.10.3 Suitable insert materials for CARS imaging of live Caco-2 cell cultures (**I**) 43
    - 4.2.10.4 Evaluation of cell viability after CARS imaging (**I**) 43
    - 4.2.10.5 Imaging of PP nanocrystal cellular uptake (**II**) 44
    - 4.2.10.6 Imaging histological sections with PP nanocrystals (**II**) 45

4.2.10.7 Workflow for correlative CARS and EM studies (**III**) 45
4.2.10.8 Solid-state imaging with PCA based hyperspectral CARS and SFG (**IV**) 46
4.2.10.9 Multimodal non-linear imaging of surface crystallization (**IV**)............ 46

5 Results and discussion 47

5.1 CARS imaging of live Caco-2 cell cultures (I) 47
5.1.1 Screening of suitable imaging conditions and materials............................47
5.1.2 Label-free CARS imaging of live Caco-2 cell cultures on membrane inserts.. 49

5.2 Chemically-specific imaging of nanocrystal cellular uptake (II-III) 52
5.2.1 Narrowband CARS imaging of nanocrystal cellular uptake (**II**) 53
5.2.2 Live imaging of nanocrystal uptake (**II**).. 56
5.2.3 Multimodal imaging of histological tissue sections with nanocrystals......57
5.2.4 Correlative CARS and electron microscopy of nanocrystal cellular uptake (**III**).. 58

5.3 Multimodal non-linear imaging of solid-state forms on surfaces (IV).............. 64
5.3.1 Characterization of indomethacin solid-state forms................................. 65
5.3.2 Solid-state imaging with PCA based hyperspectral CARS and SFG...........67
5.3.3 Multimodal non-linear imaging of surface crystallization........................ 69

6 Conclusions 72

References 74

List of original publications

This thesis is based on the following publications, which are referred to in the text by their respective roman numerals (**I-IV**).

I **Saarinen J**., Sözeri, E., Fraser-Miller, S. J., Peltonen, L., Santos, H. A., Isomäki, A., Strachan, C. J., Insights Into Caco-2 Cell Culture Structure Using Coherent Anti-Stokes Raman Scattering (CARS) Microscopy. *International Journal of Pharmaceutics*, 523 (2017): 270–280

II Darville, N., **Saarinen J**., Isomäki, A., Khriachtchev, L., Cleeren, D., Sterkens, P., van Heerden, M., Annaert, P., Peltonen, L., Santos, H A., Strachan, C. J., Van den Mooter, G., Multimodal Non-linear Optical Imaging for the Investigation of Drug Nano-/microcrystal-cell Interactions. *European Journal of Pharmaceutics and Biopharmaceutics*, 96 (2015): 338-348

III **Saarinen, J**., Gütter, F., Lindman, M., Fraser-Miller, S. J., Scherließ, R., Isomäki, A., Jokitalo, E., Santos, H. A., Peltonen, L., Strachan, C. J., Synergistic Analysis of Cell-Nanoparticle Interactions Using Correlative Coherent Anti-Stokes Raman Scattering and Electron Microscopy. Submitted.

IV Novakovic‡, D., **Saarinen‡, J**., Rojalin, T., Antikainen, O., Fraser-Miller, S. J., Laaksonen, T., Peltonen, L., Santos, H. A., Isomäki, A., Strachan, C. J., Multimodal Non-linear Optical Imaging for Sensitive Detection of Multiple Pharmaceutical Solid-State Forms and Surface Transformations. *Analytical Chemistry*, 89 (2017): 11460-11467

‡ Novakovic, D. and Saarinen, J. contributed equally to this work.

Reprinted with the kind permission of Elsevier (**I and II**) and the American Chemical Society (**IV**).

List of additional publications

Additional publications, which are not included in the experimental part of this Thesis are listed below.

1. Mah, P. T., Novakovic, D., **Saarinen, J**., Landeghem, S. V., Peltonen, L., Laaksonen, T., Isomäki, A., Strachan, C. J., Elucidation of Compression-Induced Surface Crystallization in Amorphous Tablets Using Sum Frequency Generation (SFG) Microscopy. *Pharmaceutical Research*, 34 (2017): 957-970

2. Christophersen, P. C., Birch, D., **Saarinen, J**., Isomäki, A., Nielsen, H. M., Yang, M., Strachan, C. J., A., Mu, H., Investigation of Protein Distribution in Solid Lipid Particles and Its Impact on Protein Release Using Coherent Anti-Stokes Raman Scattering Microscopy. *Journal of Controlled Release*, 197 (2015): 111-120

3. Tuomela, A., **Saarinen, J**., Strachan, C. J., Hirvonen, J., Peltonen, L., Production, Applications and *In Vivo* Fate of Drug Nanocrystals. *Journal of Drug Delivery Science and Technology*, 34 (2016): 21-31

4. Fraser-Miller, S. F., **Saarinen, J**., Strachan C. J., Vibrational Spectroscopic Imaging. Chapter 17 in a book *Analytical Techniques in the Pharmaceutical Sciences,* Part V: Imaging Techniques, Editors: Müllertz, A., Perrie, Y., Rades, T., Springer (2016): 523-589

5. Tuomela, A., **Saarinen, J**., Hirvonen, J., Peltonen, L., Analytical tools for reliable *in vitro* and *in vivo* performance testing of drug nanocrystals, Analytical Tools for Nanocrystal Characterizstion, Imaging of Nanocrystals in Cells and Tissues. Chapter 11 in a book *Nanoscale Fabrication, Optimization, Scale-Up and Biological Aspects of Pharmaceutical Nanotechnology,* Editor: Grumezescu, A. M., Elsevier (2018): 441-469

Abbreviations and symbols

ADME	absorption, distribution, metabolism and excretion
ANPG	apoptic nuclear protein granule
API	active pharmaceutical ingredient
BF	bright field (microscopy)
Calcein AM	acetoxymethyl derivate of calcein
CARS	coherent anti-Stokes Raman scattering
C-CARS-EM	correlative coherent anti-Stokes Raman scattering and electron microscopy
CCD-detector	charge coupled device- detector
CLEM	correlative light-electron microscopy
CLS	classical least squares
dGCPQ	deuterated quaternary ammonium palmitoyl glycol chitosan
DMEM	Dulbecco's Modified Eagle's Medium
DPSS laser	diode-pumped solid-state laser
DSC	differential scanning calorimetry
EDTA	ethylenediaminetetraacetic acid disodium salt dihydrate
EdU	5-ethynyl-2′-deoxyuridine
EE	early endosome
EM	electron microscopy
epi-CARS	backwards detected CARS
ER	endoplasmic reticulum
ESM	ethosuximide
EthD-1	ethidium homodimer
FBS	fetal bovine serum
f-CARS	forward detected CARS
FITC	fluorescein isothiocyanate
FTIR	Fourier-transform infrared
FT-Raman	Fourier-transform Raman
FWHM	full-width-at-half-maximum
FWM microscopy	four-wave mixing microscopy
GFP	green fluorescent protein
GLI	glibenclamide
GLI-NC	glibenclamide nanocrystal
HBSS	Hank's balanced salt solution
HCA	hierarchical cluster analysis
He/NE laser	helium-neon laser
HEPES	2-[4-(2-hydroxyethyl)piperazin-1-yl]ethanesulfonic acid
HPMC	hydroxypropylmethyl cellulose
HyD- detector	GaAsP hybrid- detector
ILV	intraluminal vesicle
IR	infrared
LE	late endosome
MCC	microcrystalline celluloce
MCR	multiple curve resolution
MMP	metalloproteinase
MVB	multivesicular body

N	number of atoms in a molecule
NA = nsinθ	numerical aperture
Nd: YVO_4 laser	neodymium-doped yttrium orthovanadate laser
NEAA	non-essential amino acids
NIR	near-infrared
OPO	optical parametric oscillator
PAL	paliperidone
PALM	photoactivated localization microscopy
PBS	phosphate buffered saline
PC	polycarbonate
PC	principal component
PCA	principal component analysis
PEG	polyethylene glycol
PEST	penicillin G/streptomycin
PET	polyethylene terephthalate
PFA	paraformaldehyde
PLGA	poly(lactic-co-glycolic acid)
PLM	polarized light microscopy
PLP	phospholipide
PLSR	partial least squares regression
PMT-detector	photomultiplier tube- detector
PP	paliperidonepalmitate
PP-NC	paliperidonepalmitate nanocrystal
PTFE	polytetrafluoroethylene
PTX	paclitaxel
PXRD	powder X-ray diffraction
RGD	arginylglycylaspartic acid
RH	relative humidity
ROI	region of interest
SCXRD	single-crystal X-ray diffractometry
SEM	scanning electron microscopy
SERS	surface enhanced Raman scattering
SFG	sum-frequency generation
SG	Savitzky-Golay
SHG	second harmonic generation
SLN	solid lipid nanoparticle
SNV	standard normal variate
SONICC	second order non-linear imaging of chiral crystals
SRG	stimulated Raman gain
SRL	stimulated Raman loss
SRS	stimulated Raman scattering
STED	stimulated emission depletion
STORM	stochastic optical reconstruction microscopy
SVM	support vector machines
TAG	triglyceride
TEM	transmission electron microscopy
Tg	glass transition temperature
TGA	thermogravimetric analysis

Ti:sapphire laser	titanium-sapphire laser
TPEF	two-photon excited fluorescence
TW20	Tween® 20
UV	ultraviolet
VCA	vertex component analysis
WDN	wavelet denoising
λ	wavelength
$d_{x,y}$	lateral spatial resolution
d_z	axial spatial resolution
ν	frequency
c	speed of light
$\tilde{\nu}$	wavenumber
E	energy
$\boldsymbol{E}$	electric field
h	Planck's constant
$\boldsymbol{P}$	polarization
ε_0	vacuum permittivity
$\chi^{(1)}$, $\chi^{(2)}$ and $\chi^{(3)}$	first order, second order and third order electric susceptibilities
ω_S	Stokes beam frequency
ω_p	pump beam frequency
ω_{pr}	probe beam frequency
k	wavevector
$\chi_R^{(3)}$	resonant term of third order electric susceptibility
$\chi_{NR}^{(3)}$	non-resonant term of third order electric susceptibility
I_{aS}	CARS intensity (anti-Stokes)
A_{eff}	effective beam area
w	w = 0.687r; Rayleigh limit r = 0.61λ/NA, where λ is the excitation wavelength
λ_{SFG}	sum-frequency wavelength

1 Introduction

The drug development process is complex (Figure 1.) and can take as long as 15 years. The total costs for drug development from a molecule to marketed dosage form can be close to US $3 billion.[1,2]

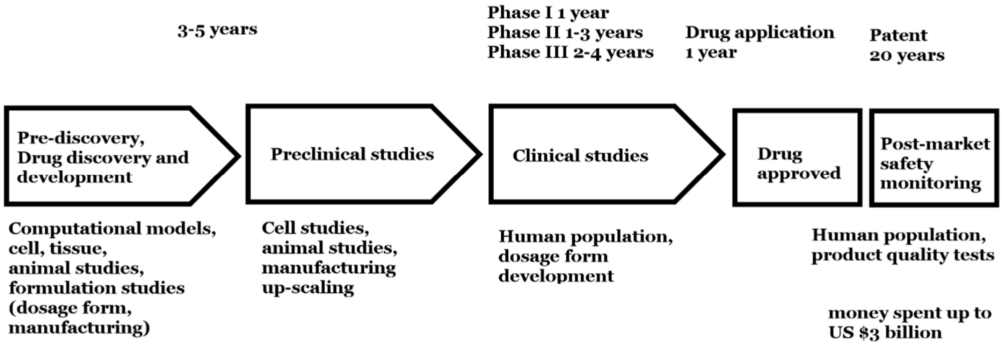

Figure 1. Schematic presentation of the time- and money consuming drug development process.

Drug development typically starts from pre-discovery, in which as much information as possible about a particular disease and its mechanisms are obtained. After this, a suitable target for the medication, such as a protein or gene in the human body, is identified during the drug discovery phase. Cell, tissue and animal models are used to study whether the target can be influenced by a molecule. This leads to the screening of suitable chemical entities from typically thousands of molecules that can bind to this desired target. From these experiments, the most promising lead molecules are found. At this point, a large number of early safety experiments are performed to gather information about the pharmacokinetic events of absorption, distribution, metabolism and excretion (ADME) and toxicity. The mechanism of action, drug-drug interactions and drug effectiveness against similar drugs are also studied. The lead molecules are further optimized in a “lead optimization” process in which hundreds of analogues of the initial lead are tested to find the most effective and safe molecule for the pre-clinical tests. Already at this stage of drug development, researchers start to think about the potential formulation, administration route and final dosage form of the medicine.

In pre-clinical studies, different types of *in vitro* and *in vivo* models are used to ensure the safety of the new drug molecule, also known as the active pharmaceutical ingredient (API), to be later tested on humans. At this point, cell models are used as well as animal models. Cell and animal models that mimic injury or disease similar to the human condition are used. The drug product itself and the production of the drug product on a larger scale (up-scaling) also receive more attention at this stage.

For the drug to be approved, extensive human (clinical) studies need to be performed to demonstrate the safety and effectiveness of the new drug. Clinical studies are divided into three phases. Phase I is when the new drug product is administered in human patients for the first time and therefore represents the first step in studying the safety and behavior of the new drug in the human body. Typically in this phase the population consists of between 20 and 100 healthy volunteers. After phase I, the population to which the drug is administered involves patients and is increased to approximately 100-500. Finally, the aim is to demonstrate the safety and efficacy of the new drug with a large enough population for statistical analysis, approximately 1000-5000 patients. Clinical trials are time-consuming big operations and most drug candidates fail in clinical trials. Even after the drug has been approved, regulatory authorities require constant monitoring of the approved drug as long as it stays on the market.

To develop new effective and efficient medicines with minimized costs, novel, adequate analysis techniques are required. Microscopy techniques can be very useful in any phase during drug development. Novel imaging techniques can be used to image cells in great detail, which is important when new drug formulations are tested in preclinical studies. Also imaging based techniques can be used to monitor drug manufacturing processes including mixing, tableting and coating. Novel, high resolution and chemically-specific imaging techniques can also be used to monitor drug's stability during storage.

There are currently several trends and challenges during the drug development process. One of the most challenging issues is that new drug molecules tend to be poorly water-soluble,[3] which means that they do not easily dissolve in the gastrointestinal tract for absorption into the bloodstream and transport to the action site. One possible approach to overcome this is to use the amorphous, or disordered, solid-state form of the API. The amorphous form exhibits faster dissolution compared to the crystalline solid-state form, where molecules are regularly arranged within the crystal lattice.[4] However, the amorphous form is thermodynamically unstable and it tends to crystallize over time. One other option to increase the dissolution rate of a poorly water-soluble drug is to reduce the particle size. For example, nanocrystals can be prepared.[5] Increased dissolution kinetics is one benefit of nanocrystals, but there is some evidence that intact nanocrystals could be also taken up by epithelial cells in the gut and therefore also improve the efficacy of poorly water-soluble drugs.[6,7] On the other hand, nanocrystals can be also used as injections for prolonged drug release.[8] In these cases, immune system macrophages can take up nanocrystals and influence pharmacokinetics.[8] However, these nanocrystal-cell interactions need to be investigated more.

A current trend in formulation science is to use different types of nanoparticles. There is a wide variety of different nanoparticles including nanocrystals,[5] solid lipid nanoparticles (SLN),[9] silica/silicon nanoparticles,[10] polymeric nanoparticles,[11] liposomes[12] and extracellular vesicles[13] just to name few. These nanoparticles can be used to improve the dissolution of poorly water-soluble drugs as in the case of nanocrystals or, for example, mesoporous silica particles can be loaded with amorphous drug.[14] However, probably the most advantageous feature of nanoparticles is that they can be tailored so that they target some specific part of the body, for example, tumor cells and tumor tissue.[15] This can be achieved especially with surface modifications of the nanoparticles with ligands capable of interactions with receptors in tumor tissue being added on the nanoparticle surfaces.[16]

Regardless of whether it is the solid state of the API, nanoparticle-cell interactions or drug influence on cell function, that needs to be monitored, suitable analysis methods are required. No single analysis method alone is capable of obtaining all the required information and every analysis method has its strengths and weaknesses. In this dissertation the potential of non-linear optical imaging, especially coherent anti-Stokes Raman scattering (CARS) has been evaluated in various pharmaceutical applications: imaging cells, nanocrystal cellular uptake and solid-state changes on the surface of solid dosage forms. Non-linear optical imaging has the general benefits of rapid data-acquisition time (video-rate imaging), label-free origin of the signal, inherent confocality (3D imaging capability) and non-destructive imaging. It is a chemically-specific method, since it is based on Raman scattering associated with molecular vibrations. These benefits, together with the natural benefit of imaging, make this coherent Raman-based technique very attractive in biomedical and pharmaceutical applications.

In the following literature review, the definition and description of the pharmaceutical importance of solid-state form of API, along with commonly used techniques for detecting solid state, are given, followed by a review of some of the most commonly used imaging techniques for cellular imaging. These descriptions will introduce the reader to some of the challenges that scientists face during the drug development process and highlight the importance of having suitable imaging methods. Since coherent Raman imaging is the main imaging technique used in this dissertation, spectroscopic imaging, especially Raman based imaging, is finally explained in some detail, with examples where these techniques have been used to image pharmaceuticals, cells and drug-cell interactions.

2 Review of the literature

2.1 Solid-state forms

2.1.1 Pharmaceutical importance of solid-state forms

Molecules can arrange themselves in different ways in crystal structures (Figure 2). This packing of molecules in three-dimensional repeating units (unit cells) in a crystal lattice defines the solid-state form. In contrast to well-defined crystal packing of molecules, disordered amorphous forms also exist. Amorphous materials can have only short-range order over a few molecular dimensions. Different crystal structures of the same molecule are called polymorphs.[17] Also co-crystals exist. Co-crystals are multicomponent crystals, in which the crystal lattice contains more than one type of molecule. Solvates, such as hydrates, where water molecules are incorporated in the crystal lattice, are examples of co-crystals. In the pharmaceutical industry, polymorphism has important implications. Different polymorphic forms can have significantly different physicochemical properties.[18] The crystal shape and size can vary between polymorphs, which can affect pharmaceutical industrial processes, such as milling, mixing and tableting.[17] Most importantly, dissolution kinetics can vary between different polymorphic forms.[4] In drug development, a huge challenge nowadays is that the majority of new drug molecules are poorly water-soluble.[3] To overcome this challenge, one solution is to use the amorphous form of the API, since its higher thermodynamic energy results in a higher dissolution rate. However, the challenge of using these amorphous structures lies in the fact that the amorphous state is not thermodynamically stable. This means that the API has a tendency to convert (crystallize) to a more thermodynamically stable form. Therefore, it is essential to have suitable analytical techniques to monitor the solid-state status of the API during formulation as well as storage.

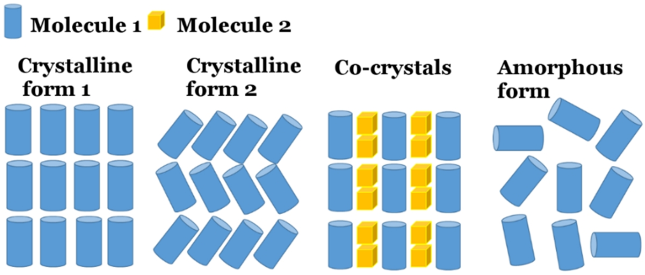

Figure 2. Solid-state forms of pharmaceuticals. The API molecules can be arranged in an ordered way in crystalline structures or a disordered way in the amorphous form.

Probably the best known case of polymorphic changes with clinical impact involves the drug ritonavir.[18] In 1992 it was only known to crystallize to form I. Two years after the ritonavir product was launched on to the market in 1996 as soft gelatin capsules, unexpected drug release behavior was observed, with some ritonavir capsules failing the drug release tests. It was observed that a less soluble, thermodynamically more stable, form (designated form II) was precipitating in the formulation. This led to the withdrawal of the product, since the lower dissolution of form II caused significant changes in the bioavailability of ritonavir. After reformulation, the product was once again approved and on the market.

2.1.2 Techniques of detecting solid-state forms of API

To ensure the desired solid-state structure of the API, its solid-state form has to be confirmed during different phases of drug development. The most common methods to obtain information about the solid-state structure are X-ray diffraction (single crystal and powder),[19] differential scanning calorimetry (DSC),[20] thermogravimetric analysis (TGA),[21] as well as microscopy methods such as polarized light microscopy (PLM)[22] and scanning electron microscopy (SEM).[23] Spectroscopy methods, especially infrared (IR) spectroscopy and Raman spectroscopy, are also widely used for this purpose.[24]

The most accurate method for obtaining information about crystal structures is single-crystal X-ray diffractometry (SCXRD).[17] This technique, however, requires crystals of suitable size and quality; typically the minimum dimension along each axis of the crystal should be at least 0.05 mm. The basis of X-ray based solid-state analysis is that X-rays interfere constructively and destructively during diffraction, resulting in a pattern unique to the respective crystal structure according to the Bragg equation:

$$n\lambda = 2dsin\theta, \tag{1}$$

where d is the distance between specific crystal planes in the crystal lattice, θ is the angle of diffraction of the X-rays, λ is the wavelength of the X-rays and n is an integer value. The angles of diffraction with constructive interference depend on the size and shape of the unit cells in the sample. By changing the angle of the incident rays, all possible diffraction directions of the lattice should be obtained. If a suitable single crystal is not available, powder X-ray diffraction (PXRD) can also be used, at least to identify the solid-state form present (rather than solve it).[17] As a matter of fact, this technique is widely used in pharmaceutical analysis. In this XRD technique, the powder is finely ground, homogenized and the average composition of the bulk material is determined by scanning the sample through a range of 2θ angles. All the possible diffraction directions should be obtained assuming sufficiently random orientation of the crystals in the powder. This technique results in X-ray powder diffractograms, which are unique to each solid-state structure and therefore can be used to identify the solid state of the API. Amorphous forms do not result distinctive peaks in diffractograms, but instead a broad amorphous halo is observed.

Thermal analysis for solid-state analysis relies on the absorption or release of heat, or alternatively on heat capacity changes, during physical changes in the material.[21] DSC is a common technique in pharmaceutical solid-state analysis. It is used to measure the energy (heat) changes of the sample when the temperature of the sample is altered.[20] By plotting the heat flow as a function of time, thermograms are obtained. Thermograms show endothermic and exothermic peaks, as well as heat capacity changes and this information can be used to get information about the solid-state form of the studied material. The most important events in thermograms are melting (endothermic) and the so called glass transition temperature (T_g).

X-ray diffraction techniques and thermal techniques can be used during drug development to precisely detect the solid state of an API at different phases, for example before and after some pharmaceutical process such as milling. However, thermal analysis methods are not non-destructive. Moreover, X-ray diffraction and thermal methods, in their standard setups, do not give information about the spatial distribution of the components in a sample. Imaging techniques are capable of that. PLM is a technique that is based on the physical phenomenon birefringence,[22] which depends upon anisotropy of the refractive index. In crystals, the molecules are arranged in an ordered structure, which leads to optical anisotropy (assuming the crystal is non-centrosymmetric). Due to this molecular arrangement, the absorption, refraction and scattering of light typically depends on the orientation of the crystals compared to polarization of the light. Under a microscope, when the crystals are rotated between crossed linear polarizing filters, the characteristic intensity changes in the light from each crystal are observed. Therefore, PLM provides information about crystallinity of the sample and is especially useful for distinguishing amorphous material from crystalline material. SEM has been also used to visualize different types of crystals with high resolution (low nanometer scale).[23] Information obtained from SEM images is purely morphological, i.e. based only on the shape and size of the particles.[4]

Solid-state specific imaging can be achieved by spectroscopy based techniques, which detect molecular vibrations.[24] The most widely used techniques in pharmaceutical solid-state analysis are those based on IR and Raman spectroscopy.[25] These can be adapted to imaging applications and are capable of visualizing the spatial distribution of different chemical and solid-state species in sample. The benefit of such imaging is that it can be used to visualize, for example, crystalline and amorphous regions and furthermore follow crystallization in a visual manner. Therefore more detailed information about crystallization behavior can be obtained and also images can be used to quantify the crystallization. These techniques can be applied to bulk material, but also non-invasively to dosage forms such as tablets. Spectroscopic imaging, especially non-linear spectroscopy methods such as CARS and SFG, can be especially useful when surfaces are analysed.

2.2 Imaging of cells and drug delivery

Microscopy has been an essential tool of scientists since the 17th century.[26] The first simple microscopes were introduced in 1595 in the Netherlands by spectacle-maker Hans Jensen and his son Zacharias. It was a simple compound microscope, a tube with two lenses. The first book about microscopy was written in 1665 by Robert Hooke. This included the first description of using a microscope with a stage and three lenses. In the mid-19th century, the first steps towards staining methods were taken as Joseph von Gerlach observed that the nuclei and nuclear granules exhibited good contrast after leaving a brain tissue section in a carmine solution overnight. Other staining methods have subsequently been developed and the use of fluorescence has been a very important step in microscopy. The first fluorescent microscope was developed in 1911, and since then confocal fluorescence microscopy, in particular (Figure 3),[27] has become one of the most widely used imaging techniques in biological analyses. Initially, only the auto-fluorescence of the specimen was used as a contrast agent, but soon afterwards the use of exogenous fluorescent labels became popular.

Nowadays, virtually any part of the cell can be visualized chemically-specifically using fluorescent labels. Fluorescence labels bind specifically to some particular part in the cell and, by illuminating with a suitable wavelength (energy), they emit light with a more or less specific wavelength (energy).[28] The binding specificity of fluorescence labels can be further enhanced with immunofluorescence. In this method, fluorescence labels are tagged to antibodies which can be used to target specific antigens in a cell.[29,30] Other important fluorescence markers are green fluorescent protein (GFP) and its modifications.[31,32] GFP, originally found in *Aequorea victoria* jellyfish, is a protein that fluoresces green light when illuminated with blue light. In 1992, the gene encoding GFP was cloned and since then it has been possible to connect this gene to the gene of the protein of interest, allowing the visualization of synthesis and trafficking of proteins in live organisms.[33]

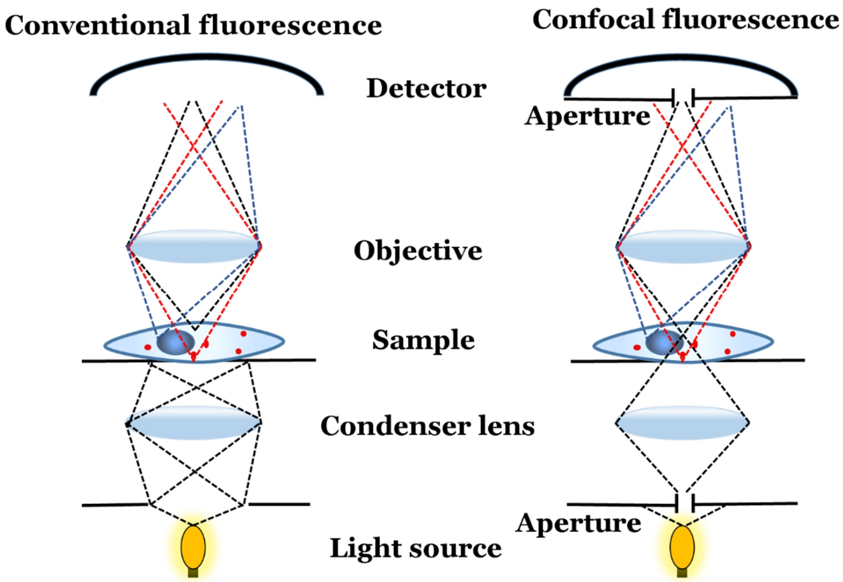

Figure 3. Principle of confocal fluorescence microscopy. The pinhole aperture blocks out-of-focus light resulting a sharper image with improved resolution. Confocal fluorescence microscopes can be also used to obtain 3D images, since confocal optical slices can be imaged with different axial positions. Adapted from Murray (2006)[34] with permission. Copyright (2006) Cold Spring Harbor Laboratory Press.

Fluorescence can be a useful phenomenon when drug interactions and cellular uptake of a drug or drug particles including nanoparticles are studied. For example, accumulation of naturally fluorescent drug molecules, such as doxorubicin[35,36] or curcumin[37] can be visualized in cells. Different types of nanoparticles can be also tailored so that fluorescent agents are included in the nanoparticle, which allows the detection of these particles in cells. For example, rhodamine B, a fluorescent agent, can be incorporated in the crystal lattice of nanocrystals, allowing the visualization of nanocrystals with fluorescence microscopy.[38] Another example of a fluorescent marker that can be incorporated in nanoparticles is fluorescein isothiocyanate (FITC).[39] The advantage of using fluorescence is that the signal intensity can be utilized for quantitative analysis. Confocal fluorescence microscopy can also be used to visualize the fluorescent signal inside the cells and quantitative analysis can be achieved by determining the fluorescence signal intensity at each pixel.[6] On the other hand, overall (non-spatially resolved) fluorescence can be also quantified by for example using a fluorescence plate reader[40] or flow cytometer.[41]

There is a constant desire and need to study details in cells on scales as small as possible. Such analysis is important to be able to gain precise information about subcellular processes. This is also important in drug development, since higher resolutions could reveal more information about the mechanisms of nanoparticle cell uptake. Nanoparticles can be taken up with different mechanisms and uptake mechanisms can play a significant role in intracellular drug release. Therefore in drug development it is important to know how nanoparticles are taken up into cells.[42] Uptake mechanisms can be studied with confocal fluorescence microscopy by using fluorescent markers to stain different organelles involved in uptake, for example intracellular vesicles such as lysosomes.[43] Information about nanoparticle uptake mechanisms is then obtained by visualizing the colocalization of nanoparticles and stained cell compartments. However, there is a physical limit to the resolution in any conventional optical microscopy technique, due to the wave-nature of the light causing diffraction when passing through an opening.[26] This means that with conventional fluorescence based microscopy, it is challenging or impossible to gain exact information about nanoparticle uptake mechanisms based on colocalization studies.

Diffraction of light causes blurred spots, when the light is focused.[44] The spot sizes determine the resolution. The resolution in the focal plane, $d_{x,y}$, (transverse full-width-at-half-maximum, FWHM, of the focal spot), can be defined as:[44,45]

$$d_{x,y} = \frac{\lambda}{2nsin\theta} = \frac{\lambda}{2NA}, \tag{2}$$

where λ is the wavelength of the light, n is the refractive index, θ is the maximum half-angle of the cone that exits the lens and $nsin\theta$ is the numerical aperture (NA). This means that by using a shorter wavelength, a higher resolution is obtained. However, UV light is more harmful for the cells and NIR light can penetrate deeper into most samples; these aspects favor the use of longer wavelengths. The resolution in the direction of optic axis, d_z, can be defined as:[44,45]

$$d_z = \frac{2\lambda}{nsin^2\theta}. \tag{3}$$

Recently, superresolution microscopy techniques have been used to break down the diffraction limited resolution barrier for which, the developers of these techniques, Eric Betzig, Stefan W. Hell and William E. Moerner, were awarded the Nobel Prize in Chemistry in 2014. Hell et al. used a technique called stimulated emission depletion (STED) microscopy to image below the diffraction limit.[46] In this technique, the illuminating area at focal point is reduced by quenching the fluorescence through stimulated emission at the rim of the excitation focal spot. This entirely stops fluorescence at the rim resulting in a fluorescing sample volume down to 0.67 attoliters, which can be scanned through the specimen in 3D. This lateral resolution is approximately 100 nm. Betzig et al. used another technique, photoactivated localization microscopy (PALM), to achieve nanometer resolution.[47] This approach takes advantage of photoswitchable fluorophores. Low-power illumination is first used to activate only a few of the fluorophores. These fluorophores are then imaged with high-power illumination and fluorescence of the fluorophores is immediately switched off with photobleaching. This process is then repeated thousands of times so that all the molecules have been switched on and off stochastically. Fluorescence in a single image originates from a single molecule, which means that the center of mass of the molecule can be calculated with a high precision and by combining every frame this leads to an image with a spatial resolution as good as 10 nm. PALM originally involved fluorescent proteins as photoswitchable markers, whereas another superresolution microscopy technique, stochastic optical reconstruction microscopy (STORM), used synthetic carbocyanide dyes. These two methods are essentially the same.[48,49]

Superresolution microscopy has been used to study drug nanoparticle-cell interactions. Zwaag et al. used STORM to image the uptake of different types of nanoparticles in HeLa cells and in DC2.4 cells.[50] They used carboxylic acid functionalized polystyrene beads labeled with Alexa-647-Cadaverine, amine functionalized polystyrene beads labeled with Cy5-NHS and carboxylated polystyrene beads functionalized with ovalbumin Alexa Fluor conjugate (OVA-AF647). Moreover cell components, including actin, the cell membrane, nuclear pore complex and macropynosomes, were stained for STORM imaging. They demonstrated the benefits of the sub-diffraction limit resolution of STORM by successfully imaging individual nanoparticles as small as 80 nm in the cells. In addition, they developed an image analysis method that could be used to quantify the nanoparticles inside the cells. Based on the detection of individual nanoparticles it was possible to obtain a size distribution histogram and average size of the internalized nanoparticles. This technique was furthermore applied for analysis of internalization of antigen (ovalbumin) modified nanoparticles in antigen-presenting dendritic cells (DC2.4). In this part of the study, the endocytic vesicles were also stained and colocalization of individual nanoparticles with individual vesicles was observed. The developed quantitative analysis method was also used in this part of the study with the particle size being used to conclude that ovalbumin was still in the nanoparticles in the cells. The authors finally compared STORM to electron microscopy as they imaged the DC2.4 cells with internalized nanoparticles. Electron microscopy images could be used to image the internalization of different particles in great detail. However, this study showed the challenge of electron microscopy; it is not chemically-specific. In comparison, STORM could be used to distinguish different nanoparticles based on both size and fluorescence color. This study nicely demonstrated the potential of superresolution microscopy to study nanoparticle-cell interactions. However, the imaging was performed with fixed cells. In future, superresolution microscopy techniques could be used to study nanoparticle cell interactions in live cells.

Despite the advances in superresolution microscopy, EM is still the only imaging technique that can truly visualize for example two biological membranes touching each other. It is also a method that allows visualization of the whole cell environment in great detail. This is beneficial, because it allows, for example, visualization of localization of drug nanoparticles on a subcellular level and therefore provides detailed information about drug uptake mechanisms. Also this information can be used to determine cell viability after drug treatment, since the morphology of the cell as a whole can be visualized.

All in all, it can be concluded that there is not a single imaging method capable of obtaining all the information required for the complete understanding of subtle cellular processes, including drug nanoparticle uptake. All the imaging techniques have their inherent benefits and weaknesses. Therefore, combining different complementary imaging techniques is becoming popular. In the most precise way, different imaging techniques would be combined to image exactly the same sample, for example the same cells. Combining light (typically fluorescence) microscopy, with chemical-specificity, and electron microscopy, with (sub)nanometer spatial resolution, can be especially beneficial. This approach, called correlative light electron microscopy (CLEM), has been used for cell imaging, with some cellular process first visualized in live cells with fluorescence microscopy, followed by cell fixing and electron microscopy imaging.[51] Most commonly, protein expression is visualized in live cells by fusing GFP to a specific protein. To visualize GFP in EM, the GFP can be labeled with an anti-GFP antibody that targets the GFP together with a secondary antibody carrying an EM contrast agent, such as colloidal gold.[52]

Vibrational spectroscopy imaging is currently gaining interest as an alternative microscopy technique, since the image contrast is obtained from molecular vibrations and therefore there is no need for external labels. Even though fluorescence imaging has benefits, there are drawbacks to using fluorescent labels. Added fluorescent markers do not naturally belong to nanoparticles and can affect the drug delivery behavior and potentially the function of the drug itself. Also, fluorescent probes can cause errors in image interpretation and dissociate from nanoparticles.[53] Moreover, photobleaching can inactivate the marker, making the drug again invisible for detection. Fluorescent markers induce phototoxicity. Amongst label-free, chemically-specific vibrational spectroscopy imaging techniques, especially coherent Raman imaging, has much potential for imaging cells and nanoparticle-cell interactions. Vibrational spectroscopy imaging, especially Raman-based imaging is explained and introduced more in detail in the next chapters, since coherent Raman imaging is the main technique used in this dissertation. In Table 1, some conventional and more advanced imaging techniques with their benefits and drawbacks are summarized.

Table 1. Summary of conventional fluorescence and EM techniques and more advanced imaging techniques with their benefits and drawbacks.

Imaging technique	**Resolution**	**Imaging specificity**	**Benefits**	**Drawbacks**
Electron microscopy	~0.1 nm	Contrast depends on differences in the electron density of the material and can be improved by staining e.g. with uranyl acetate and lead citrate	Subnanometer resolution	Often extensive sample preparation is required, typically not suitable for live cell imaging
Confocal fluorescence microscopy	Diffraction limited resolution, ~250 nm laterally with 500 nm excitation light and objective with NA of 1, axially ~500 nm[45]	Autofluorescence or external fluorophores can be used with high chemical-specificity	High chemical-specificity with added fluorescence labels, live-cell imaging, quantitative analysis	Need to use externally added fluorescent labels unless the specimen is autofluorescent
Superresolution microscopy	20 nm (STORM),[48] ~100 nm (STED)[46]	Fluorescent proteins or non-genetically encoded probes e.g. inorganic quantum dots, reversible photoactivable fluorophores and irreversible photoactivated fluorophores[54]	High resolution between that of EM and diffraction limited microscopes, live cell imaging	Need to use externally added fluorescent labels unless the specimen is autofluorescent, sophisticated instrumentation not yet widely available

Spontaneous Raman microscopy	Diffraction limited resolution, ideally if 532 nm laser is used with objective with NA of 1, 266 nm laterally and 532 axially[45]	Detected signal is based on molecular vibrations	Label-free chemical-specific imaging, linear signal to concentration dependence	Slow data acquisition, difficulties with fluorescent samples, sample damage with sensitive samples
CARS microscopy, SRS microscopy	Diffraction limited resolution, typically NIR lasers are used, therefore in theory a bit lower than spontaneous Raman, however signal can be generated from under even 100 nm spots[55]	Detected signal is based on molecular vibrations, high chemical-specificity in a label-free manner	Fast data acquisition, label-free chemical-specific imaging, linear signal to concentration dependence (SRS), inherent confocality, non-destructive	Non-linear signal to concentration dependence (CARS), non-resonant background (CARS) can be sometimes disturbing while imaging

2.3 Spectroscopy

Spectroscopy is the study of interactions of light (electromagnetic radiation) and matter as a function of wavelength. The measured light can be emitted, absorbed or scattered.[56] Spectroscopic techniques can be used to identify and quantify the properties of materials, since the electromagnetic radiation detected has distinctive wavelengths and energies based on the material studied. When light is dispersed and different wavelengths separated, a spectrum is generated. The distribution of different wavelengths (energies) in a single spectrum can vary and this allows materials to be characterized. An emission spectrum is generated when the material relaxes from an excited state by the emission of light. Fluorescence spectroscopy utilizes this phenomenon. An absorption spectrum is generated, when light is passed through a sample and certain wavelengths are absorbed. Infrared spectroscopy is an example of a technique that uses this phenomenon.

The principles of chemically-specific spectroscopic methods can be explained by energy diagrams (Figure 4). Each type of molecule has discrete energy levels due to the quantum mechanical behavior of the system.[57] The ground state is the lowest energy state of a molecule and its electrons. The higher energy states are excited energy states. Within these electronic states, several vibrational energy states occur and are caused by atoms vibrating in a periodic motion within a molecule. Several types of normal vibrational modes exist, including antisymmetric, symmetric, wagging, twisting, scissoring and rocking motions (Figure 5). In addition to these vibrational motions, the entire molecule can experience translational and rotational motion. However infrared and Raman spectroscopies deal with molecular vibrations.

Each molecule, with its bonds vibrating with specific energies, creates a unique fingerprint spectrum. Absorption spectroscopy methods measure energy transitions from the ground state to excited states, whereas fluorescence spectroscopy methods measure transitions from excited states towards the ground state.

Different degrees of freedom allow molecules to take up energy. If electronic excitations are neglected, these consist of rotational, translational and vibrational molecular motions.[56] Three of these are described by translational motion and three by rotational motion. Therefore, the possible number of vibrational modes can be calculated as:

$$3N - 6, \tag{4}$$

where N is the number of atoms in a molecule. This is true except in the case of a linear molecule, in which the number of possible vibrational modes is one fewer.

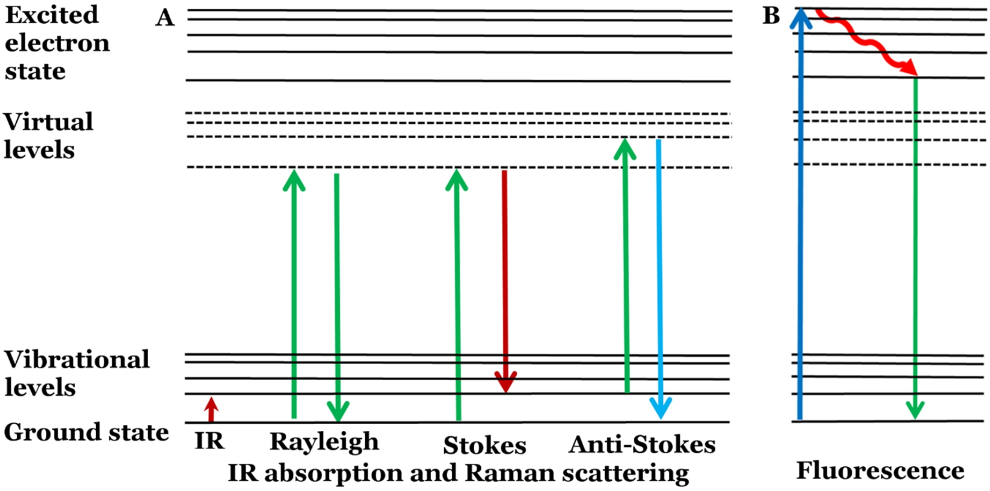

Figure 4. Energy level diagrams of IR absorption and Raman scattering (A) and fluorescence (B).

IR together with Raman spectroscopy are the most common methods of vibrational spectroscopy. These techniques are truly chemically-specific, since they directly measure atomic vibrations in a molecule. IR spectroscopy and Raman spectroscopy are complementary methods.[57] Both techniques can be used to probe the same molecular vibrations, assuming that these vibrations are IR and Raman active. The IR light can be absorbed only when there is a change in the dipole moment in a molecule during the vibration. Intense IR absorption occurs when the magnitude of the change of the dipole moment is high. Raman spectroscopy relies on inelastic scattering of light instead of absorption.[56] In Raman spectroscopy, the vibrational modes are probed through the molecule being excited to a virtual energy state from where it relaxes to the vibrational states specific to the particular molecule. Whereas IR spectroscopy requires a change in dipole moment, Raman spectroscopy detects the change in polarizability in a molecule, which can be seen as the distortion of the electron cloud around the nuclei. Therefore, typically non-polar, π-bonded and aromatic compounds are strong Raman scatterers. The origin of the signal results in some benefits of Raman over IR spectroscopy for pharmaceutical and biomedical applications. For example, Raman spectroscopy can be used to measure samples in an aqueous environment, whereas the high background in the IR spectrum could mask the signal from other components. In addition, APIs are often strong Raman scatterers compared to excipients, allowing efficient detection of APIs in drug formulations. Raman spectroscopy is covered in more detail in the next chapters since Raman spectroscopy and imaging, especially its non-linear variant, is used extensively in this Thesis for analyzing cells, drug delivery into cells and pharmaceutical solid-state forms.

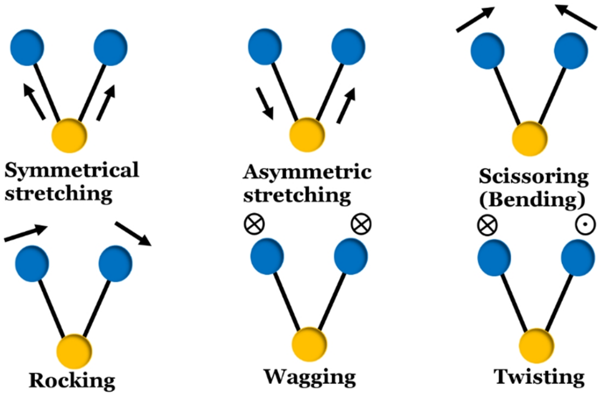

Figure 5. Molecular vibrations of the CH_2 group. These vibrations can be probed with vibrational spectroscopy methods. Circles with crosses indicate an atom moving into the page plane and circles with a dot indicate an atom moving out from the page plane.

2.3.1 *Raman spectroscopy and microscopy*

The discovery of Raman scattering dates back to the 1920s in India. Chandrasekhara Venkata Raman suggested that scattered light from the sea also contains an inelastic component. He submitted manuscripts related to this phenomenon in 1928 and was awarded the Nobel Prize in Physics in 1930 for this discovery.[58,59] In Raman spectroscopy, the sample is illuminated with a laser and light is scattered (Figure 6).[24,56,57] Most of the time, there is no change in energy between the incoming and scattered photons and therefore the scattered light does not give any information about the chemical composition of the sample. However, sometimes, quite rarely (one in every 10^6 – 10^8) photons undergo a change in energy during the scattering. This is called inelastic scattering. The change in energy between the incoming and the scattered photon can be positive or negative. If the scattered photon has lower energy compared to the incoming photon, the Raman scattering is called Stokes scattering. If the scattered photon has higher energy compared to the incoming photon, the scattering is called anti-Stokes scattering. Anti-Stokes scattering can occur in situations where the molecule is already in some excited vibrational energy level. This is always rarer compared to the situation where the molecule is in the ground state vibrational energy level. It is important to note that in conventional Raman spectroscopy, the sample does not receive enough energy to transition the molecules into an excited electronic state, but instead the molecules go to a virtual energy state from where they quickly relax to an excited vibrational state.

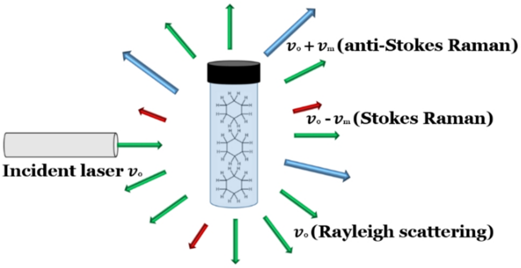

Figure 6. Raman scattering phenomenon. In Raman scattering, there is a shift in energy between the photons of the incident laser and scattered light. The shift in energy is quantized and depends on the chemical composition of the sample.

The energy of magnetic radiation is related to the wavelength by the following equations.[57] Firstly, the frequency ν, which describes how many waves of light travel in one second can be written as:

$$\nu = \frac{c}{\lambda}, \tag{5}$$

where c is the velocity of light. Instead of frequency, wavenumbers $\tilde{v}$ are often used as a unit in spectroscopy. The wavenumber is defined as:

$$\tilde{v} = \frac{v}{c}, \tag{6}$$

which describes the number of wave cycles per unit length and is typically expressed in the units of cm^{-1}. It is related to the energy by taking into account the quantum properties of light so that the energy of electromagnetic radiation is:

$$\mathrm{E} = h\,v = h\frac{c}{\lambda} = hc\tilde{v}, \tag{7}$$

where h is Planck's constant (6.63×10^{-34} Js). The energy difference between two quantized energy states can be described similarly:

$$\Delta E = hc\Delta\tilde{v}, \tag{8}$$

Hence, if the light is scattered from a molecule via Raman scattering, the transferred energy from the field to the molecule can be expressed this way. Thus, if the ground state energy level is E_1 and the excited vibrational state is E_2, the molecule absorbs or emits energy:

$$\Delta E = E_2 - E_1 = hc\Delta\tilde{v}. \tag{9}$$

In IR spectroscopy, this is the energy that a molecule absorbs at each vibrational transition. As mentioned, the origin of Raman spectra, involving scattering, differs from IR absorption spectra. In Raman scattering, the sample is irradiated with light (UV-Vis region) with a frequency v_0. The frequency of the scattered photon is $v_0 \pm v_m$, where v_m corresponds to a vibrational frequency of a molecule. In Raman spectroscopy the vibrational frequency v_m is observed as a shift from the frequency of the incident light, v_0, and the commonly used term for it is Raman shift.

As mentioned, in Raman spectroscopy the concept of polarizability is important and describes the movement of the electron cloud around the nuclei. According to the classical theory, atoms vibrating in a molecule can be seen as oscillating systems. When electromagnetic radiation interacts with these systems, the induced polarization can be described by the following power series expansion:[56,57,60]

$$\boldsymbol{P} = \varepsilon_0\,\chi^{(1)}\boldsymbol{E} + \varepsilon_0\,\chi^{(2)}\boldsymbol{E}^2 + \varepsilon_0\,\chi^{(3)}\boldsymbol{E}^3 + \ldots, \tag{10}$$

where ε_0 is the vacuum permittivity, $\chi^{(1)}, \chi^{(2)}$ and $\chi^{(3)}$ are the first, second and third order electric susceptibilities, respectively, and $\boldsymbol{E}$ is the electric field. χ is a dimensionless proportionality unit (tensor) that describes the degree of polarization of a dielectric material in response to an applied electric field. In spontaneous Raman scattering it is the first term $\varepsilon_0\,\chi^{(1)}\boldsymbol{E}$ that describes the polarization, and therefore spontaneous Raman is a linear method. When more energy is brought into the system, other terms become important. $\varepsilon_0\,\chi^{(2)}\boldsymbol{E}^2$ describes the second order non-linear interactions, such as second harmonic generation and $\varepsilon_0\,\chi^{(3)}\boldsymbol{E}^3$ the third order non-linear interactions, such as coherent-anti-Stokes Raman scattering.[60]

A typical Raman device is illustrated in Figure 7. The laser source in Raman spectroscopy typically operates in the UV-Vis region. Most often lasers with wavelengths of 532 nm or 785 nm are used. Also NIR wavelengths, such as 1064 nm are used especially in Fourier-transform Raman (FT-Raman) spectroscopy.[61] The sample is irradiated with the laser and the scattered photons are collected with lenses. Elastically scattered (Rayleigh) photons are filtered out, typically by a notch filter, and Raman scattered light is dispersed onto a detector in a spectrograph typically by a diffraction grating or prism. The detector is commonly a charge coupled device (CCD). The Raman spectrum is plotted so that the x-axis denotes the Raman shift (cm^{-1}) and the y-axis the intensity of scattering at each Raman shift. The collected spectrum is unique to each molecule, with that of cyclohexane serving as an example in Figure 8.

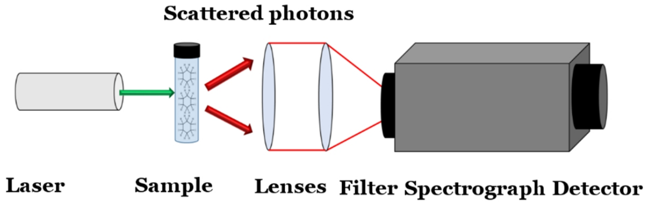

Figure 7. Illustration of a typical Raman spectrometer. Scattered photons are collected through lenses and directed to the spectrograph that separates the different wavelengths of the light.

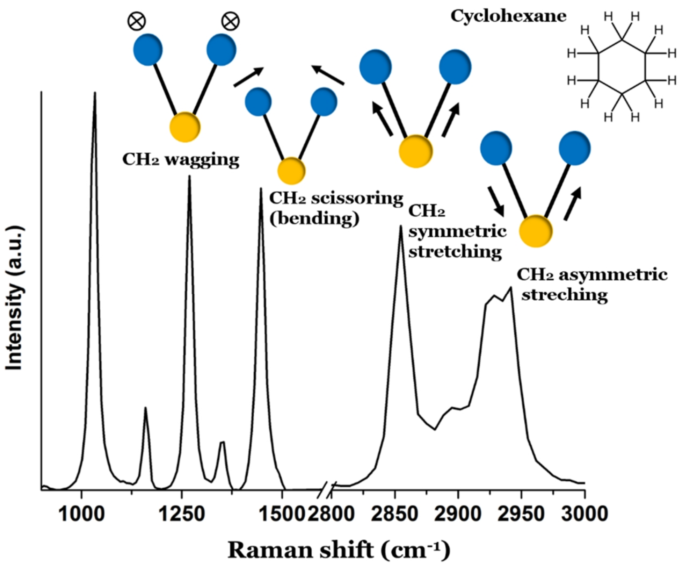

Figure 8. Raman spectrum of cyclohexane. Raman peaks originate from molecular vibrations illustrated above the peaks. The fingerprint (Raman shifts up to 1500 cm^{-1}) and CH-stretching (2800 -3100 cm^{-1}) regions were measured with two different measurements and thus their relative intensities are not to scale.

Raman spectroscopy can be also utilized with microsopy.[56,62] A Raman microscope can be built based on a standard optical microscope with the addition of an excitation laser, suitable optical filters, spectrometer or monochromator and detectors such as a CCD. The benefit of a Raman microscope over standard spectrometers is that it allows detection of the Raman spectra point-by-point since the laser beam can be focused through microscope objectives into small regions in the sample. Thus, high-resolution chemically-specific images can be constructed based on Raman scattered photons. Confocal Raman microscopes have further improved image quality, since pinhole apertures can be used to block out-of-focus light and suppress the background signal. This also allows for optical sectioning in the axial direction, making 3D imaging possible.

On a conceptual level, spontaneous Raman imaging can be divided into two categories: direct imaging and mapping.[24] The difference between the two techniques is that in mapping the full spectrum is acquired at each pixel, whereas in imaging a full image is directly obtained by scanning the specimen and detecting only one specific Raman shift. Typically, mapping can achieve a more data-rich image; however, it is also more time consuming.

Raman microscopes can generate a huge amount of data, since spectra can be collected pixel-by-pixel resulting a hypercube of data containing spatial (x-y-z) information and spectral information (λ). Therefore, image formation is not always straightforward and can require several data-processing methods. These data-processing methods are often needed even in cases where one only wants to interpret spectra as such, but become even more important with imaging. The first steps for the data processing include, for example, visual inspection of individual spectra and spectral preprocessing as described in the next paragraph. After that, the spectral data can be processed using univariate, bivariate and multivariate data-analysis methods to extract dominant patterns in the data and to visualize them as images.[24,63] In this Thesis principal component analysis (PCA) was used as a multivariate data-analysis method for CARS image formation in hyperspectral imaging approach. The description of PCA as a multivariate data-analysis method in spectral imaging is given in Section 2.4.3.

The need for data preprocessing can be minimized if the acquisition parameters have been optimized to achieve the highest possible signal-to-noise ratio. Nevertheless, Raman spectra often still contain some noise due to the electrical and thermal sources in detection.[64] Also, fluorescence backgrounds are common. The first step in preprocessing includes cosmic ray filtering. Visual inspection can also reveal outliers in the dataset that can be removed. A common Raman data preprocessing method to minimize noise is smoothing. Different smoothing algorithms exist. However, one has to be careful when smoothing is performed since there is always a risk of losing important data. The most commonly used smoothing algorithms to filter high-frequency noise are Savitzky-Golay (SG) smoothing, minimum noise fraction transform and wavelet denoising (WDN). Baseline correction is also a common procedure for Raman spectral processing, especially when fluorescence is present. For this purpose, typically polynomial baseline fitting is performed. In this procedure, the user can define some anchoring points that are used in polynomial fitting to get rid of the sloped baseline. Baseline correction can also be performed using first or second order differentiation with SG smoothing. The overall intensity can also vary between spectra due to changes in focus, sample surface or laser intensity changes, and scaling is a common procedure to remove such differences. Scaling (normalization) methods include minimum-maximum normalization and vector normalization, as well as standard normal variate (SNV) transformation. SNV transformation centers and scales each spectrum independently by its own standard deviation.

2.3.2 Spontaneous Raman imaging of biological samples and pharmaceuticals

The number of publications on spontaneous Raman imaging of biological samples, such as cells and especially drug delivery into cells is not high.[65–67] There are a few obvious challenges limiting such analysis. Spontaneous Raman imaging, especially in mapping setups, is slow and, therefore, especially live cell imaging is practically impossible. Secondly, drug concentrations inside the cells are typically very low, making detection challenging. Imaging in 3D is also difficult and time consuming, even with confocal Raman microscopes. On the other hand, spontaneous Raman microscopy has been extensively used to image a wide range of pharmaceuticals including for solid-state analysis.[62] In this chapter, an overview of studies of spontaneous Raman imaging of cells, drug delivery into cells and pharmaceuticals, including solid-state analysis, is given. Some examples are discussed in more detail, while different types of applications are summarized in Table 2. There are also excellent review articles of Raman imaging of pharmaceuticals and drug delivery.[62,68]

Despite the slow data-acquisition time with spontaneous Raman microscopy, it is possible to distinguish between different types of cell organelles in 3D in fixed cells. Recently, Prof. Steven's group from Imperial College London used a 3D confocal Raman microscope to measure Raman spectra pixel-by-pixel from many z-planes.[66] They acquired a volumetric hyperspectral dataset and applied univariate and multivariate data-analysis methods to the dataset. They visualized human induced pluripotent stem cells (hiPSCs) and their cardiac derivatives. First, they used univariate analysis to clearly visualize the cytoplasm (1008 cm^{-1}), nucleus (789 cm^{-1}), lipids (2857 cm^{-1}) and glycogen (938 cm^{-1}) in these cells in 3D. In addition, they imaged monocyte differentiation to macrophages (THP-1 cells). In this case, they applied the multivariate data-analysis method, vertex component analysis (VCA), to the volumetric hyperspectral dataset and could resolve different types of lipids – triglycerides (TAGs), phospholipids (PLPs) and cholesterol esters – in the cells and follow lipid content change during cell maturation. In the last step, they applied the same VCA method to human mesenchymal stem cells (hMSCs) that were cultured in two different types of 3D culturing matrices, one being biologically inert (polyethylene glycol, PEG) and the other one being biologically active with arginylglycylaspartic acid (RGD) and metalloproteinase (MMP) incorporated into PEG. They observed that the cells cultured in the inert culture matrix were round, while the cells cultured in the bioactive matrix became more elongated, showing cell interaction with the matrix material.

As mentioned, visualization of drug delivery into cells and detection of drug distribution in cells using label-free and chemically-specific Raman microscopy is a challenging, but interesting, task. In order to be able to detect low drug concentrations in cells, some approaches are available. It is evident that in such studies strongly Raman scattering drugs are beneficial. One example drug in this context is erlotinib.[69,70] Erlotinib is a drug containing a conjugated aryl alkyl moiety. The alkyne group with its triple C≡C bond gives a strong Raman signal in the biologically inactive region at 2125 cm^{-1}. The alkyl group can also be used as an added marker, as with fluorescent dyes. Even though usage of such markers perhaps removes one advantage from Raman as a label-free imaging technique, these Raman markers have benefits over fluorescent markers. First of all, alkyl Raman tags are smaller than fluorescent markers so that they do not alter normal cell functions, and the signal does not fade during prolonged imaging.[70–73] Other benefits are their biorthogonal nature (they do not react with endogenous biomolecules) and inexistence of alkyl moieties in cells. Alkyl Raman tags have been used to visualize different biomolecular events in cells. For example, amino acid and lipid analogues based on alkyne Raman tagging have been prepared. Yamakoshi et al. have shown, for example, that a thymidine analogue with an alkyne bond (EdU) can be incorporated into DNA during DNA replication and accumulate in the nucleus.[72,74] This allows for detection of proliferation of cells, since strong Raman signal can be observed from the nucleus. The signal is strong enough to be imaged with spontaneous Raman, but can be further strengthened with coherent Raman techniques.

A study showing the potential of Raman microscopy in detecting drug inside cells is that of El-Mashtoly et al (2014).[69] They used spontaneous confocal Raman microscopy to visualize erlotinib in human colorectal adenocarcinoma (SW480-228) cells.[69] They incubated the cells with erlotinib (100 µM) for 12 h and imaged the erlotinib distribution in fixed cells. They used the unsupervised learning algorithm, hierarchical cluster analysis (HCA), to analyze the spectral data and were able to visualize the cells and their different compartments including the nucleus with nucleoli and several distinctive regions in the cytoplasm. Most importantly, erlotinib was also found inside the cells. They could further show that erlotinib was metabolized inside the cells. Firstly, the spectrum measured inside the cell showed that a significant peak, characteristic for the drug carrier captisol, was missing, and furthermore the Raman spectrum of the drug inside the cell was significantly different compared to that of the free erlotinib. They compared Raman spectra measured inside the cell to the reference spectra of known metabolites of erlotinib and could show that the detected signal was actually desmethyl-erlotinib. This study shows the capabilities of label-free, chemically-specific Raman based imaging in detecting drug inside the cells. However, it is worth noting that the concentrations detected in human plasma with mass spectrometry are well below 10 µM after the oral administration of 150 mg of erlotinib per day and these concentrations are currently too low to be detected with spontaneous Raman analysis.

The vast majority of pharmaceutical applications of spontaneous Raman imaging are those where different types of dosage forms have been imaged. In these analyses the slow data-acquisition time is not as critical as in cell imaging. The API often contains chemical structures such as double bonds and aromatic rings that provide sufficient Raman scattering. Dosage forms or formulations in which the API distribution has been imaged with Raman microscopy include tablets,[75–78] powders,[79] granules,[80] inhalation formulations,[81–83] solid dispersions,[84] transdermal tapes[85] and printed medicines.[86]

In addition to visualization of API and excipients in a dosage form, Raman microscopy can be used to visualize different polymorphs and crystallinity since Raman spectra usually change between different solid-state forms of a material. This is due to different molecular packing and conformations that alter the molecular vibrations. One example is a study by Nakamoto et al., in which ethosuximide (ESM) in its crystalline and amorphous forms in model tablets containing lactose monohydrate, microcrystalline cellulose, hydroxyl-propyl-cellulose and magnesium stearate, was imaged.[78] Raman spectra of the materials revealed that crystalline ESM had peaks at ~1758 cm^{-1} and ~1705 cm^{-1} and amorphous ESM had a peak at ~1768 cm^{-1}. Since Raman peak positions between crystalline and amorphous ESM were located at different positions and excipients did not show Raman peaks in this region, it was possible to visualize both forms on tablet surfaces.

Haaser et al. used Raman imaging to study drug release during dissolution.[87] Extrudates made of theophylline anhydrate and lipid tripalmitine with and without PEG were imaged after dissolution. These studies were performed on the extrudates after dissolution testing for different times and removal from the dissolution medium for analysis. Pixel-by-pixel Raman mapping was performed covering the spectral region between 65 and 1520 cm^{-1}. Theophylline had a distinctive Raman peak at 554 cm^{-1}, tripalmitin had two peaks at 1100 cm^{-1} and 1130 cm^{-1} while PEG had two peaks at 844 cm^{-1} and 860 cm^{-1}. The normalized peak areas were used to calculate the drug distribution in the samples. According to UV-Vis spectroscopy, after 120 min 17% of theophylline was released from the extrudates made of theophylline and tripalmitine. According to the Higuchi theory, this would mean that theophylline would locate approximately at the boundary located 45 µm from the edge of the extrudate. It was actually possible to detect theophylline in the expected region, but it was observed that theophylline did not release uniformly. In the case of ternary mixtures, it was seen that PEG dissolved rapidly and after 30 min of dissolution PEG was not visible in Raman images. This example demonstrated that Raman microscopy can be used to observe drug dissolution with relatively good spatial resolution after removal of the sample from dissolution medium. In this example, the lateral spatial resolution was approximately 4 µm with a 50x objective.

Table 2. Some examples of studies where Raman microscopy has been used to image biological samples and pharmaceuticals.

Raman imaging of biological samples		
Sample type	Study	References
Human pluripotent stem cells and their cardiac derivatives, monocytes, monocyte-derived macrophages (THP-1 cells) and mesenchymal stem cells	Different types of endogenous cell compartments including cytoplasm, nucleus, glycogen and lipids were imaged in cells in 3D	[66]
EA.hy 926 cells, mice aortas	Biochemical composition of biological samples were visualized in 3D	[65]
SW480 cells, erlotinib	Erlotinib drug distribution and metabolism in colon cancer cells was monitored	[69]

RAW 264.7 macrophage cells, poly(diallydimethyl-ammonium chloride) coated nanorods	SERS signals could be obtained from the coated nanorods in the vesicles of live cells imaged by light microscopy	88
Algal culture	SERS imaging was used to follow intracellular biosynthesis of gold nanoparticles	89
MDCK cells, clofazimine	Antibiotic (clofazimine) cell accumulation was studied, confocal Raman microscopy was used to identify drug inclusions as amorphous drug	90
Escherichia coli cells, clavulanic acid, tazobactam	Raman microspectroscopy was used to study penetration of enzyme inhibitors into the bacterial cells and furthermore complexes between enzyme inhibitors and β-lactamase enzymes were detected	91
	Raman imaging of pharmaceuticals	
Dosage form	Study	References
Tablets	Excipients, API and polymorphs were visualized using Raman microscopy	75,76,78,92
Patch	Oestradiol crystals were observed in a drug patch	93
Vaginal rings	HIV microbicide was observed in the core and the sheath of the ring	94
Solid dispersions	Drugs were visualized in the solid dispersion and their distribution, physical state and presence of polymorphs and trace crystallinity was studied	84,95,96
Dried nasal spray	Beclomethasone dipropionate particels were identified and particle size distribution was obtained	97
Granules	The API and excipients were visualized on granule surfaces	80
Inkjet-printed pharmaceuticals	Raman mapping was used to visualize APIs on substrates of inkjet-printed pharmaceuticals	86,98
Dry powder inhalation	Raman imaging was used to identify API in powder with lactose carrier particles	81

2.4 Non-linear spectroscopy and imaging

Non-linear optical processes require several photons to interact in a material so that a new photon at a different energy is created.[60,99] Therefore, the overall output signal scales non-linearly with the intensity of the excitation light. The most common non-linear processes include coherent anti-Stokes Raman scattering (CARS),[100] sum-frequency generation (SFG) with its special case second harmonic generation (SHG),[101,102] and third harmonic generation (THG). Two-photon excited fluorescence (TPEF) also belongs to this category.[103–105] These non-linear phenomena are utilized extensively in biomedical imaging and are also generally referred to as multiphoton microscopy techniques.

In biomedical applications, multiphoton microscopy is frequently used due to its benefits compared to linear techniques. Typically, multiphoton microscopes use high-intensity NIR pulsed lasers that have better sample penetration compared to linear techniques. For example, whereas in linear fluorescence microscopy where a fluorophore is excited with a single photon having shorter wavelength compared to the detected photon, TPEF combines two photons with longer wavelength to excite the same fluorophore. The combined energy of these photons is equal to one photon in linear fluorescence. The longer wavelengths used in TPEF microscopy penetrate deeper into a biological specimen and are also less harmful, allowing live cell and tissue imaging. Other benefits of multiphoton microscopy are the inherent confocality, data acquisition speed and chemical-specificity.

Cell and tissue imaging includes a broad field of applications where multiphoton techniques are used.[100,106] These techniques are important in the pharmaceutical sciences,[107] since it is of great importance to be able to investigate how novel drug formulations, especially nanoparticles interact with biological matrices.[108] On the other hand, chemically-specific, highly sensitive detection methods using non-linear optical phenomena can be used in any phase during the drug development process. These techniques can potentially be used to identify raw materials, monitor processes such as mixing, and potential solid-state changes during processing such as tableting. Also these techniques have potential for quality control of final dosage forms. For example, dosage forms can be imaged during storage and solid-state changes can be monitored. Biomedical and pharmaceutical applications of non-linear imaging techniques are discussed in more detail in the next sections.

2.4.1 Theory and instrumentation of CARS microscopy

The main analytical method in this Thesis is CARS microscopy, and therefore its theory and instrumentation is discussed in some detail. As mentioned earlier, conventional spontaneous Raman scattering is a very weak process (one in every 10^6 – 10^8 photons).[56] CARS is a non-linear imaging method that relies on a stimulated Raman effect, which makes this technique much faster (at least 100 times faster) than spontaneous Raman.[109] Even though the CARS name has nothing to do with cars, the CARS process was first described in the Ford Motor Company in 1965.[110] Duncan et al. were the first ones to take advantage of the CARS phenomenon as a contrast agent in microscopy in 1982[111] and it has been further developed by Zumbusch et al.[112] The instrument development included the use of NIR excitation that avoids two-photon electronic resonance excitation and therefore significantly increases the sensitivity. Also long excitation wavelengths enable larger penetration depths. CARS is a third order non-linear process involving four photons in total, therefore it is also termed a four-wave mixing (FWM) process.[113] In the CARS process three photons coherently excite the sample so that they spatially and temporally overlap in a small focal point creating a fourth photon, which is then detected. The laser beams involved in CARS are called the Stokes (ω_S), pump (ω_p) and probe (ω_{pr}). The probe beam typically originates from the same source as the pump beam and it has the same wavelength. The wavelength of the Stokes beam or pump/probe beam is tunable and therefore specific vibrational frequencies can be probed so that the energy difference between the Stokes and pump beams corresponds to some molecular vibration. This vibration is then probed with a probe photon. The resulted energy diagram of the CARS process is shown in Figure 9. The emitted photons in CARS are blue-shifted anti-Stokes photons, $\omega_{aS} = \omega_p - \omega_S + \omega_{pr}$.[60] The CARS signal can be detected in the forward direction (f-CARS) or backward direction (epi-CARS).

In order for the four-wave mixing to occur efficiently, phase-matching conditions are required.[60,100,114] Under phase-matching conditions, the photons are combined in phase to generate the CARS signal that is detected. Current CARS microscopes use high numerical aperture (NA) objectives to tightly focus laser beams, so that the required k-vectors are always present and the interaction length is too short for dephasing. [112]

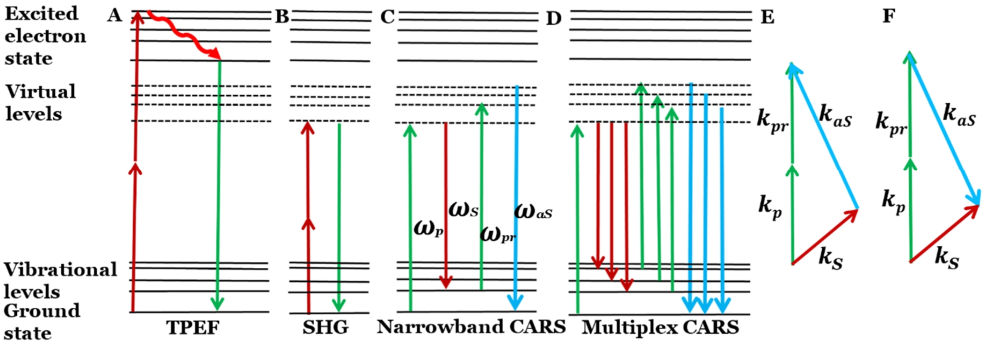

Figure 9. Energy diagrams of (A) TPEF, (B) SHG, (C) narrowband CARS, (D) multiplex CARS and the phase matching conditions for forward-generated CARS (E) and epi-generated CARS (F). k is the wavevector, and is expressed as $k = 2\pi / \lambda$. k_S, k_p and k_{pr} are the wavevectors for the Stokes, pump and probe beams, respectively. In narrowband CARS, a single vibrational transition is addressed at a time, whereas in multiplex CARS, a broad range of vibrational transitions are addressed simultaneously.

In the CARS process, the third order non-linear electric susceptibility of the sample, $\chi^{(3)}$, can be expressed as:

$$\chi^{(3)} = \chi_R^{(3)} + \chi_{NR}^{(3)}, \tag{11}$$

where $\chi_R^{(3)}$ is the resonant term and $\chi_{NR}^{(3)}$ is the non-resonant term. It is the resonant term that contains information about chemical composition and quantity of the sample through vibrational resonances.[115] It is worthwhile to mention that there is always a non-resonant part in CARS that originates from the electronic properties of the material.[109] The overall intensity in CARS depends on both the resonant and the non-resonant components as:[115]

$$I_{aS} \propto |\chi^{(3)}|^2 = \left|\chi_R^{(3)} + \chi_{NR}^{(3)}\right|^2 = |\chi_R^{(3)}|^2 + 2\chi_{NR}^{(3)} RE\left[\chi_R^{(3)}\right] + \left|\chi_{NR}^{(3)}\right|^2 \tag{12}$$

CARS imaging is a microscopy technique that has become the subject of much interest, since it has several benefits. First of all, the image acquisition time compared to spontaneous Raman microscopy is at least a hundred times faster.[116] This allows chemically-specific, label-free and video-rate imaging.[117] Non-linear techniques are also inherently confocal, since the signal is generated only in the small focal point, which allows 3D sectioning. Furthermore, CARS is a relatively non-destructive imaging method that allows live cell imaging.[118,119] The longer wavelength laser sources have the benefit that the multiphoton sample damage significantly reduces when longer NIR lasers are used.[120–122] NIR wavelengths also have better penetration properties, which allow analyses of turbid samples and deep tissue imaging.[100]

The general requirements for CARS microscopes are high NA objectives and short pulsed lasers, typically with picosecond or femtosecond pulse duration.[100,113] Also suitable detectors, such as photo-multiplier tubes (PMTs) or CCDs are required. CARS techniques can be divided roughly into two categories: narrowband (single-frequency) CARS, and multiplex (broadband) CARS. The basic difference between these techniques is that narrowband CARS probes one vibrational mode at a time, whereas multiplex CARS probes several vibrational modes simultaneously.[100,115,121,123–125]

Narrowband CARS setups usually consist of two picosecond laser sources.[100] One example of a narrowband CARS setup is the one used in the experimental part of this Thesis. Its laser setup consists of a Nd:YVO_4 laser, which pumps an optical parametric oscillator (OPO), producing two output beams (idler and signal). The wavelength of the fundamental Nd:YVO_4 laser beam is typically 1064 nm and this is used as a Stokes beam in the CARS process. The Stokes beam is combined with a tunable signal beam (pump) produced by the OPO. To achieve simultaneous detection over a wide range of Raman shifts in multiplex CARS, a spectrally broader femtosecond Stokes pulsed laser can be utilized. Cheng et al. and Müller et al. achieved multiplex CARS imaging with two Ti:Sapphire lasers with one laser beam having a picosecond pulse duration and the other (Stokes) having femtosecond pulse duration.[121,123,126] Later, the bandwidth of the Stokes beam was further increased using tapered and photonic crystal fibers to achieve broadband CARS microscopy capable of probing CARS shifts between 500 and 3100 cm^{-1} in a single measurement without additional laser tuning.[125,127–129]

Broadband CARS is a data-rich method, since it detects a full spectrum at each pixel (hyperspectral imaging). This can be more time consuming, but setups in this field are under continuous development and their imaging speed is becoming faster and faster.[130,131] Spectral information can be useful if more accurate analysis of the chemical composition of the sample is needed. The collection of whole spectra also facilitates quantitative analysis. As mentioned in equation 12 the CARS intensity scales quadratically to the third order susceptibility of the material and the CARS signal consists of resonant and non-resonant terms. The resonant term $\chi_R^{(3)}$ contains the chemically-specific information. More precisely, it is the imaginary part Im $[\chi_R^{(3)}]$ that can be directly compared to spontaneous Raman spectra and is linearly proportional to concentration and therefore used in quantitative analysis.[115] However, it is not straightforward to extract this component. In order to be able to retrieve the imaginary part of the CARS signal one has to access the phase θ of the CARS field, since Im $[\chi_R^{(3)}]$ depends on the field according to the following equation:

$$\mathrm{Im}[\chi_R^{(3)}] = \left|\chi^{(3)}\right| sin\theta \propto \sqrt{I_{aS}}\, sin\theta. \tag{13}$$

Conversely, the main benefits of narrowband CARS over broadband CARS microscopy are the fast data-acquisition and improved signal-to-noise ratio.[100] In narrowband CARS microscopy, the narrow bandwidth of picosecond pulsed lasers are well matched to single vibrational resonances, at the same time allowing effective and fast probing of these vibrations. This is especially beneficial when fast imaging is required, for example in the case of live cell or tissue imaging. With narrowband CARS microscopes, it is also possible to acquire a CARS spectrum with more time. In this case the wavelength of a pump beam is systematically changed and images are acquired at each wavenumber.[132–134]

In addition to CARS microscopy, another coherent Raman technique is stimulated Raman scattering (SRS) microscopy.[99,135–140] The SRS phenomenon was observed just after the invention of the ruby laser but is still a relatively new imaging technique first used in 2007.[141] In SRS, as in CARS, signals are generated by the co-alignment of the pump and Stokes beams so that the energy difference matches a molecular vibration. In this way stimulated excitation of the molecular vibration occurs. In the process, intensity loss in the pump beam (stimulated Raman loss, SRL) and intensity gain in the Stokes beam (stimulated Raman gain, SRG) is induced.[70] Whereas in CARS the anti-Stokes signal generated by the four-wave mixing process is detected, in SRS the image contrast is based on the modulation of the pump beam. Typically, the Stokes beam is actively modulated and the induced modulation in the pump beam is measured using radio-frequency lock-in detection. The benefits of SRS over CARS microscopy are non-resonant background free imaging, linear signal dependence to concentration, and spectral shapes that closely resemble those obtained from spontaneous Raman spectroscopy.[99,142]

It is also worthwhile to mention that CARS is a special case of non-linear four-wave mixing (FWM) processes. FWM microscopy is not only limited to probing molecular vibrations, but is also sensitive to electronic properties of the material. Electronic excitations can be probed by tuning the incoming or emitted frequencies into an electronic resonance of the material.[119,143–145] For example, silicon and gold have been imaged using FWM microscopy, and the electronic four-wave mixing is especially important in the case of nanomaterials.[145]

2.4.2 Theory of SFG and SHG microscopy

Another interesting non-linear imaging method in addition to CARS microscopy is sum-frequency microscopy and its special case, second harmonic generation microscopy.[101,102,107,146–148] These phenomena are not based on vibrational resonances as with CARS, but can also provide label-free imaging. The signal in SFG can be generated from samples in which inversion symmetry is broken, such as crystals with a non-centrosymmetric structure or boundaries between materials or chiral structures.[107] SFG is a second order process and thus requires two input photons that interact with the sample and each other, resulting in frequency-summing of the two photons. SHG is a special case of SFG where two of the input photons have the same energy and the generated second harmonic photon has exactly double the energy (half the wavelength) compared to the photons in the excitation beam (Figure 9). Therefore, the SHG signal can be generated by using a single laser source. A pharmaceutically important application of SFG and SHG is the detection of crystallinity.[146,147,149,150] Non-centrosymmetric crystals produce SFG and SHG signals and this can be utilized, for example, in the studies of crystallization (stability studies or studies to get more information about crystallization processes). In biomedical applications, SHG is often used to visualize collagen fibers or microtubules.[151,152] A similar phenomenon to SFG and SHG also exists as a third order process. Third harmonic generation signal production does not require a break in symmetry and, thus, most materials can generate some THG signal. However THG is not used in this Thesis and therefore is not further discussed in this context.

Generally, temporally short and spatially broad femtosecond pulsed laser sources are preferred in SHG microscopy to obtain strong signals.[147–149] However, in multimodal imaging it is possible to use different non-linear phenomena (CARS, SFG/SHG and TPEF) in a single instrument also with picosecond laser sources. In biomedical multimodal imaging applications, often CARS is used to image lipids using CH_2 stretching, while SHG is used to visualize collagen.[153,154]

2.4.3 Hyperspectral imaging with multivariate data-analysis methods

In general, hyperspectral imaging means that, during image acquisition, a spectrum at each pixel is measured. To form a meaningful image with spectral information, univariate, bivariate or multivariate data-analysis methods can be applied to the spectral data.[24,63] Univariate methods are the simplest, as they use just a single variable such as peak intensity at a single wavelength or the integral of a band. Bivariate methods use two variables for image formation, such as the ratios of peak intensities at two different wavelengths. Multivariate data analysis methods generally use whole spectral data in image formation and these techniques can be therefore especially useful in the case of spectral overlapping signals in a heterogeneous sample.

Common multivariate data-analysis methods include principal component analysis (PCA), classical least squares (CLS), partial least squares regression (PLSR) and multiple curve resolution (MCR). These multivariate methods can be supervised or unsupervised. Unsupervised methods do not require any prior knowledge of the sample, whereas supervised methods use some reference spectra in the processing. The multivariate data-analysis methods also include classification methods, where spectra can be categorized based on spectral similarities. PCA is an unsupervised classification technique, along with hierarchical cluster analysis (HCA), k-means clustering and fuzzy C-means clustering being the most popular ones. Supervised techniques that can be used to classify spectra include, for example, linear discriminant classifiers (LDCs), artificial neural networks and support vector machines (SVMs). In this Thesis PCA is used as the multivariate data-analysis method for classifying spectra and image formation based on CARS spectral data and, therefore, this method is described more in detail below. More informative descriptions of other methods can be found elsewhere.[24,63,155,156]

PCA is a widely used multivariate data-analysis method in pharmaceutical applications. PCA can be used to distinguish repeating variations in a spectral dataset.[24,63,157,158] Spectral datasets in imaging (x, y, λ), are multidimensional hyperspectral datasets. PCA is a tool that can be used to re-express these datasets with a lower number of variables. It is based on the detection of variance in the data and retaining the most significant variance in the data.

Let us have a look at a hypothetical simplified spectrum with only two peaks (Figure 10A). The same principle works with any spectrum with n peaks. Spectra with n peaks can be plotted based on the peak intensities in n-dimensional space as shown in Figure 10B. After all the spectra are plotted this way (Figure 10C), a PCA algorithm calculates the principal component vectors (eigenvectors) and forms a new coordinate system (Figure 10D). The original data points (spectra) can be projected onto the axes of the newly formed coordinate system (Figures 10E and F) and therefore each data point can be expressed as numbers, PC scores, which describe the position of the projected data points from the origin of the new coordinate system. As the number of PCs increases, the higher order PCs describe less and less of the variation in the data. Therefore, only lower order PCs that describe most or a substantial proportion of the data can be used to explain the meaningful variation. Often the three first PCs are enough to explain the useful variation in the data.

PCA can be used to graphically illustrate differences in spectra as shown in Figure 10E. This kind of illustration is called a PC score plot. The data points (spectra) with similarities (e.g. the spectra that show the same peaks or more generally spectral shape) are plotted close to each other since they have similar PC score values. PCA can be also used to form images based on the spectra at each pixel. After recording the spectra, PCA is performed and the resulting PC score values at each pixel can be used to form false-color images. One approach to performing this is to use, for example, the first three PCs (they often explain most of the variation in the data), each with a defined color, and use PC score values at each pixel as the basis for the resulting combination colors. For example PC1 can correspond to red color, PC2 to green color and PC3 to blue color. Based on the score values, intensities of these colors can vary and pixels with similar spectra are colored similarly.

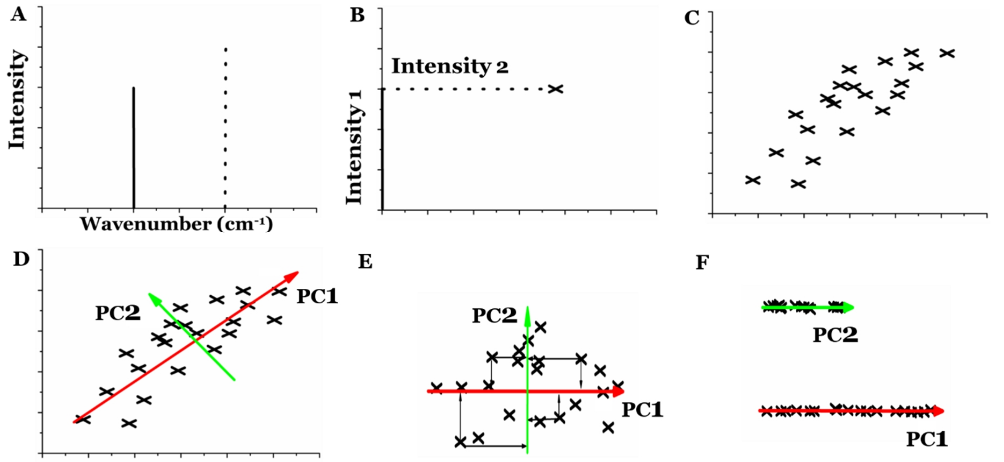

Figure 10. Schematic presentation illustrating the principle of PCA in spectral analysis. Spectra (A) with n peaks can be plotted with n-dimensional space (B). After all the spectra (C) are plotted, principal component vectors (eigenvectors) can be plotted so that PC1 is aligned to the direction of the most variance in the data (D). Principal component scores are the values of the projected data points in a new coordinate system (E and F).

2.4.4 Non-linear optical imaging of biological samples and pharmaceuticals

Due to the benefits of non-linear imaging, including fast data-acquisition allowing video-rate imaging, inherent confocality allowing 3D imaging, the label-free and chemically-specific nature of the signal, improved sample penetration and relative non-destructivity of the NIR lasers, multimodal non-linear optical imaging has become increasingly popular in the field of biomedical applications.[99,118,159,160] Cells and tissues are full of lipid structures with plenty of CH bonds. Most often CARS microscopy has been used to image biological specimens by using a CARS shift at around 2850 cm^{-1} that originates from the CH_2 stretching of lipids.[118,122,161–165] Especially lipid droplets have been visualized this way. Excellent review articles on biomedical applications of coherent Raman and non-linear optical imaging have been written.[99,100,160] In this section, a basic overview of the potential of these techniques in biological imaging and pharmaceutical applications is given. The diversity of non-linear optical imaging in this context is also summarized in Table 3.

Multimodal non-linear imaging of lipid droplets in live cells with a combination of CARS microscopy and TPEF dates back to the early 21st century when Prof. Sunney Xie and his group performed lipid droplet imaging studies at Harvard University. They imaged lipid droplets in live 3T3-L1 fibroblast cells with a CARS shift of 2845 cm^{-1} and followed how lipid droplet content changed during cell differentiation.[122,166] They observed that first the number of lipid droplets decreased during the differentiation process and then drastically increased with the size of lipid droplets growing. In later studies they monitored lipid droplet transport in live steroidogenic mouse adrenal cortical (Y-1) cells with CARS microscopy.[161] They concluded that with a pulse energy under 2 nJ and the average power under 9 mW for the pump laser (710 nm) they could follow the lipid droplet transport non-invasively. They also combined the analysis with TPEF imaging of mitochondria to study the interactions between lipid droplets and mitochondria in adrenal gland cells.

Lipid droplets have also been imaged in living organisms. For example, Hellerer et al. used CARS microscopy to image lipid droplets in living *Caenorhabditis elegans* worms.[167] They used worms with different genetic variations in metabolic pathways to demonstrate the potential of label-free CARS microscopy in studies of obesity-related diseases. They observed clear differences between genetically modified species. Genetically modified species favoring lipid synthesis and down-regulation of the glycolysis showed a significantly higher lipid volume fraction compared to control worms. Moreover, they compared label-free CARS microscopy to fluorescence imaging of stained lipid droplets and showed that two-photon fluorescence underestimates the number of lipid droplets compared to label-free CARS microscopy.

Since CARS microscopy is especially suitable for lipid detection, one disease model that has been studied with CARS microscopy is atherosclerosis. Lim et al. used narrowband CARS microscopy to image lipid structures in plaque lesions of mouse aortas.[134] In their study, two mouse models were used: low density lipoprotein receptor-deficient (LDLR$^{-/-}$) and ApoE lipoprotein-deficient (ApoE$^{-/-}$). They observed that cholesterol crystals were found in the aortas of mice. The crystals were more abundant in the plaques of ApoE$^{-/-}$ mice. This study showed the potential of CARS microscopy to study the progression of atherosclerosis involving cholesterol crystals.

Another fascinating application of multimodal CARS/TPEF imaging of cells is a study by Prasad et al. They imaged lipids with CARS microscopy at 2840 cm^{-1} and proteins at 2930 cm^{-1} and fluorescently stained (acridine orange stain) DNA and RNA compartments with TPEF in HeLa cells undergoing apoptosis.[168] A particular focus was on CARS images of proteins and it was observed that in the control cells most of the protein content was accumulated in the nucleolus. The protein distribution in the nuclear environment drastically changed during apoptosis: 30 min after beginning apoptosis, protein distribution was disturbed and apoptic nuclear protein granules (ANPGs) were formed. Moreover, it was shown that after 2 h of apoptosis nucleolar proteins formed a complex network, and after 24 h proteins left the nucleolus and chromatin bodies segregated from the proteins.

Current development of broadband CARS setups have allowed the probing of other cell structures in addition to lipids and proteins (with CARS shifts between 2840 and 2930 cm^{-1}). The drawback of using broadband CARS microscopes can be slow data acquisition. However, recent developments in broadband CARS microscopes have significantly improved this, allowing CARS imaging in the fingerprint region.[169] Cicerone et al. have used broadband CARS microscopy to image human mesenchymal stem cells (hMSCs) cultured in three different culturing media for 2 weeks.[170] Since a full spectrum was measured at each pixel from 500 cm^{-1} to 3400 cm^{-1} the full spectral information could be used to form pseudo-colored images of cells showing that lipids, cytosol, nucleus and minerals could be distinguished. Furthermore, two data-processing methods were used on the spectral data obtained from differently cultured stem cells to find out from which lineage the cells were growing. In the first method, they used specific CARS peaks or regions of peaks as biomarkers and, based on the signal intensities of these biomarkers at each pixel with suitable threshold limits, they could classify the cells based on the differentiation. PCA classification, using all the spectral information, was used to confirm this. Cicerone et al. have moreover used their improved broadband CARS system to image healthy murine liver and pancreas tissues and brain tumor lesions surrounded by healthy brain matter with great success.[131]

SRS has also been used to distinguish different cell compartments in live cells.[171] Figure 11 demonstrates how SRS was used to image live salivary gland cells of *Drosophila* larvae. Xie et al. observed that nucleic acids have very weak Raman peaks compared to lipids and proteins and therefore DNA imaging can be challenging. However, the *Drosophila* larvae used in their study is a good model for DNA imaging, since they have a very high DNA concentration. As a matter of fact, they were able to distinguish lipids using a Raman peak at 2845 cm^{-1}, proteins at 1655 cm^{-1} and DNA content at 785 cm^{-1} and 1090 cm^{-1}. It was even possible to study the DNA structure in such a manner that closely packed chromosomes could be visualized.

The previous examples show that CARS and SRS microscopies have been used quite extensively in biomedical applications. These applications include single cell imaging with visualization of cell organelles and changes during culturing with different media. Also, different disease models have been used in CARS microscopy studies that could reveal diseased lesions over normal tissue and new information about the progress of disease. The information obtained from such studies can support the development of new medications when knowledge of cellular processes and disease progression is increased. However, the applications where CARS microscopy have been used to image drug or drug nanoparticles within biological specimens are still limited, and mostly materials that give strong FWM signals have been used as proof-of-concept studies. These materials include gold,[119] silicon,[145] diamond[55] and deuterated materials.[172]

Pope et al. used CARS microscopy to probe nanodiamonds in fixed and living HeLa cells by using the sp^3 vibrational resonance of diamond.[55] They showed that theoretically single nanodiamonds even as small as 27 nm in diameter could be imaged using CARS microscopy. FWM microscopy based on electronic excitation has been used to image nanostructures, such as gold nanoparticles,[119] silicon nanoparticles[145] or zinc oxide nanocrystals[144] in biological matrices. Garret et al. used FWM microscopy to image gold nanoshells (GNSs) by probing the electronic excitation of gold material.[119] GNSs of diameter less than 200 nm were detected inside live RAW 264.7 macrophage cells and human epidermoid carcinoma cells (A431). GNSs were imaged in the epi-direction, while the CARS signal due to the CH_2 molecular stretching was detected in forward direction simultaneously. Garret et al. have also imaged deuterated quaternary ammonium palmitoyl glycol chitosan (dGCPQ) nanoparticles using CARS microscopy in various organs after intravenous injection and oral administration.[108,172] Deuteration is one approach to change the molecular vibrations of materials, so that CARS peaks occur outside the biological CH stretching region. Deuterated nanoparticles give a strong CARS signal at 2100 cm^{-1} due to CD_2 stretching. In these studies, Garrett et al. first visualized dGCPQs in the liver after intravenous dosing showing particle uptake in the blood vessels, and intracellular spaces between hepatocytes and within Kupffer cells. Images taken after oral administration, revealed that particles were not transported across villi, but accumulated in the jejunum mucus. Particles were also found in the brain parenchyma after oral administration which suggested that dGCPQ nanoparticles could increase brain uptake of drugs due to the increased residence time at the blood brain barrier. In later studies, dGCPQs were found to be taken up by enterocytes in the gut from where they passed into the blood stream and were transported to the liver prior to recirculation via bile in the gall bladder to the small intestine.

As mentioned previously, the detection of free drug in cells is a demanding task. However, coherent Raman imaging has high potential for this purpose and one of the current goals of coherent Raman imaging in pharmaceutical/biomedical applications is the detection of low concentrations of drugs in cells. Xie et al. have shown that by using hyperspectral SRS imaging it was possible to detect tyrosine kinase inhibitors inside lysosomes of live cells (BaF3) even at concentrations as low as 4 μM.[142] They could also detect the enrichment of the imatinib and nilotinib concentrations by over 1000 fold in lysosomes. Furthermore they showed that lysosomal trapping of nilotinib was reduced more than tenfold when the drug was administered with chloroquine. This study beautifully demonstrates the potential of novel coherent Raman techniques in studying drug-cell interactions and drug-drug interactions in a quantitative manner. The detection limit may potentially be lowered still further by using for example Raman tags based on alkyne groups. The potential of SRS imaging with alkyne tags[173] has already been demonstrated in studies where biological processes including glucose uptake,[174] DNA[175,176] and lipid[73] synthesis have been visualized. Wei et al. have taken Raman tag development to a whole new level by creating a Raman dye palette of 24 resolvable colors, each having distinctive Raman peaks, based on triple-bond conjugates, and, with an immunostaining approach, they could use this technique to follow DNA and protein metabolism under physiological and pathological conditions in neuronal co-cultures and brain tissue.[177]

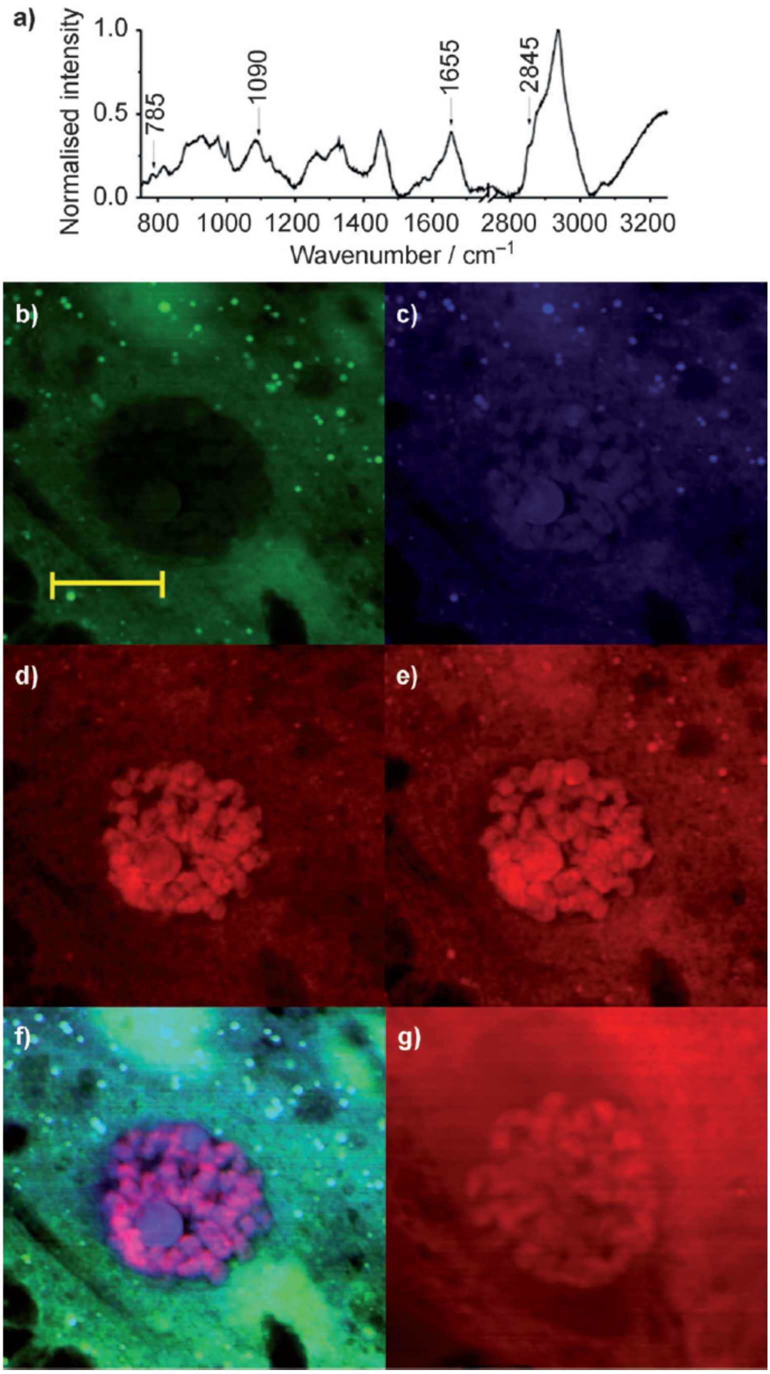

Figure 11. SRS imaging of live salivary gland cell of *Drosophila* larvae. a) Raman spectrum of a Drosophila cell. b–g) SRS images of a salivary gland cell, via the stimulated Raman loss detection scheme. b) Lipid-specific image taken at 2845 cm^{-1}, c) Amide I band at 1655 cm^{-1}, d) nucleic acids at 785 cm^{-1} and e) 1090 cm^{-1} . f) Multicolor image generated by combining images (b)–(e). g) Nucleic acid map recorded at 785 cm^{-1} via the stimulated Raman gain detection scheme. The scale bar is 20 mm. Each image has the size of 512 × 512 pixels. Reprinted from reference[171] with permission. Copyright (2012) Wiley.

Most of the purely pharmaceutical applications of non-linear optical imaging are studies where different types of dosage forms have been imaged for visualizing the distribution of chemical components or drug release and solid-state changes under dissolution.[24] As with spontaneous Raman imaging/mapping, coherent Raman techniques have been used to visualize different chemical components, including API in varied pharmaceutical dosage forms: inhalation powders,[178] microparticles[179] and tablets.[116] Hartshorn et al. used broadband CARS to visualize indomethacin tablets consisting of varied ratios of excipients: lactose monohydrate, Avicel (microcrystalline celluloce, MCC), croscarmellose sodium, magnesium stearate and gamma, and alpha solid-state forms of indomethacin.[116] They compared their broadband CARS measurements to wide-field Raman imaging and confocal Raman measurements. They demonstrated the benefits of rapid CARS microscopy over slower spontaneous Raman measurements, since they could successfully map different chemical components on tablet surfaces with broadband CARS with a data-acquisition time 10-100 times faster than spontaneous Raman spectroscopy. They also found unexpected spectra on some regions, which they thought originated from amorphous indomethacin that had formed due to the tableting process. A similar study, also visualizing API and excipients on tablet surface was performed by Slipchenko et al. They used SRS and CARS with comparison to confocal Raman imaging to image amlodipine besylate tablets manufactured by different companies. They showed that SRS offered 10^4 times higher data-acquisition time compared to spontaneous Raman microscopy.

Tablets under dissolution have also been visualized using CARS microscopy with a series of experiments using theophylline as a model drug.[180,181] First lipid based tablets made of theophylline and tripalmitin were imaged under dissolution.[180] It was shown that theophylline anhydrate converted to monohydrate, which can exhibit the dissolution of theophylline, when tablets made of powdered lipid material were prepared. This conversion was not observed when, extrudated lipids were used as starting material. These studies were continued, combining inline UV absorption spectroscopy with this analysis.[181] CARS microscopy revealed the theophylline anhydrate conversion to monohydrate, and UV absorption spectroscopy confirmed the results of a decreased dissolution rate. In addition to drug release from tablets, CARS microscopy has been used to image drug release from polymeric matrices.[182] Paclitaxel (PTX) release from poly(ethylene glycol)/poly(lactic-co-glycolic acid) (PEG/PLGA) blends was visualized. It was shown that the addition of PEG into polymeric matrix first initiated a burst release of PTX from surface, but after that PTX release was retarded and it was microscopically shown that PTX formed ring structures within PLGA polymeric matrix that effected retarded dissolution.

Figure 12 illustrates one example from the literature that combines CARS microscopy and SEM to image lactose carrier particles used as inhalation powders with API salmeterol.[178] It shows clearly the benefit of CARS microscopy as a chemically-specific imaging method. Lactose particles imaged with SEM do not directly give any information about the chemical composition of small particles on top of lactose carrier, whereas this information can be readily achieved with CARS microscopy and API can be distinguished from lactose carrier particles.

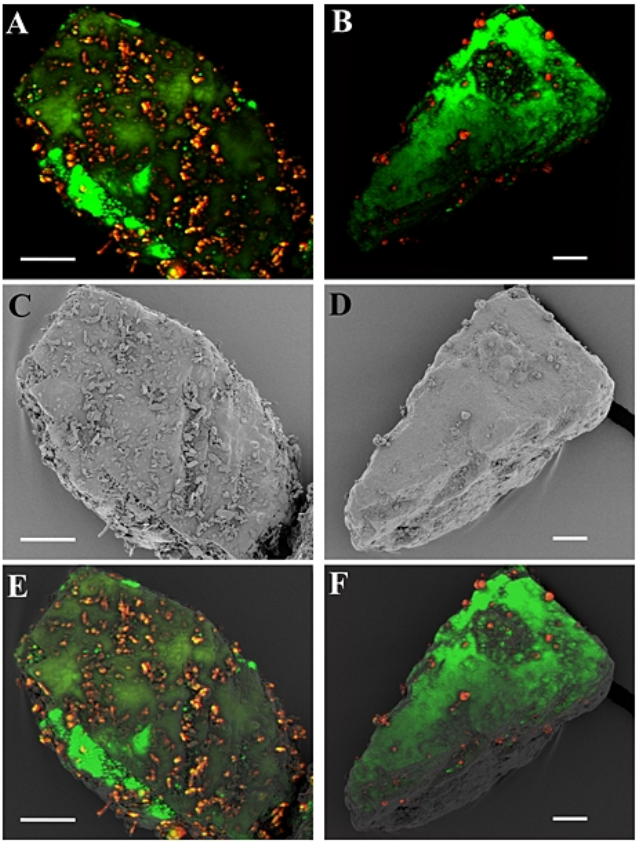

Figure 12. CARS and SEM imaging of lactose carrier particles used in dry powder inhalation formulation with salmeterol particles. (A+B) CARS, (C+D) SEM, and (E+F) correlative CARS and SEM images of salmeterol mixtures after 0.5 (left) and 600 min of mixing (right). Green color corresponds to lactose (2888 cm^{-1}) and red color corresponds to salmeterol (3050 cm^{-1}). Scale bars represent 20 µm. Reprinted from reference[178] with permission. Copyright (2014) Wiley.

In addition to coherent Raman microscopy, SHG has been used in pharmaceutical applications, since it can be used to differentiate crystalline and amorphous material, as well as some polymorphic crystalline forms (based differences in the presence/absence of centrosymmetry).[146,149,183] Prof. Simpson's group at Purdue University have used SHG quite extensively in their studies.[147,150,184] They have frequently employed an imaging setup with a femtosecond pulsed laser producing high peak powers that can be used to efficiently generate SHG signals. One important application has been the detection of the early stages of protein crystallization. An example of such analysis was demonstrated with green fluorescent protein (GFP) crystals.[150] SHG was successfully used to detect crystalline GFP proteins with lower background compared to TPEF. Simpson et al. have used SHG imaging to quantify crystallinity within nanosuspensions formulated with albumin-bound PTX.[149] In this study, crystals were detected with SHG and the location of SHG active crystals was marked for the subsequent confocal Raman analysis that was used to identify crystals as PTX. This method showed batch-to-batch variability and revealed water-insoluble PTX crystals up to 120 µm. SHG guided Raman microscopy and powder X-ray diffraction has also been used to differentiate clopidogrel bisulfate polymorphic forms I and II in powder mixtures.[185] This kind of complementary analysis can be beneficial, since the data obtained from different techniques can support each other. Furthermore, combinational approaches can also be used for rapid identification of multiple solid state-forms, since SHG screening, relying on detection of non-centrosymmetric crystals, is both very fast and highly sensitive, while for example, CARS, Raman and XRPD analyses can different some solid-state forms without relying on differences in centrosymmtery.

Table 3. Some examples of studies where non-linear optical imaging has been used to image biological samples and pharmaceuticals.

Non-linear imaging of biological samples

Method	Sample type	Study	References
Narrowband CARS	NIH/3T3 fibroblast cells, steroidogenic mouse adrenal cortical (Y-1) cells, 3T3-L1 fibroblast cells, human adipose-derived stem cells	Lipid droplet analysis: imaging lipid droplets under cells were differentiating, long term live cell imaging showing lipid droplets fusing, imaging lipid droplet motion in live cells, visualizing changes in lipid droplet configuration in infected cells	118,122,161,186
Multiplex CARS	HeLa and 3T3-L1 cells	Quantitative imaging of individual lipid droplets	163
Narrowband CARS	*Caenorhabditis elegans* worm	Lipid droplet content in genetically modified *Caenorhabditis elegans* worms were visualized aiming to study metabolic disorders	167
CARS, SHG, THG, SFG	yeast cells	Multimodal molecular imaging of live cells	187
Narrowband CARS	MIA PaCa-2 and HT29 cells	Different cellular components were visualized using CARS microscopy and hierarchical cluster analysis (HCA)	188
Narrowband CARS, TPEF	HeLa cells	CARS/TPEF was used to visualize biomolecules including proteins, lipids and nucleic acids during apoptosis	168
Broadband CARS	L929	Visualizing cell compartments including lipid droplets (CH_2 and C=C) and cell nuclei	128
Broadband CARS	human mesenchymal stem cells (hMSCs)	Different cell compartments were visualized in cells and quantitative CARS was used to monitor stem cell differentiation	189
SRS	salivary gland cells of *Drosophila* larvae	SRS fingerprint region imaging of nucleic acids, proteins and lipids in single cells	171
SRS	mouse brain tissue, mouse ear skin	Simultaneous two-color imaging of lipids and proteins	190
SRS	HeLa cells, nanodiamonds	SRS imaging of live cells using alkyne Raman tags, visualizing nucleic acid, proteins, lipids and glycan	73
Broadband CARS	HeLa cells, gold nanoshells	Visualizing single nanodiamonds in live cells	55

Narrowband CARS	mouse organs, deuterated quaternary ammonium palmitoyl glycol chitosan (dGCPQ) nanoparticles	Distribution of dGCPQs in different organs was visualized after i.v. and oral administration	108,172
FWM, CARS	RAW 264.7 macrophage cells	CARS and FWM microscopy was used to visualize gold nanoshells in live cells	119
SRS	BaF3 cells, tyrosine kinase inhibitors	SRS was used to visualize tyrosine kinase inhibitors accumulation in lysosomes of live cells in a quantitative manner and detection limit was as low as 4 µM	142
SHG, SFG, FWM	Human KB cells, ZnO nanocrystals	ZnO nanocrystals were visualized in the cells using SFG and FWM microscopy	144
Broadband CARS, SHG	murine liver tissue, murine pancreatic ducts, mouse brain gliobastoma	Spectral window of 500 - 3500 cm^{-1} was utilized to visualize healthy murine liver and pancreas and interfaces between healthy brain matter and xenograft brain tumours by probing nucleus, collagen and lipids	131
Narrowband CARS	brain tissue	Glioma was identified from healthy gray and white matter using CARS- based imaging techniques	191
Narrowband CARS, SHG	liver biopsies	Lipids and collagen was visualized in liver biopsies and automated image analysis method was developed to detect early fibrosis stage	153
Narrowband CARS	low density lipoprotein receptor-deficient (LDLR(-/-)) mouse and the ApoE lipoprotein-deficient (ApoE(-/-)) mouse	Atheroschlerosis was studied with mouse models, hyperspectral CARS imaging with PCA was used to visualize cholesterol crystals in mouse aortas	134
Narrowband CARS	mouse eyes	Meibomian glands were visualized using hyperspectral CARS imaging with PCA and distribution of lipids was accessed	133
Narrowband CARS	axonal myelin from guinea pigs	It was shown that myelin lipids are in the liquid ordered phase with water between bilayers of lipids	192
Narrowband CARS, TPEF	human eye	Trabecular meshwork cells (CARS shift at 2850 cm^{-1}) and surrounding collagen (TPEF) were visualized simultaneously	193

Non-linear imaging of pharmaceuticals

Method	Sample type	Study	References
Narrowband CARS	polymer films containing paclitaxel (PTX)	PTX distribution and release was visualized with concentration limit of 29 mM	182,194
Narrowband CARS	solid lipid microparticles (SLM) with lysozyme protein	Lysozyme protein distribution in SLMs prepared with different methods was imaged and the distribution data was used to explain drug release from SLMs prepared with different methods	179

SFG	tablets made of amorphous griseofulvin with and without excipients	Crystallization on tablet surface and in core of the tablet due to the compression and storage was studied by SFG microscopy combined to FTIR-ATR and SEM	[146]
Narrowband CARS	compacts of theophylline anhydrate and monohydrate and mixtures of these with lipids	CARS microscopy and hyperspectral CARS imaging were used to monitor theophylline anhydrate conversion to monohydrate and inline UV absorption spectroscopy analysis showed the decreased dissolution rate due to the conversion	[180,195,196]
Narrowband CARS	crystalline amino acids	Hyperspectral imaging method was developed and used to distinguish different amino acids from mixtures	[132]
Narrowband CARS	Silica microparticles loaded with itraconazole and griseofulvin	Hyperspectral CARS imaging was used to visualize the drug loaded in the silica particles and confirm that the solid state of the drug was amorphous	[197]
Broadband CARS	tablets with alpha and gamma indomethacin and excipients	Broadband CARS imaging was used to visualize the distribution different polymorphic forms of API and excipients on tablet surfaces	[116]
SHG	powdered griseofulvin	SHG (detection limit of 4 ppm crystallinity) was used to visualize the loss of crystallinity due to milling and recrystallization of amorphous griseofulvin achieved by milling and quench-cooling	[184,198]
SHG	lyophilized powder of albumin bound paclitaxel and aqueous suspension of that	SHG was used to locate the crystalline particles and Raman microscopy was used to confirm that these particles were paclitaxel	[149]

2.5 Conclusion of the literature review

It has been shown that non-linear optical imaging, including coherent Raman imaging with its label-free nature and chemical- and solid-state specificity, can be used in a wide range of applications including the biomedical and pharmaceutical sciences. Coherent Raman techniques have been extensively developed during the last couple of decades. Important developments are, for example, improved imaging speed, spectral and spatial resolution, signal-to-noise ratio and chemical-specificity.[130,199–201] A current trend in CARS microscopy is the development and application of broadband CARS microscopy. It offers a wide spectral range, with the fingerprint region as low as 500 cm^{-1} able to be used for data acquisition and quantitative analysis.[202] It also offers rapid imaging.[125,131,189] SRS is a very promising imaging technique.[99,135–137,203] It has certain benefits over CARS, since it lacks the non-resonant background and the signal scales linearly to concentration, facilitating quantitative analysis.[142,204] A very attractive prospect for the future is label-free coherent Raman imaging with subdiffraction resolution.[137] One way to achieve this, would be to use structured illumination techniques[205–207] or an additional doughnut-shaped Stokes beam could be used to saturate the SRS signal at the edges of the pump beam, analogous to the superresolution microscopy method STED.[208] Also, the surface enhanced Raman (SERS) phenomenon can be used with coherent Raman techniques to potentially image nanometer objects as small as single molecules.[209,210]

Many novel improvements, such as superresolution coherent Raman imaging, are still mostly at the theoretical level or their principles have just been demonstrated. In any case, the huge developments and present research will eventually lead to more affordable commercial instruments. An important aspect in such commercial imaging setups is user-friendliness. Also, to be able to fully benefit from non-linear optical imaging, it would be important that these microscopes could be used as multimodal non-linear microscopes combining coherent Raman and SHG, as well as fluorescence. Such microscopes could potentially offer a highly useful platform for scientists in diverse fields, including pharmaceutical development. They could also be used to reveal important information about cell functions and drug-and nanoparticle-cell interactions. Non-linear optical imaging could be also used to understand and monitor drug manufacturing processes, starting from solid-state characterization to monitoring, for example, powder mixing and tableting. In addition, drug release from drug products could be visualized and the chemically- and solid-state specific signal would also allow drug products to be monitored during storage and determine, for example, their solid-state stability.

Coherent Raman techniques alone will not diminish the value of other imaging and analytical techniques, rather the synergistic use of many improved techniques will reveal the smallest and subtlest secrets of cells and behavior of drug systems. Microscopy has been an attractive tool for scientists who have used it to visualize “invisible” objects since the 17th century. Since then, imaging techniques have developed from conventional light microscopy to fluorescence microscopy, and finally to superresolution microscopy, at least theoretically. Developments in imaging techniques and optics have also led to numerous Nobel prizes. For example, recently Jacques Dubochet, Joachim Frank and Richard Henderson were awarded in 2017 the Nobel Prize in Chemistry for their developments in cryo-electron microscopy (cryo-EM),[211] while the same prize was awarded to Eric Betzig, Stefan W. Hell and William E. Moerner in 2014 for their developments in super-resolved fluorescence microscopy. It is interesting to live in this era, when scientific developments are happening at such a fast pace. It seems that only the sky is the limit also for microscopy developments.

3 Aims of the study

The overall aim of this study was to evaluate the potential of label-free non-linear optical imaging, especially CARS microscopy, in pharmaceutical applications, including imaging of cells, cellular uptake of drug nanoparticles and solid-state analysis.

More specifically, the objectives were:

- To evaluate the potential for CARS microscopy to non-destructively image lipid structures and their changes in live cell cultures during culturing on membrane inserts as used in drug permeation studies. (**I**)

- To investigate the potential of label-free, chemical-specific CARS microscopy with the support of other non-linear optical imaging methods to probe unlabeled, non-fluorescent drug nanoparticles in cells and tissue. (**II**)

- To develop a correlative CARS and electron microscopy method to investigate unlabeled, non-fluorescent drug nanoparticle cellular uptake in more detail by combining the inherent benefits of label-free and chemically-specific CARS microscopy and the (sub)nanometer spatial resolution of electron microscopy. (**III**)

- To investigate the potential of multimodal non-linear optical imaging for spatially-resolved and solid-state specific analysis of pharmaceutical surfaces. (**IV**)

4 Experimental

4.1 Materials

*4.1.1 Materials in cell experiments (**I-III**)*

Cell culture medium solution Dulbecco's Modified Eagle's Medium (DMEM), fetal bovine serum (FBS), L-glutamine, non- essential amino acids (NEAA), Penicillin (100 IU/mL), Streptomycin (100 mg/mL) and trypsin were purchased from HyCLone, USA. Sodium pyruvate was purchased from ThermoFisher Scientific, USA. Ethylenediaminetetraacetic acid disodium salt dihydrate (EDTA), 2-[4-(2-hydroxyethyl)piperazin-1-yl]ethanesulfonic acid (HEPES), paraformaldehyde (PFA) and glutaraldehyde were acquired from Sigma-Aldrich, Germany. Osmium tetroxide and sodium cacodylate were purchased from Electron Microscopy Sciences (EMS), USA. Hank's balanced salt solution (HBSS) and phosphate-buffered saline (PBS), penicillin G 10000 I.U./ml and streptomycin 10 mg/ml (100×) solution (PEST) and CellMask® Orange were purchased from Life Technologies, USA. The 25 cm^2 and 75 cm^2 culture flasks and Transwell® inserts made from polyester (polyethylene terephthalate, PET) with a pore size of 3.0 µm, polycarbonate (PC) with a pore size of 3.0 µm, and collagen coated polytetrafluoroethylene (PTFE) with pore sizes of 3.0 µm and 0.4 µm, cell scrapers (catalog no. 3010) and Triton™ X-100 were obtained from Corning Inc., USA. Human colon carcinoma cells (Caco-2) and Raw 264.7 macrophage cells (ATCC® TIB-71™) were obtained from the American Type Culture Collection (ATCC), USA. Isotonic 0.4% w/v trypan blue solution was acquired from Lonza Ltd. (Basel, Switzerland). The glass-bottomed 24-well plates No. 1.5 and gridded glass-bottomed Petri dishes No. 1.5 were obtained from MatTek Corporation, USA.

*4.1.2 Drug materials (**II-III**)*

Paliperidone palmitate racemate (PP), paliperidone racemate (PAL) and the marketed PP nanocrystal suspension Xeplion® (PP-NC) were donated by Janssen Pharmaceutica NV (Beerse, Belgium) and used as received. Polysorbate (Tween®) 20 (TW20) was purchased from Applichem GmbH (Darmstadt, Germany). Glibenclamide (GLI) was purchased from Alpha Aesar (Karlsruhe, Germany) and hydroxypropylmethyl cellulose (HPMC) METHOCEL E5 Premium LV was purchased from Dow Chemical Company (Stade, Germany). Indomethacin (gamma form) was donated by Orion (Finland).

*4.1.3 Histological sections (**II**)*

Mounted, but unstained, paraffin sections (~5 µm) of formalin-fixed and paraffin-embedded rat i.m. administration sites 7 days after injection of PP-NC, as well as adjacent cryosections (~10 µm) of the same tissue sample, stained with Oil Red O and haematoxylin and eosin (H&E), were donated by Janssen Pharmaceutica NV.

4.2 Methods

*4.2.1 Cell culturing (**I-III**)*

Caco-2 cells were cultured in 25 or 75 cm^2 culture flasks in DMEM with 10% (v/v) heat inactivatedFBS, 1% (v/v) L-glutamine, 1% (v/v) NEAA and 1% (v/v) antibiotic mixture (final concentration of 100 IU/mL Penicillin and 100 mg/mL Streptomycin) (**I**). Cell passage numbers 31– 39 were used. The cells were passaged once a week. 0.5 mM PBS- EDTA and 0.25%

(w/v) trypsin-PBS-EDTA solutions were used for passaging the cells. For imaging experiments, the cells were seeded on Transwell® inserts with an initial density of 60,000 cells per 1 cm². Cells were cultured at 37 °C in a humidified atmosphere (95%) with 5% CO_2.

The RAW 264.7 cells (passages 40–44) were grown in culture flasks containing DMEM supplemented with 10% v/v heat inactivated FBS, 1% v/v L-Glu, 1% v/v NEAA and 1% v/v PEST and were maintained at 37 °C in an atmosphere of 5% CO_2 in humidified air. The cells were passaged every 2–3 days before a confluency that was too high was reached using a 0.25% w/v trypsin–EDTA (0.5 mM) solution in PBS, followed by centrifugation for 5 min at 1000g and resuspension in DMEM. The viability of the cells was determined using the trypan blue exclusion method and was higher than 85% (**II**).

Another approach to culture the RAW 264.7 murine leukemia monocyte–macrophage cell line (passage numbers below 10) was to use cell scrapers for detaching the cells (**III**). Raw 264.7 macrophage cells were cultured in 37 °C and 5% CO_2. Cells were grown in a 75 cm² cell-culturing flask and passaged every 2-3 days. Cell culture medium solution consisted of DMEM with 10% v/v heat inactivated FBS, 1 % v/v L-Glu, 1% v/v NEAA, 1% v/v PEST and Sodium pyruvate (1% in total). Cells were passaged using cell scrapers so that cells were washed twice with DMEM and 10 ml of DMEM was added into flask prior to scraping the cells gently so that they were detached. Approximately 1 ml of cell suspension was added to a new culturing flask with a total amount of 13 ml of DMEM.

4.2.2 *Preparation of nanocrystal suspensions* (**II-III**)

PP nanocrystal (PP-NC) suspension was a marketed product (Xeplion®, Janssen Pharmaceutica NV, Beerse, Belgium) (**II**). GLI nanocrystal (GLI-NC) suspension was prepared via media milling using a Dispermat® SL-C 5 bead mill (VMA Getzmann GmbH, Germany) (**III**). Suspension medium was double-distilled water (FinnAqua 75, San Asalo-Sohlberg Corp., Helsinki, Finland) and the suspension was stabilized with (HPMC) 10%wt related to drug amount. The milling time was 320 min and milling was performed in circulation mode with a pump speed of 70 mL/min and rotor speed of 4000 rpm using silica beads with a size of 1-1.2 mm. The batch size was 100 g with 10 g of glibenclamide.

4.2.3 *Preparation of indomethacin solid-state forms (**IV**)*

The gamma form of indomethacin (Orion, Finland) was used as received. The alpha form was prepared by dissolving 3 g of the gamma form in 20 ml of ethanol with continuous stirring at approximately 80°C in a covered vessel. The warm solution was then filtered into a beaker with 40 ml of MilliQ water. The resulting slurry was vacuum filtered and dried, first for one hour in a vacuum oven and then overnight over phosphorus pentoxide in a desiccator. The resulting alpha form was gently ground with a mortar and pestle.[212] The amorphous form was prepared by complete melting of the gamma form on an aluminium pan at 165°C on a hot plate, followed by quench cooling of the melt on a cold metal surface at room temperature and equilibration at room temperature over phosphorus pentoxide in a desiccator. The glass film was then scraped from the pan and gently ground with a mortar and pestle. The amorphous form was used within 24 h of preparation.

4.2.4 *Preparation and storage of indomethacin tablets (**IV**)*

Tablets (300 mg, 13 mm diameter) were compressed with a hydraulic press (Specac, Kent, UK) using a weight equal to 1 ton for 30 seconds. Mixture tablets used in the first part of the study consisted of equal amounts (1:1:1 w/w) of gamma, alpha and amorphous indomethacin.

Tablets used for monitoring crystallization were prepared from pure amorphous indomethacin. The bottom side of each tablet was imaged. The crystallization behavior of amorphous indomethacin tablets was studied at 30°C and two different humidities: 23% RH and 75% RH. The tablets were placed in open glass vials in desiccators with the bottom surface exposed to the air. Desiccators with saturated salt solutions — potassium acetate and sodium chloride — were used to create 23% RH and 75% RH, respectively. Eleven tablets were prepared in total. A freshly made tablet was used as the day 0 sample. For the other time points — days 1, 2, 5, 7 and 22 — a separate tablet from each of the two desiccators was used for each time point.

The stored tablets were analyzed by visual inspection, SEM, FTIR-ATR spectroscopy, Raman microscopy and CARS and SFG/SHG imaging. Each of the tablets was analyzed in triplicate from three different surface sites. Simca software (v.14.1, Umetrics, Umeå, Sweden) was used to perform pre-processing (SNV transformation and mean centering) and PCA on the FTIR and Raman spectra.

*4.2.5 Scanning electron microscopy (SEM) (**III-IV**)*

SEM was used to visualize GLI crystals after milling to confirm that the milling resulted in nano-sized crystals (**III**) and as a complementary method to visualize different solid-state forms of indomethacin powders and to monitor solid-state changes on indomethacin tablet surfaces over a 22 day period (**IV**). FEI Quanta 250 Field Emission Gun Scanning Electron Microscope (FEI, USA) was used to image coarse GLI powder and GLI-NCs as well as different solid-state forms of indomethacin and indomethacin tablet surfaces. The samples were mounted on aluminium stubs covered with carbon tape and then coated with a thin layer of platinum. Micrographs were taken under low vacuum (coarse GLI) or high vacuum (GLI-NCs), with a 10 kV beam and a spot size of 4 (arbitrary units).

*4.2.6 Fourier-transform infrared spectroscopy (FTIR) (**IV**)*

FTIR was carried out using a Vertex 70 FTIR spectrometer (Bruker Optics, Germany) with a MIRacle ATR accessory containing a diamond single-bounce crystal (Pike Technologies, USA). The spectra were collected between 650 and 4000 cm^{-1} with a spectral resolution of 4 cm^{-1}. All spectra were the average of 256 scans with the background signal (blank crystal) subtracted (Opus software). For each sample, spectra were collected in triplicate.

*4.2.7 Raman spectroscopy (**II-IV**)*

Raman spectroscopy was used to identify suitable Raman peaks prior to CARS microscopy (**II-IV**). In addition Raman spectroscopy was used to further confirm the crystalline solid-state structure of milled nanocrystals (**II-III**) and the purity of different solid-state forms of indomethacin (**IV**). Raman spectroscopy was also used as a complementary method to monitor the surface crystallization of indomethacin tablets over 22 days of storage (**IV**).

Raman spectra of the undiluted aqueous PP-NC suspension, the air-dried PP-NC drug product, pure PP and PAL, as well as TW20 were recorded at room temperature using a LabRAM HR800 confocal Raman microscope (Horiba Jobin Yvon SAS, Palaiseau, France) equipped with a 100× objective (**II**). The system was calibrated using the 2853 cm^{-1} Raman band of cyclohexane. The zero Raman shift position was routinely checked to exclude any drift or fluctuation of the Raman shifts. The spectra were generated at 785 nm in the 200 cm^{-1} to 3300 cm^{-1} range with a spectral resolution of 2 cm^{-1} using the multi-window mode and an acquisition time of 50 s for each window. All spectra were normalized to their respective maximum intensity over the recorded 2800–3000 cm^{-1} spectral region.

Raman spectra of GLI, GLI-NCs and HPMC (**III**) as well as solid-state forms of indomethacin and indomethacin tablet surfaces (**IV**) were measured using a TimeGated® 532 instrument (TimeGated® 532, TimeGate Instruments, Oulu, Finland). This instrument consisted of a 532 nm picosecond pulsed laser (pulse width < 100 ps, repetition rate of 40-50 kHz, average output power of 20-40 mW), sampling optics (fiber), spectrometer with a time-gated complementary metal-oxide semiconductor (CMOS) single-photon avalanche diode (SPAD) detector and a computer with MATLAB-based measurement software (MathWorks, Massachusetts, USA). The powders were analyzed with a sampling probe (BAC100 Raman Probe, B&W Tek, Delaware, USA) by placing the samples on a metal wafer that was rotated at a constant speed while measuring the spectrum. The tablet surfaces were measured by focusing the laser beam on the tablet surface through a 40× microscope objective with an NA of 0.75 (Olympus, Tokyo, Japan). The Raman spectra of the tablet surfaces during the crystallization study were the average of spectra measured from three different spots on each of the tablets.

*4.2.8 Cell viability tests for nanocrystal uptake studies (**II-III**)*

CellTiter-Glo® Luminescent Cell Viability Assay (Promega Corporation, USA) was used to measure cell viability after incubating the cells with GLI-NC suspensions in DMEM. Briefly, 50 000 cells per well on 96- well plate (Corning Inc., USA) were seeded and allowed to attach overnight. The next day, cells were incubated with GLI-NC suspensions in DMEM with concentrations of 100 µg/ml, 250 µg/ml, 500 µg/ml, 750 µg/ml, 1 mg/ml and 2 mg/ml for 6 h. Cells were washed with HBSS-HEPES (10 mM HEPES concentration) pH 7.4 buffer solution and 50 µl of CellTiter-Glo® reagent was added to each well containing 50 µl of HBSS-HEPES buffer prior to shaking the plate for 2 mins and measuring the luminescence signal after 15 mins with a Varioskan Flash reader (Thermo Fisher Scientific Inc., USA).

The same assay was used to measure cell viability after incubating the cells with PP-NC suspensions (**II**). The incubation time was 3 h and PP-NC suspensions at concentrations of 50, 100 and 250 µg/ml in phenol red-free DMEM were used.

*4.2.9 Sample preparation for cellular uptake studies (**II**)*

A volume of 1 ml of cell suspension (RAW 264.7) with a concentration of 3.1×10^5 cell/ml was added to wells in a glass-bottomed (No. 1.5) 24 well plate and allowed to attach to the bottom of the well plate overnight. The next day, 1 ml of diluted PP suspension (250 µg/ml in 10mM HBSS-HEPES pH 7.4) was added and cells were incubated with suspension in 37 ˚C and 5 CO_2 for 6 h and 24 h. For imaging fixed RAW 264.7 cells, the cell membrane was first stained with fluorescent dye CellMask® Orange to facilitate cell membrane visualization. First, excess particles were removed and cells were washed with 10mM HBSS-HEPES pH 7.4 buffer solution and then 500 µl of freshly diluted plasma membrane stain at a concentration of 5 µg/ml in PBS was added to each well and incubated at 37 °C for 5 min. The staining solution was removed and the cells were fixed in 4% w/v PFA in PBS for 10 min. The cells were rinsed twice and kept in 0.5–1.0 ml of HBSS for imaging. Cellular uptake studies of GLI-NCs were performed as described in the workflow for correlative CARS and EM studies in Section 4.2.10.7 (**III**).

*4.2.10 Multimodal imaging (**I-IV**)*

*4.2.10.1 Microscope setup (**I-IV**)*

The microscope used for non-linear imaging and confocal fluorescence and bright field (BF) light imaging was a commercially available fully-integrated Leica TCS SP8 CARS microscope with the image acquisition software Leica Application Suite Advanced Fluorescence (LASAF). A heated environmental chamber built over the microscope with a controlled CO$_2$ supply (37 °C and 5% CO2) was used for maintaining the live cell cultures during imaging. The system consists of an inverted microscope equipped with a laser-scanning confocal scan-head and photomultiplier tube (PMT) and GaAsP hybrid (HyD) photodetectors (Figure 13). The CARS signal was separated from other signal components (e.g. second harmonic generation, SHG) using bandpass filters at 560–750 nm or 645–850 nm and detected in the forward direction (f-CARS) or backward direction (epi-CARS) using non-descanned PMT detectors. SHG signals were also detected in the forward direction (f-SHG) or backward direction (epi-SHG) using bandpass filters at 465 nm ± 85 nm. SHG and SFG peaks were also detected by measuring the second order non-linear spectra detected using a HyD detector as described in the next section. A water-immersion 25 × objective with an NA of 0.95 (Leica HCX IR APO L 25 × /0.95 W) was used in all experiments. The CARS excitation source was a Nd:YVO4 solid-state-laser (APE GmbH, Germany) with an optical parametric oscillator (OPO). The Stokes beam (ω_S) had a fixed wavelength of 1064.5 nm and a pulse duration of 7 ps. The bandwidth was about 2–3 cm^{-1} and the repetition rate was 80 MHz. The pump and probe beams (ω_p and ω_{pr}) at 781–827 nm were generated from the OPO with a pulse duration of 5–6 ps. The excitation light beams were linearly polarized (extinction ratio of 100:1) and co-polarized with respect to each other.

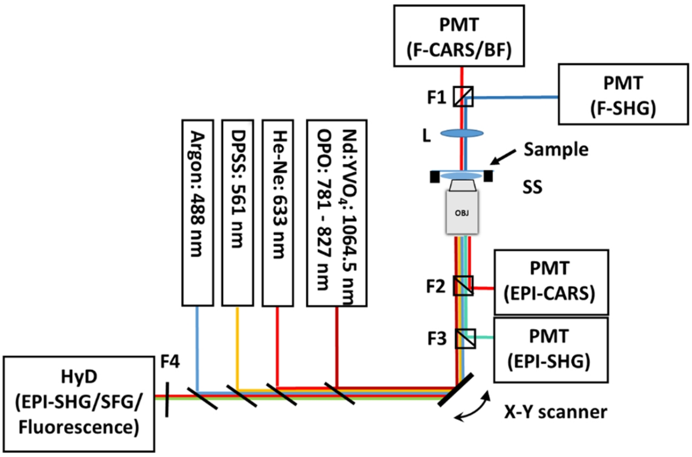

Figure 13. Schematic figure of imaging configuration and the laser lines used in studies in this Thesis. OBJ: microscope objective, (25 ×, N.A. 0.95), SS: scanning stage with galvanometric z-scanner, L: condenser lens (N.A 0.55), F1, F2 and F3: dichroic mirrors and band-pass filters for f-CARS/BF, f-SHG, epi-CARS and epi-SHG channels, PMT: photomultiplier tube, Nd:YVO4: 80 MHz pulsed solid-state fundamental laser, OPO: optical parametric oscillator, F4 tunable band-pass filter, HyD: GaAsP hybrid detector.

For the BF imaging a He/Ne laser with a wavelength of 633 nm and power below 0.1 mW was used for detecting the transmitted light using a PMT detector. An argon laser with a wavelength of 488 nm and DPSS laser with a wavelength of 561 nm were used in fluorescence based assays evaluating the cell viability after CARS laser exposures as described in Section 4.2.10.4, Evaluation of cell viability after CARS imaging (**I**). TPEF was used to detect the cell membranes of stained RAW 264.7 macrophage cells in nanocrystal uptake studies and a 1064.5 nm laser was used to excite the molecules, with a HyD (550-650 nm) detector used to detect the fluorescence

*4.2.10.2 Non-linear spectroscopy (**I-IV**)*

CARS spectra from DMEM with and without phenol red, HBSS, and PBS were measured to find the optimal media solution for imaging the cells (**I**). A drop of each solution was placed on glass coverslips, which were then scanned in the yz-plane in order to acquire CARS signal from both the sample and the coverslip. The spectra were recorded from 2698 cm^{-1} to 3410 cm^{-1} by tuning the pump laser step-by-step 71 times during a spectral scan. The sample spectra were normalized to the spectrum of the coverslip. Since glass only generates a non-resonant CARS signal, it was possible to cancel out the intensity variations due to the laser power fluctuations and the wavelength-dependent detection efficiency. The same spectral region was also used to measure the CARS spectrum of live Caco-2 cells grown on membrane inserts (**I**). CARS spectra of pure PAL and PP, the air-dried PP-NC and TW20, as well as blank RAW 264.7 cells were recorded by changing the wavelength of the pump beam with steps of 10 cm^{-1} for the energy difference to match Raman shifts from 2760 to 3000 cm^{-1} for the pure compounds and 2760 to 3100 cm^{-1} for the incubation constituents (i.e. RAW 264.7 cells, diluted PP-NC and blank HBSS) (**II**). Spectra were recorded with the same instrumental parameters (laser powers and f-CARS PMT gain). The signal intensities in each average spectrum were normalized to their respective maximum intensities over the recorded spectral region. The maximum intensity was set to 1 (i.e. maximum of an arbitrary scale ranging from 0 to 1). For measuring the CARS spectra of GLI, GLI-NCs, and HPMC, a small amount of powder or suspension was placed on a glass coverslip and the wavelength of the pump laser was changed from 797 nm to 821 nm with 41 steps (2786 – 3153 cm^{-1}) (**III**). The same region was also used to measure the CARS spectra from the inside of the cells (**III**). For measuring the CARS spectra of different solid-state forms of indomethacin (amorphous, alpha, gamma) powders or tablets (1:1:1 w/w gamma, alpha, amorphous or tablets made of amorphous indomethacin and stored at 30 °C in 23% RH or 75% RH) were placed on a glass coverslip and CARS spectra (epi-CARS) were measured between 1413 cm^{-1} and 1800 cm^{-1} by systematically tuning the wavelength of the pump laser 33 times (893.3 nm – 925.3 nm) (**IV**).

The second order non-linear spectra containing the SFG and SHG signals were recorded by exciting the sample with the Stokes wavelength of 1064.5 nm and a pump wavelength of 901.3 nm while collecting the emitted photons with a HyD detector from 400 nm to 700 nm by changing the detection range in 10 nm steps (**IV**). In this way, a spectrum containing the three SFG/SHG signals could be obtained, with the predicted SHG signals at 451 nm and 532 nm and the SFG signal at 488 nm calculated as:

$$\lambda_{SFG} = \frac{1}{\frac{1}{\lambda_1}+\frac{1}{\lambda_2}} , \tag{14}$$

where λ_1 and λ_2 are the irradiation wavelengths. The positions of the peaks and absence of a broader background signal were used to confirm that the detected signal originates from SFG/SHG (and therefore crystalline material) rather than the less solid-state specific two-photon excited fluorescence (TPEF) (the intensities of the second order signals were not calibrated for the detectors' spectral response). The spectral data was collected using a Leica

Application Suite Advanced Fluorescence (LASAF) and processed with OriginPro 8.6 (OriginLab, Northampton, Massachusetts, USA) and, in the case of hyperspectral imaging, with MATLAB R2016a (MathWork, MA, USA).

*4.2.10.3 Suitable insert materials for CARS imaging of live Caco-2 cell cultures (**I**)*

The durability of different membrane insert materials to CARS lasers and the optical properties of inserts were evaluated to find the best insert for CARS imaging. Commonly available Transwell® inserts (Corning Inc., USA) made from three different materials, PET, PC and collagen–coated PTFE, were imaged. The inserts were placed on a coverslip while being imaged. Z-stacks covering the entire thickness of the insert membrane were acquired at 2860 cm^{-1} with increasing laser powers until visible damage was observed. Inserts were imaged dry as well as after the addition of HBSS-HEPES buffer solution on the apical side to see if the buffer changed the optical behavior of the insert materials and image quality. BF images of the inserts were taken before and after CARS imaging. The CARS experiments were performed with laser powers of up to 100 mW for the pump/probe beam and 50 mW for the Stokes beam, corresponding to a maximum peak power density of ~0.14 TW/cm^2 within the diffraction limited spot. The incident powers were measured by a photodiode power sensor (S170C, Thorlabs Inc., USA). The effective beam areas, A_{eff}, were calculated as:

$$A_{eff} = \pi w^2/2, \tag{15}$$

where w is the $1/e^2$ beam radius of the Gaussian fit to the Airy disk (w = 0.687r; Rayleigh limit r = 0.61λ/NA, where λ is the excitation wavelength).

*4.2.10.4 Evaluation of cell viability after CARS imaging (**I**)*

The effect of CARS imaging on cell viability was investigated at 37°C and 5% CO_2. The cells were seeded on glass-bottomed 24- well plates at a density of approximately 325 000 cells/well and incubated overnight to allow the cells to attach to the bottom of the wells. The cells were imaged using CARS microscopy the next day. Cells were exposed to the CARS lasers at different powers and for different durations. BF images were recorded before and after exposure to the lasers to detect any changes in cellular morphology.

To attain further information about the effect of laser irradiation on cell viability, a fluorescence assay was performed using the CytoSelect™ Cell Viability and Cytotoxicity Assay Kit (Cell Biolabs, Inc., USA, Catalog Number CBA-240). The kit contains an acetoxymethyl derivate of calcein (Calcein AM) and ethidium homodimer (EthD-1) fluorescence dyes. Live cells convert the non-fluorescent Calcein AM to the highly fluorescent calcein, which remains within the cells. EthD-1 is a fluorescent stain that can only penetrate damaged cell membranes and fluoresces strongly when bonded to ssDNA, dsDNA, RNA, oligonucleotides and triplex DNA. Thus, it was used to detect dead cells. Before performing the assay, CARS z-stacks with different laser powers (20–100 mW for the pump beam and 10–50 mW for the Stokes beam in the focus) were recorded of the Caco-2 cells. Z-stacks were recorded so that they covered the entire thickness of the cells in the field of view. The number of steps in the z-stack was 45 and the step size was 0.57 µm. Images with 512 × 512 pixels were recorded using a 2× zoom, producing a scanning area of 232 × 232 μm^2. A scanning speed of 400 Hz (line average 2) was used, resulting a pixel dwell time of 1.20 µs and a frame rate of 0.386 frames/s. After recording each CARS stack, the medium was removed from the wells and 400 µL of fluorescence dye containing Calcein AM and EthD-1 (diluted in HBSS-HEPES, 1:500) was added per well. The cells were then incubated for 30 min at 37°C. After incubation, the excess stain was removed by washing the cells twice with HBSS-HEPES buffer solution. The cells were kept in buffer while imaging the cell viability. HyD- detectors were used for imaging the green fluorescence signal from calcein and the red fluorescence signal from EthD-1. For the negative control, the cells were incubated with HBSS-HEPES buffer solution without exposure to the CARS lasers. For the positive controls indicating dead cells, the cells were incubated with Saponin (diluted in HBSS-HEPES, 1:100) or 1% Triton™ X-100 in HBSS-HEPES for 10 min and imaged afterwards in the same manner as the samples that were exposed to different CARS laser powers.

*4.2.10.5 Imaging of PP nanocrystal cellular uptake (**II**)*

For the imaging of fixed RAW 264.7 macrophages with PP-NCs, three representative regions (ROIs) in each well were observed at low (1.5×; 1024 ×1024 pixels; pixel size 302 nm) and high (6.5×; 512 × 512 pixels; pixel size 140 nm) digital magnification consecutively in BF, TPEF and f-CARS modes. BF transmitted light was detected with the f-CARS detector (gain 200 V). The CARS signal was generated using a 817 nm pump beam (ω_p, 71mW in focus at the sample) and 1064.5 nm Stokes beam (ω_s, 64mW in focus at the sample), while probing with the pump beam. The f-CARS signal of PP was recorded (gain 650 V) at 2845 cm^{-1}. The 1064.5 nm laser (21 mW in focus at the sample) was used to generate the TPEF signal originating from the cell membrane stain, which was recorded with the 550–650 nm HyD- detector (gain 100%). Because of the inherent confocality of the CARS and TPEF processes, z-stacks were recorded covering the thickness of the macrophage monolayer (~25 µm) with fixed increments of 0.5 µm. Each frame from the z-stack was alternatively scanned in the TPEF and f-CARS modes prior to reiteration in the next frame. Single CARS or TPEF 512 × 512 pixels xy-scans taken over the full field of view were obtained within 3 s, while the total acquisition times for combined CARS/TPEF 512 × 512 pixels × 25 µm z-stacks with 0.5 µm z-step size approximated 5 min.

Imaris (Bitplane; Zurich, Switzerland) was used for rendering the three-dimensionally reconstructed data sets. The physical dimensions and frequencies of cellular components and/or drug particles were obtained from direct measurements of the CARS-positive (2845 cm^{-1}) bodies, based on quantitative image analysis of the maximum projection images (xy-frames projected in z-direction) of a number of representative three-dimensional recordings. The "Analyze Particles" algorithm in the ImageJ software v1.47 (U.S. National Institutes of Health, Bethesda, Maryland, USA) was applied after scale setting, brightness/contrast adjustment and thresholding. All detailed images used for image analysis (i.e. field of view 71.5 µm × 71.5 µm) were acquired with a 140 nm pixel size (25× objective magnification; 6.5× zoom factor; 512 × 512 pixels), ensuring that the pixel size would not be the resolution-limiting factor. The reported particle sizes and frequencies represent the mean values of three independent image analysis runs.

PP-NC cellular uptake was also studied with live RAW 264.7 macrophage cells. These studies were performed with the cells kept in DMEM at 37 °C and 5% CO_2 for acclimatization until removal of medium and adding diluted PP-NC suspension while cells were still on the microscope stage. The f-CARS and BF imaging modalities for living cells were identical to those for the fixed cells. Focused BF images and f-CARS xy-scans were captured with 3 min intervals during 120 min following addition of the drug nanocrystals, and f-CARS z-stacks covering the thickness of the cell monolayer were recorded at the end of the incubation.

*4.2.10.6 Imaging histological sections with PP nanocrystals (**II**)*

The BF and f-CARS imaging modalities were analogous to those for fixed cells. The f-SHG signal was generated using the 817 nm pump beam (ω_p, 71mW in focus at the sample) and recorded using a PMT detector gain of 650 V. Larger areas of interest were imaged as separate tiles and stitched to create overview images using the LASAF software.

*4.2.10.7 Workflow for correlative CARS and EM studies (**III**)*

RAW 264.7 macrophage cells (approximately 100 000 cells/well) were seeded on gridded glass-bottomed Petri dishes (MatTek, No. 1.5, 35 mm, 13 mm glass) and allowed to attach to the bottom of the dish overnight. GLI-NC suspension diluted to a concentration of 250 µg/ml in DMEM (1 ml) was added and cells were incubated in 37°C and 5% CO2 with suspension for 6 h. Excess particles were removed and the cells were washed twice with DMEM. Cell membranes were stained with CellMask® Orange plasma membrane stain (5 µg/ml in DMEM) by incubating the cells in 37°C and 5% CO_2 with 1 ml of stain for 5 mins. The stain was removed and cells were fixed with 2% glutaraldehyde in 100 mM sodium cacodylate buffer for 30 mins at RT. Sodium cacodylate was replaced with HBSS-HEPES (HEPES concentration 10 mM) pH 7.4 buffer solution and cells were imaged first with the Leica TCS SP8 CARS microscope. BF images were recorded showing the grid markings. These images could be used to locate the same cells for the preparation of TEM sections and imaging with TEM. CARS/TPEF imaging of the cells were performed so that z-stack images over the cells were recorded (step size 0.5 µm, CARS shift 3080 cm^{-1}, average powers at the focus approximately 30 mW for the Stokes beam and 43 mW for the pump/probe beam). In addition, CARS spectra from the inside of the cell were measured by systemically tuning the pump laser 41 times obtaining the spectrum between 2785 and 3150 cm^{-1} CARS shifts. Then, cells were post-fixed with 1% reduced osmiumtetroxide in 100 mM Na-cacodylate buffer, pH 7.4 for 1 h at RT, dehydrated with graded series of ethanol (70%, 96%, 100%), incubated with transitional solvent acetone and flat-embedded in Epon.[213] 120 nm thick sections in parallel orientation were then cut from the block face using Leica UCT ultramicrotome from the area selected, based on the BF images showing the grid markings. Sections were post-stained with uranyl acetate and lead citrate and imaged with Jeol JEM-1400 TEM (Jeol Ltd., Tokyo, Japan) transmission electron microscope with Gatan Orius SC1000B bottom- mounted CCD-camera using a 80 kV beam. The entire cells were sectioned and imaged allowing us to compare the entire cells imaged with both imaging techniques. For the TEM imaging of GLI-NCs without cells, suspension was diluted with Milli-Q water and a small droplet was placed on a copper grid and allowed to dry prior to imaging.

The LASAF was used for image acquisition of CARS/TPEF and BF images and adjusting the contrast for these images. The spectral data was processed with OriginPro 8.6 (OriginLab, Northampton, Massachusetts, USA). Contrast for TEM images was adjusted with Fiji Image J (open-source distribution) and Microscopy Image Browser (MIB, version 2.01 with MATLAB R2017b, MathWork, MA, USA)[214] and overlaying of CARS/TPEF and TEM images was achieved by using GNU Image Manipulation Program v2 (open-source distribution). For the overlaying CARS/TPEF and TEM images, CARS/TPEF images of size 768 × 768 pixels, obtained with a digital magnification of 4.5× (pixel size 135 nm) were used as a template so that low magnification (500×) TEM images were compared. These magnifications resulted in images that could be overlaid (low magnification of TEM and relatively high magnification of CARS). Furthermore, smaller regions (250 pixels × 250 pixels) from the images were cropped and the CARS/TPEF image was placed as the bottom layer for which opacity was adjusted.

Distinguishable regions of the cells (e.g. edges of the cell) were used as benchmark for overlaying and TEM images required some stretching, since sample preparation causes some shrinkage to the cells. To be able to analyze all the TEM sections showing cells with internalized NCs, TEM slices were aligned using Amira (version 6.3, Thermo Fisher Scientific, FEI, Oregon, USA). The frame numbers were added to the aligned images using the GNU Image Manipulation Program v2 and the aligned sections were rendered as a video or minimum projection image of overlaid TEM sections in MIB.

*4.2.10.8 Solid-state imaging with PCA based hyperspectral CARS and SFG (**IV**)*

CARS and second order non-linear spectra on the surface of the tablets containing (1:1:1 w/w) gamma, alpha and amorphous indomethacin were recorded as described in Section 4.2.10.2, Non-linear spectroscopy (**I-IV**). MATLAB R2016a (MathWork, MA, USA) was used to process the hyperspectral CARS data. Images (33 images with different wavenumbers, each with 512 × 512 pixels) obtained from each CARS spectral scan were converted into ascii- files so that each pixel had a value corresponding to the intensity of the pixel. The data was treated with standard normal variate (SNV) transformation. These matrices were then overlaid to achieve a 3D data stack (x,y,ω) and the data was mean centered. Thus, each pixel represented a single CARS spectrum resulting in a total of 262 144 spectra. Principal component analysis (PCA) was then performed on the data matrices. The first three principal components (PCs) were used to create RGB color images based on PC score values at each pixel. The PC score values were normalized so that the minimum PC score value was set to 0 and the maximum score value to 1 and all values in between scaled linearly. PC1, PC2 and PC3 scores were represented by red, green and blue coloring, respectively. The relative intensity of these colors at each pixel depended on the PC score values and can vary case by case. It was also possible to extract the original spectrum from each pixel. The SFG peak signal intensities from 480 nm to 490 nm were extracted from the second order non-linear spectra and subsequently overlaid with the PCA-based CARS images.

*4.2.10.9 Multimodal non-linear imaging of surface crystallization (**IV**)*

To visualize surface crystallization of indomethacin tablets, the CARS signal at a specific CARS shift unique for one of the solid-state forms (identified from the CARS spectra) and the SFG/SHG signals (with the bandpass filter 465 nm ± 85 nm) were simultaneously detected using two separate channels (epi-direction). Gamma indomethacin was imaged at 1701 cm^{-1} and amorphous indomethacin at 1676 cm^{-1} while SFG/SHG signals were used to visualize alpha indomethacin. Images obtained from these two channels were then overlaid. To remove any TPEF signal interference from the CARS signal, the signal detected when the sample was excited with one laser only (pump beam) was subtracted from the overall signal detected when the excitation was carried out with both the Stokes and pump/probe beams.

5 Results and discussion

5.1 CARS imaging of live Caco-2 cell cultures (I)

Fluorescence microscopy and Raman microscopy of cells has usually been performed with the cells cultured on glass surfaces, e.g. Petri dishes, cover slips, or well plates. However, in pharmaceutics, Caco-2 cells are regularly cultured on membrane inserts, where they are expected to grow as a monolayer, which mimics the intestinal epithelium. The cells in this monolayer express morphology with many features in common with the intestinal epithelium, including tight junctions, carrier proteins and microvilli.[215,216] These Caco-2 cell monolayers are then used in drug transport studies to predict how new drug molecules are absorbed from the intestine. These studies are performed so that the drug is introduced to one side of the insert and the drug concentration on the other side is measured over time.[215,217] These kinds of studies are generally quite easy to perform. However, they do not give any direct information on the cell layer composition and structure during the growth period. Also, the results of such studies can vary between laboratories.[216,218]

Microscopy methods could potentially be used to visualize these Caco-2 cell monolayers and this would help facilitate understanding of structural sources of drug permeation testing variability. CARS microscopy, theoretically would offer a potential platform for this purpose, since it offers a chemically-specific, label-free, inherently confocal signal and is relatively non-destructive.[100] Therefore, the aim of the first study in this Thesis was to evaluate if label-free and chemically-specific CARS microscopy could be used to image live Caco-2 cells cultured on these membrane inserts. This requires the screening of suitable imaging conditions, including insert materials, media solutions for imaging and tolerable laser powers for live cell imaging. After optimizing the imaging conditions, CARS imaging was used to image the lipid composition and distribution of Caco-2 cell monolayers and changes during the typical culturing period.

5.1.1 Screening of suitable imaging conditions and materials

The CH_2 stretching region at around 2800-3000 cm^{-1} is especially of interest in coherent Raman imaging of cells, since cells contain CH_2 moieties in large quantities and stretching vibrations of this group can be probed with coherent Raman microscopy. Therefore, this region was examined in more detail, when suitable imaging media solutions, insert materials and cell viability were evaluated.

Four media solutions for intestinal epithelial cell culturing were tested in this study: two buffer solutions commonly used for cell experiments, PBS and HBSS-HEPES, and the cell culturing medium DMEM, with and without phenol red. CARS spectra of these media were measured to find out the differences in the background that could potentially disturb the imaging of cells. Based on the spectral profiles, it was concluded that the CARS signal strength was weak and no major differences in the CARS spectra could be seen between the media solutions. The spectra showed similar profiles with a broad peak at around 3200 cm^{-1} associated with the stretching of the –OH group of water; no other peaks were observed. Thus, all the media are suitable for imaging cell cultures in this spectral region. In this study, HBSS-HEPES was subsequently used while cells were imaged on membrane inserts.

For the potential insert materials, polycarbonate (PC), polyethylene terephthalate (PET) and collagen coated polytetrafluoroethylene (PTFE) were chosen and the durability of different insert materials to the CARS lasers was evaluated by recording z-stacks (2800 cm^{-1}) of the membranes. It was found that the most common insert material, PC, was not suitable for CARS imaging. Figure 14a includes a BF image after recording a z-stack across the entire thickness of a PC membrane (~22 µm) with laser powers of 32 mW and 14 mW for the pump and Stokes beams, respectively. Obvious damage, manifested as holes and surrounding dark regions, is visible. Such damage occurred when laser powers as low as 15 mW for the pump and 7 mW for the Stokes beam were focused on the filters. The ongoing damage was also seen as a broadband luminescence emission on all PMT detector channels. The damaged areas are expected to contain carbon (graphite) particles. These particles absorb light through one-photon and two-photon excitation which causes fluorescence over a broad spectral range. Part of this emission falls into the detection range of the CARS channel and is seen as an intense signal (Figure 14b). Strong absorption could possibly trigger further thermal damage on the membrane. Similarly, CARS lasers also damaged PET inserts and even a single scan (1024 × 1024) with laser powers of 47 mW for the pump and 20 mW for the Stokes were able to damage the insert. In contrast, the PTFE inserts showed superior durability compared to the PC and PET inserts. It was possible to record CARS z-stacks with maximum laser powers with no apparent optical damage.

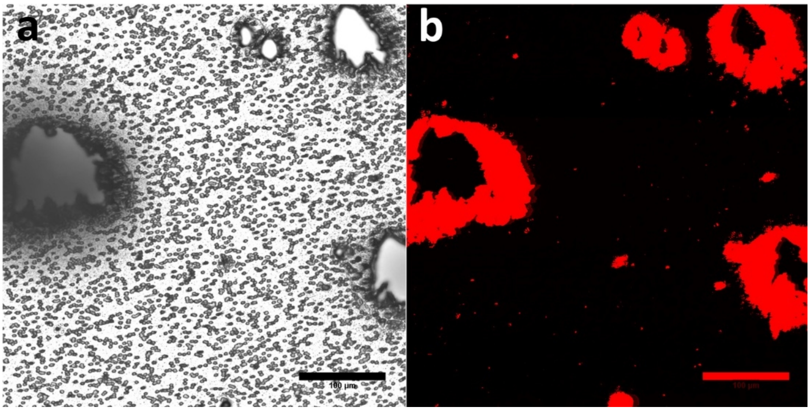

Figure 14. Optical damage on a PC membrane as seen in the BF (a) and CARS (b) channels after CARS z-stack imaging (2800 cm^{-1}) through the thickness of the insert membrane. The CARS laser powers were 32 mW for the pump and 14 mW for the Stokes beam. Scale bar is 100 µm. Reprinted from publication (**I**) with permission. Copyright (2017) Elsevier.

As mentioned, in general the CARS process is thought to be rather well tolerated for cell and tissue imaging[100,117] and CARS microscopy can be applied for long-term live cell imaging.[186] The CARS process itself occurs from the ground electronic state,[100] which reduces photodamage and many CARS microscopes use picosecond pulsed lasers that have a lower peak power compared to femtosecond lasers that are typically used in TPEF imaging.[166] However, multi-photon absorption-induced photodamage can still occur when the Stokes and pump lasers are irradiated onto the sample during CARS imaging. Thus, it is important to confirm the viability of the cells in order to be able to image cells that remain alive and healthy under the experimental time needed. Since there are different CARS setups between research groups it is not trivial to compare the photodamage that is observed in various studies unless all variables are accounted for. These variables include laser wavelength(s), pulse width, and repetition rate, objectives used and image acquisition time, including pixel dwell time and scanning speed. Also some studies between laboratories can be slightly conflicting. For example Wong et al. showed that there is apparent photodamage (NIH/3T3 cells) with a laser power of 35 mW,[118] whereas Cheng et al. concluded that the same cells could be imaged with up to 60 mW average powers.[166]

In our study, the Caco-2 cell viability after CARS imaging with increasing powers was evaluated using BF imaging and fluorescent stains to selectively stain live and dead cells, with Calcein AM used to stain the live cells and EthD-1 used to stain the dead cells. No major changes in cell morphology were observed in the BF images. After exposing the cell culture for 5 min with powers of 100 mW for the pump and 50 mW for the Stokes beam (total irradiance of ~0.14 TW/cm^2) it was possible to see some changes in cell culture structure: the cells were less tightly associated with one another indicating photodamage. This result is in accordance with previous studies where comparable irradiance values were used and is attributed to chemical changes due to formation of free electrons in the sample.[219,220] Since morphological analysis is not always sufficiently sensitive to detect cell viability, fluorescence staining was also used. After the full z-stack (~2 min exposure time) at laser powers of 100 mW and 50 mW for the pump and Stokes beams respectively, the cell membranes were not sufficiently damaged for EthD-1 to contact the DNA-like structures and fluoresce. Thus, according to this analysis, the Caco-2 cells were still viable soon after CARS image acquisition even with the high laser powers.

It is likely that different cells can tolerate laser exposure differently. Wong et al. showed that there was apparent photodamage in the BF image of NIH/3T3 fibroblast cells after CARS z-stack imaging with laser powers of ~35 mW.[118] The same cell was also imaged after 2 h and it had altered its morphology to become round-shaped and was detached from the surface of the Petri dish, indicating cell death. In our case, no such effects were observed when Caco-2 cells were imaged using z-stacks and pump and Stokes laser powers of 40 mW and 20 mW, respectively. The BF images were recorded before and 2 h after the CARS imaging. After 2 h, the cells were still attached to the bottom of the 24-well plate and no change in morphology was observed. One potential reason for the different observations could be that Caco-2 cells tend to grow closely attached to each other, unlike NIH/3T3 cells.

It should be also taken into account that different types of experiments require different thresholds for cell damage. For example, lipid droplet trafficking or other internal cellular processes could be disrupted with lower laser powers and energies. Thus, it is best to keep the laser powers as low as possible, while still being able to capture images of sufficient quality. As an example, Nan et al. imaged lipid droplet transport in living steroidogenic mouse adrenal cortical (Y-1) cells using CARS microscopy, and concluded that laser pulse energies should be under 2 nJ with an average power under 9 mW to be able to image lipid droplet transport nondestructively.[161]

In conclusion, we demonstrated that using a pixel dwell time of 1.2 ms, frame rate of 2.59 s per frame, 45 scans per z-stack, pulse repetition rate of 80 MHz, pulse width of 5–7 ps and 1064.5 nm and 816 nm laser wavelengths, no damage to the cells was apparent even with a total average power as high as 150 mW. Typically, total average powers of 18–32 mW for pump/probe beam and 8–14 mW for the Stokes beam in the focus were needed to produce good quality images of lipid structures in Caco-2 cells. These settings were subsequently used for imaging Caco-2 cells grown on PTFE inserts with HBSS-HEPES pH 7.4 as imaging buffer.

5.1.2 Label-free CARS imaging of live Caco-2 cell cultures on membrane inserts

The membrane inserts with the Caco-2 cell monolayer on top were placed on a glass microscope slide and imaged while maintaining suitable conditions for live cell imaging: 37 °C and 5% CO_2 level (Figure 15a). CARS spectra were measured and a strong peak at 2856 cm^{-1} was observed and identified as CH_2 stretching (Figure 15b). In addition, a shoulder occurred above 2900 cm^{-1} (CH_3 stretching).[182] The CH_2 stretching region is typically used for imaging cellular lipid structures, especially lipid droplets, since the CH_2 moiety is highly concentrated in cellular lipids.[99,100,122,167] No strong CARS peaks were observed in the spectra that were recorded in the centre of the cell. Above 3000 cm^{-1} there was a broad peak in both spectra due to the aqueous environment.

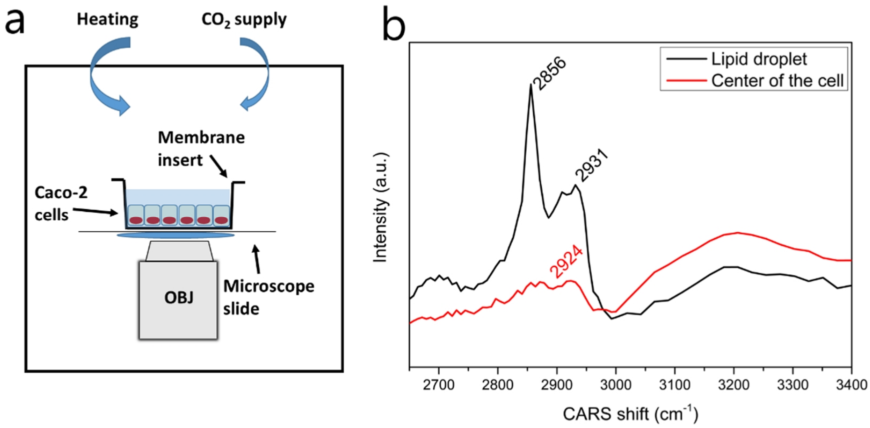

Figure 15. a) Schematic figure of the imaging configuration of live Caco-2 cells cultured on PTFE membrane inserts. b) CARS spectra of a lipid droplet and center of a cell for live Caco-2 cells cultured on PTFE membrane inserts. Adapted from publication (**I**) with permission. Copyright (2017) Elsevier.

The interest in studying lipid droplets, their maturation, trafficking and cellular function is growing. It is known that in general, lipid droplet sizes can vary substantially depending on the cell type and, for example, adipocytes can have a single lipid droplet tens or hundreds of microns in size.[221] A phospholipid monolayer forms on the outer surface of the lipid droplets, and the core consists mainly of neutral triacylglycerol and cholesterol esters.[222] It is not completely understood how intracellular lipid droplets are formed, although they are believed to originate from the endoplasmic reticulum (ER). Neutral lipids are synthesized inside the bilayer of the ER from where lipid droplets with the phospholipid monolayer surface bud after maturation.[223,224] Lipid droplets are nowadays believed to be dynamic organelles that also contain and interact with many proteins.[223,225] Intralipid droplet proteins of particular importance are the perilipin family proteins, which regulate the balance between the degree of lipid storage and hydrolysis of stored triacylglycerols.[226]

Previously it was shown that human colon cancer tissue has an increased number of lipid droplets compared to healthy tissue.[227] Since Caco-2 cells are colon adenocarcinoma cells, these cells may contain larger quantities of lipid droplets than would be expected in healthy tissue *in vivo*. Accioly et al. used electron microscopy to show that Caco-2 cells have a 4 to 5-fold increase in the number of lipid droplets compared to rat intestinal epithelial cells (IEC-6 cells) after 24 h of culturing. Scalfi-Happ et al. used confocal spontaneous Raman microscopy for imaging Caco-2 cells and IEC-6 cells and concluded that Caco-2 cells had substantially higher lipid droplet accumulation compared to non-malignant IEC-6 cells.[228] Our results support this and lipid droplets were observed in Caco-2 cells in large quantities using CARS microscopy (Figure 16). However, to the best of our knowledge, the present study is the first where live unlabeled Caco-2 cells have been imaged in a (bio)pharmaceutically relevant environment for drug permeation studies, including on membrane inserts. It is more demanding to capture high quality images in these conditions compared to situations where cells have been grown on glass slides or glass-bottomed well plates, which are typically used for CARS imaging. As demonstrated here, the membrane insert material can have a great impact on the image quality of the cells.

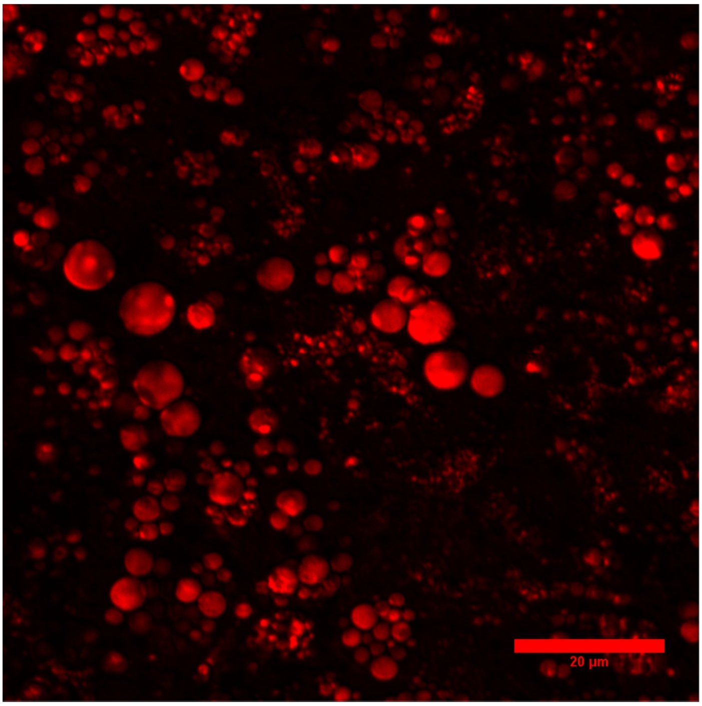

Figure 16. F-CARS image at 2860 cm^{-1} of lipid droplets in live Caco-2 cells grown on a PTFE membrane insert (Transwell® insert with a pore size of 3 µm) after 14 days of culturing. Adapted from publication (**I**) with permission. Copyright (2017) Elsevier.

Furthermore, structural evolution of the lipid-rich structures in Caco-2 cells was evident during the cell culture progression. After 7 days of culturing many small lipid droplets were visible in the CARS images. The size of the lipid droplets increased substantially over the 21-day period. After 14 days of culturing, the diameter of the largest lipid droplets was ~7 µm (Figure 16). The diameter of a Caco-2 cell is ~20 µm, meaning that in these cases over 10% of the cellular cross section was filled with a single lipid droplet.

In conclusion, it was shown that label-free, chemically-specific CARS microscopy can be used to image live Caco-2 cells on membrane inserts (PTFE) and especially to probe lipid structures, most prominently lipid droplets, and to visualize the structural changes over the culturing period. CARS microscopy was successfully used to show that the number and size of the lipid droplets increased substantially over a 21-day culturing period, which is important in the context of drug permeation studies. Caco-2 cell lipid droplet content is pharmaceutically relevant, since, as mentioned, Caco-2 cells are frequently used as an *in vitro* intestinal cell model in studies predicting drug transport across the intestinal epithelium. However, with many drugs being hydrophobic and/or lipophilic, the lipid content of the cells will influence drug permeation. Therefore, knowledge of lipid content and distribution in exactly the same cell cultures that are used for drug permeation studies may help address the reasons for the wide variability in drug permeation observed between laboratories with these cultures. CARS microscopy allows for such analysis.

5.2 Chemically-specific imaging of nanocrystal cellular uptake (II-III)

As mentioned in the literature review, the pharmaceutical industry requires novel and innovative screening methods, especially in preclinical studies, when new drug molecules or drug formulations are tested with cells.[229,230] These cell studies can reveal crucial information about the efficacy and safety of the new drug candidates and this information can be used to screen the potential candidates for further studies. For the industry, it would be greatly beneficial if such cell studies could be performed as early as possible in the drug development phase and give as accurate information as possible. The key point here is to have an efficient preclinical model, and imaging techniques play an important role here.[231] The imaging of cells at the single-cell level in a native environment however still remains challenging. Nevertheless, it has been shown in numerous publications that coherent Raman imaging is a microscopy method with plenty of potential to image live cells and living organisms.[117,203,232] Also, this technique is gaining interest as an imaging tool for detecting drug delivery and accumulation in cells. These kinds of studies are a 'hot topic' at present and technical developments have already made it possible even to detect micromolar concentrations of drugs in cells.[142] In addition, a current trend is to use nanoparticles in drug development, for example to achieve targeted drug delivery for cancer treatment. Suitable imaging techniques are required to follow the cellular uptake and intracellular fate of nanoparticles. Coherent Raman imaging also has much potential for visualizing the nanoparticle-cell interactions and uptake of nanoparticles into cells.[55,119] However, there is still a limited number of such publications and, especially, nanocrystal cellular uptake studies are lacking.

In this Thesis, drug nanocrystals were used as model nanoparticles and the capability of CARS imaging with TPEF and SHG imaging for probing nanocrystals in cells and tissue were evaluated (**II-III**). It is worthwhile to mention that nanocrystal suspensions are realistic drug formulations that can be used as such and indeed the first study involved a marketed nanosuspension product, Xeplion®, which contains the prodrug PP. In the first study, these nanocrystals were used, because, in addition to being a suitable simple model nanoparticulate system, it had been shown that PP-NCs started to accumulate *in vivo* in cells of the mononuclear phagocyte system.[8] Xeplion® is a long-acting injectable drug formulation and therefore nano-crystal–macrophage interactions and nanocrystal accumulation in cells are especially important events as they can influence the pharmacokinetics of paliperidone palmitate. To be able to study the accumulation of nanocrystals in macrophages, suitable imaging techniques are needed. Therefore, the potential of multimodal non-linear optical imaging, including CARS microscopy, as an analytical tool for the fast and sensitive label-free exploration of organic drug nanocrystals in various biological matrices was evaluated (**II**). Fixed and living RAW264.7 macrophages (a commonly used cell line for uptake studies), as well as *in situ* in unstained histological sections of i.m. administration sites, were used.

In the second study of cellular nanocrystal uptake, GLI-NCs were the model nanoparticles (**III)**. The main focus in this study was the analytical method development. The aim was to combine two imaging methods, chemically-specific label-free CARS microscopy and (sub)nanometer scale spatial resolution transmission electron microscopy (TEM), to image the cellular uptake of nanoparticles. Using this synergistic correlative coherent anti-Stokes Raman scattering and electron microscopy (C-CARS-EM) method it would be possible to gain insights into nanoparticle uptake that would not be available with either of these techniques alone. The cellular uptake of GLI-NCs in RAW 264.7 macrophages was visualized first with CARS, and then exactly the same cells were visualized with TEM, to be able to obtain more information about the subcellular localization of the nanocrystals.

5.2.1 *Narrowband CARS imaging of nanocrystal cellular uptake (**II**)*

Raman and CARS spectra of the pure drug substances (PAL and PP), nanocrystal stabilizer (TW20) and air-dried nanocrystalline suspensions (PP-NC) were recorded to identify the suitable Raman bands for imaging (Figure 17). The entire Raman spectra are presented in Figure 17a and spectra of PAL, PP and PP-NC in the CH stretching region only, most suitable for narrowband CARS microscopy in this study, are shown in Figure 17b. Pure PP exhibited relatively broad, but strong and characteristic, bands in the CH stretching region between 2800 and 3100 cm^{-1} (Fig. 17b) with the most prominent resonances found at approximately 2845 cm^{-1} (symmetric CH_2 stretching) and 2880 cm^{-1} (asymmetric CH_2 and symmetric CH_3 stretching).[233,234] A broad shoulder, which is associated with asymmetric CH_2 stretching and motions of terminal CH_3 groups in saturated acyl chains, was present at around 2930 cm^{-1} and a smaller but distinct Raman peak attributed to aromatic CH stretching occurred at around 3080 cm^{-1}.[235]

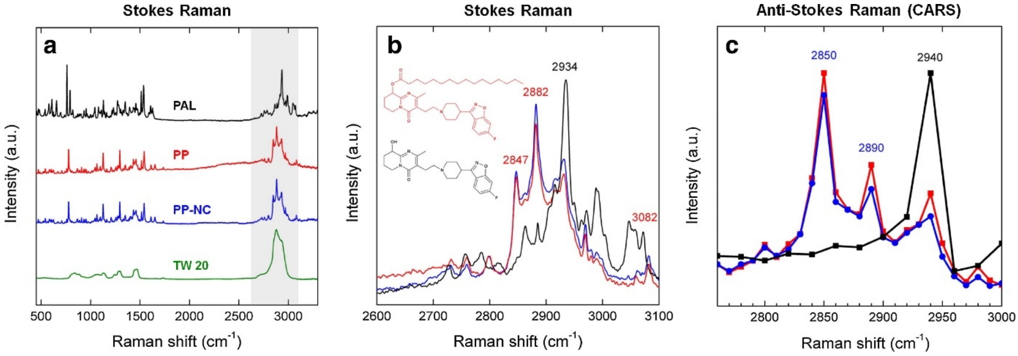

Figure 17. Raman and CARS spectra of the test substances. a) Raman spectra of powdered PAL (black), PP (red), PP-NC (blue) and TW20 (green) showing characteristic peaks in the fingerprint (500–2000 cm^{-1}) and CH stretching (2600–3000 cm^{-1}) region. b) Detail of the highlighted 2600–3100 cm^{-1} region of the Raman spectra of PAL (black), PP (red) and PP-NC (blue) showing strong drug-specific Raman shifts eligible for CARS. (c) CARS spectra of PAL (black), PP (red) and PP-NC (blue) showing suitable drug-specific CARS resonances in the CH stretching region. Reprinted from publication (**II**) with permission. Copyright (2015) Elsevier.

CARS spectra essentially showed peaks at the same positions, while the relative intensities of the peaks varied from those obtained with spontaneous Raman scattering (Figured 17c). For PP, the strongest scattering was detected at 2850 cm^{-1}, followed by two less intense bands around 2890 cm^{-1} and 2940 cm^{-1}. The spectra of powdered PP and air-dried PP-NC were similar despite the presence of small amounts of TW20 adsorbed onto the nanocrystals (Figure 17c). The Raman and CARS spectra of pure TW20 showed a broader band in the 2800–3000 cm^{-1} region associated with CH_2 stretching. It could be concluded that the main contribution to both the Raman and CARS signals originated from the hexadecanoyl (palmitate, C16:0) group. Furthermore, the active moiety PAL, which lacks the alkyl chain found in the prodrug, produced spectra (strong peak at 2940 cm^{-1}) that were different to those from PP, enabling discrimination between the two related compounds using CARS imaging. These findings confirmed that CH vibrational motions (2800–3000 cm^{-1}) are well suited for the imaging of PP nanocrystals through CARS. The 2845 cm^{-1} vibrational shift was subsequently used to image the PP or PP-NCs in a chemically-specific manner.

The next step was to capture chemically-specific images of materials and, especially, to visualize PP-NCs using CARS microscopy and obtain information about e.g. morphology and particle size in order to be able to distinguish PP-NCs later in a cellular context. A strong signal at 2845 cm^{-1} was observed from PP in the epi-direction, as demonstrated in the maximum projection image of a z-stack (Figure 18a). Figure 18b demonstrates the inherent confocality of CARS microscopy: it is an overlaid image of the BF signal and a single-plane CARS image from the same z-stack as in Figure 18a. The peak at 2940 cm^{-1} could also be used to chemically-specifically image PAL (Figure 18c). Most importantly, PP-NCs, sized well below 1 µm, could be visualized using the CARS shift at 2845 cm^{-1} (Figure 18d). The average PP crystal size, as measured through image analysis, was found to be 934.1 ± 485.1 nm (n = 100), which was in good agreement with the known particle size distribution of the PP-NC formulation as previously measured by laser diffractometry (D_V,10 = 450 nm; D_V,50 = 1073 nm and D_V,90 = 3190 nm).[8] The morphology could also be visualized, with the particles being irregularly shaped with sharp edges. Thus, CARS microscopy was suitable for the three-dimensional imaging of unlabeled non-fluorescent PP nanocrystals.

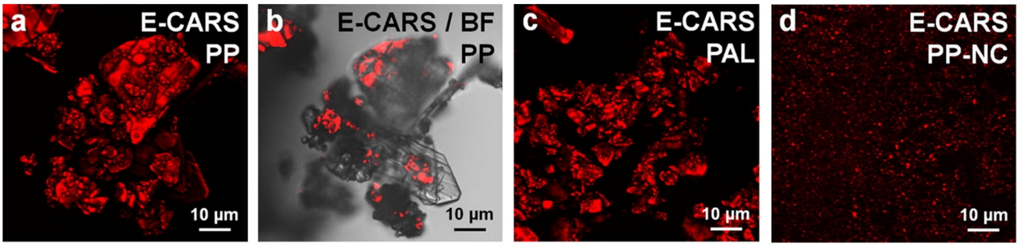

Figure 18. CARS images of unlabeled PAL and non-fluorescent PP powders and PP-NCs. a) Epi-CARS maximum projection image (xy-frames projected in z-direction) of PP powder showing compound-specific CARS-scattering at 2845 cm^{-1} b) Merged BF and single epi-CARS focal plane of the same sample recorded under identical conditions. c) Epi-CARS maximum projection image of powdered PAL (parent compound) showing CARS-scattering at 2940 cm^{-1} allowing discrimination from the prodrug. d) Epi-CARS maximum projection image of the PP- NC nano-/microcrystal suspension recorded at 2845 cm^{-1} showing individual nano-sized crystals. All images are presented without brightness or contrast enhancement. Powers at the sample were ~64 mW for Stokes and ~71 mW for pump/probe. Adapted from publication (**II**) with permission. Copyright (2015) Elsevier.

To ensure that lipids in RAW 264.7 macrophages would not disturb the imaging of PP-NC s in cellular context, control cells without PP-NCs incubation were imaged. A z-stack over the entire height of PFA fixed RAW cells was measured (CARS shift at 2845 cm^{-1}) and it was observed that f-CARS signal generated at 2845 cm^{-1} in each focal volume was only slightly more intense than the weak non-resonant background, as evidenced by the minor cumulative f-CARS signal in the z-projection. Using the digital post-acquisition contrast enhancement, the average cell signal-to-noise ratio could be enhanced so that by using the f-CARS modality it was possible to visualize cell demarcations. High magnification f-CARS images revealed the nuclei of the well-differentiated macrophages as near-circular and low CARS-intensity areas. However, no lipid droplets were obvious in the CARS images obtained. The lipid content in control RAW 264.7 cells after specific lipid droplet staining using Nile Red was also investigated, and the fluorescence was negligible, suggesting the absence of significant numbers of intracellular lipids in these macrophages. In addition, different morphologies (spherical for lipid droplets and irregular for nano/microcrystals) would also facilitate the differentiation between the drug crystals (especially microcrystals) and any lipid droplets.

Cells were subsequently incubated for 2h with PP-NCs and fixed with PFA and imaged using a CARS shift (f-CARS) at 2845 cm^{-1}. Multiple irregularly shaped bodies in each macrophage were observed with a very strong signal at 2845 cm^{-1}, typical of PP. The majority of these bodies were present in the cytosol, outside the respective nuclei at axial positions corresponding to the center of the macrophage (i.e. ~5 µm from the glass bottom). The cytosol and remaining cellular components displayed signal intensities similar to those of the extracellular background, with a lack of notable features. The average diameter of the CARS-positive bodies in the incubated cells, as determined with quantitative image analysis of the corresponding maximum projection image (xy-frames projected in the z-direction), was 1096 ± 866 nm (n = 192), with 57.10 ± 1.48% of the measured particles smaller than 1.0 µm, and all entities larger than 320 nm and smaller than 6.5 µm. The apparent particle size range was in good agreement with the known physical sizes of PP-NC crystals as measured by laser diffractometry, as well as with the average size determined earlier by quantitative epi-CARS image analysis. Also, their sharp-edged geometric shapes, as well as the clear spatial and geometric congruency with the solid crystals observed under BF microscopy, further confirmed that these particles were PP-NCs.

Even though f-CARS could be used to visualize cell boundaries, in order to thoroughly study the cellular uptake of PP-NCs, cell membranes were stained with a fluorescent cell surface marker, allowing simultaneous TPEF and CARS imaging. As a result, merged x-y images or z-stacks provided enhanced cellular contrast and enabled accurate assessment of the PP-NC disposition relative to the cell membrane. After incubation of PP-NCs with cells, staining the cell membranes and fixing the cells with PFA, multimodal CARS/TPEF imaging was performed. RAW 264.7 macrophages were incubated with 250 µg/ml PP-NC for 2 and 24 h. After a 2 h incubation and subsequent removal of excess PP-NCs, some PP-NCs remained associated with the macrophages (Figures 19a-d). BF images (Figures 19a and e) give some preliminary information about nanocrystal cell accumulation, but do not give accurate information on the disposition of the nanocrystals. In contrast, CARS microscopy, in conjunction with TPEF, allowed the visualization, with (sub)micrometer lateral spatial resolution, of non-fluorescent PP-NC nanocrystals relative to the RAW 264.7 cellular framework (Figures 19 b-d and f-h). Compared to 2h samples, after 24 h incubation, markedly more PP-NCs were present in each macrophage (Figures 19e–h), highlighting the high uptake capacity of the RAW 264.7 macrophages and the propensity of TW20-stabilized PP-NC to be recognized and internalized by macrophages. No signs of cellular degradation (i.e. lysis or apoptosis) were observed after 24 h, which was in line with the *in vitro* cytotoxicity data. Due to the inherent confocality of CARS microscopy, orthogonal projection images and three-dimensional reconstructions obtained from z-stacks could be used to obtain information about colocalization of PP-NCs in a cellular context (Figure 19c-d and g-h). Orthogonal projections showed the location of the PP-NCs relative to the cell membrane (Figures 19 c and g). Three-dimensional reconstructions distinguished between adsorbed (Figure 19d, white arrow) and cytoplasmic PP-NCs (Figures 19d and h, black arrow). It could be concluded that several non-spherical particles had been internalized already after 2h of incubation (Figure 19d) and were located within the cytoplasm, in the proximity of the cell membrane, indicating relatively fast PP-NC uptake under the stated conditions. Furthermore, the internalized amount of PP-NCs was markedly higher after 24 h of incubation (Figure 19h).

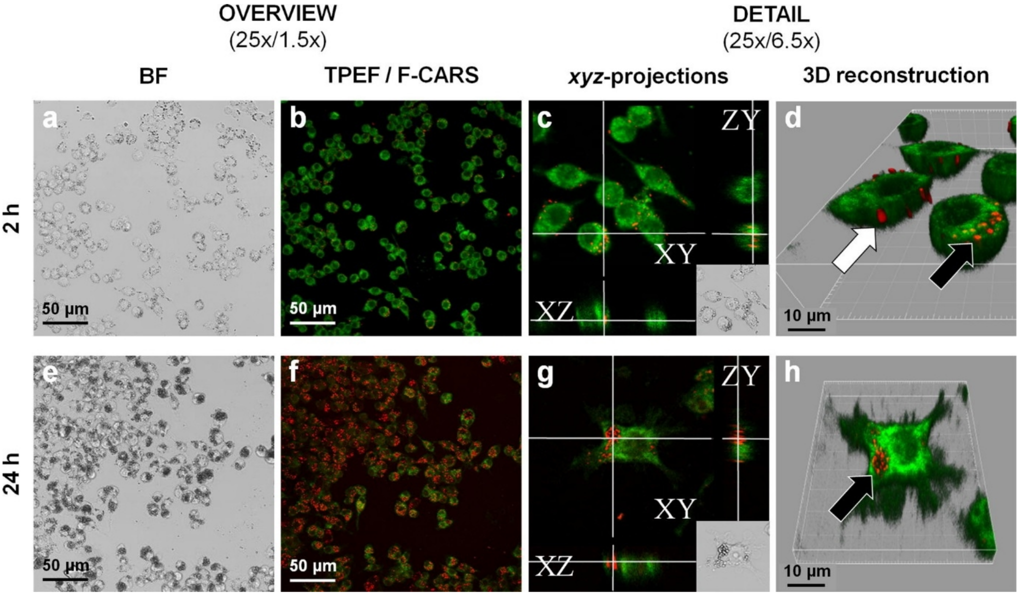

Figure 19. Qualitative investigation of PP-NC interactions with RAW 264.7 macrophages using CARS imaging. Low and high magnification BF (a,e) and F- CARS (red)/TPEF (green) merged micrographs (b, f) of stained/fixed RAW 264.7 macrophages after incubation for 2 h (a–d) and 24 h (e–h) with 250 μg/ml of PP-NCs. (c, g) Orthogonal projections of z-stacked F-CARS/TPEF overlays showing intracellular PP-NCs (d, h) Three-dimensional reconstructions of the z-stacked F-CARS/TPEF overlays. The white and black arrows indicate PP-NCs adsorbed onto the cell surface and phagocytosed, respectively. Reprinted from publication (**II**) with permission. Copyright (2015) Elsevier.

*5.2.2 Live imaging of nanocrystal uptake (**II**)*

Real-time live imaging was additionally performed on cells to explore the suitability of CARS imaging for the selective probing of dynamic processes within unfixed and unstained RAW 264.7 macrophages. F-CARS imaging at 2845 cm^{-1} was used and it offered sufficient CH_2 contrast in living RAW 264.7 macrophages in order to provide information on the cell morphology. Individual cells and their main cellular components could be visualized, but the signal from the cells still did not hinder the signal from PP-NCs. Hence, no additional staining was required. The living RAW 264.7 cells displayed the typical macrophage morphology. Cell-particle interactions started to be visible after approximately 90 min after PP-NC addition, and 2 h after PP-NC addition a limited number of nanocrystals were located intracellularly, near the cell membrane (Figure 20). There was no evidence of photodamage.

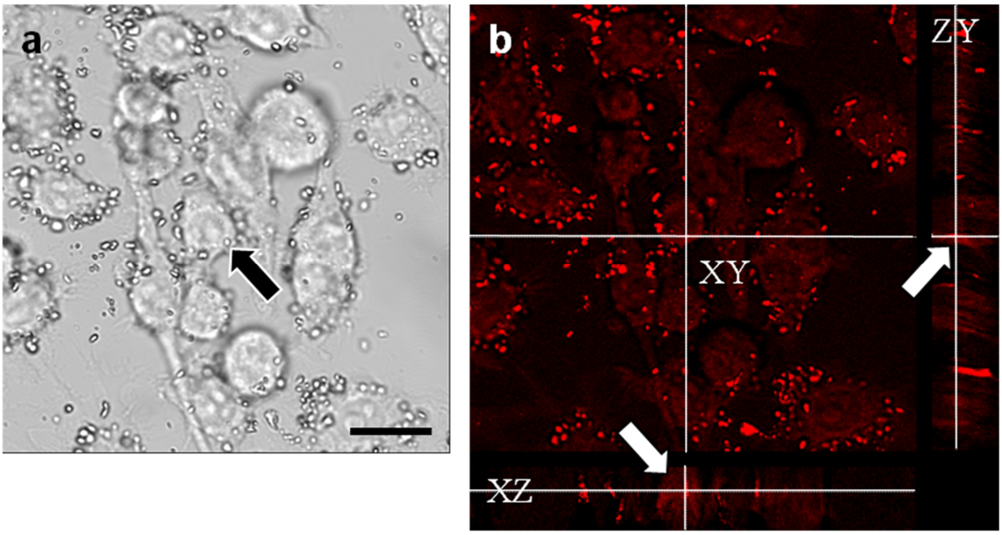

Figure 20. Uptake of PP-NCs in live RAW 264.7 macrophage cells. a) BF image of living RAW 264.7 macrophages after 2 h incubation with PP-NC and removal of the excess particles. b) Corresponding F-CARS *xy*-frame and orthogonal projections showing a limited number of internalized PP-NC. The arrows indicate an example particle that is located intracellularly. The scale bar represents 10 µm. Reprinted from publication (**II**) with permission. Copyright (2015) Elsevier.

Even though it was possible to image the uptake of PP-NCs in live RAW 264.7 macrophage cells, these kinds of experiments possess some challenges in practice. It takes time for particles to get contact with cells. The long incubation at 37 °C resulted in the gradual evaporation of the water from the immersion objective and culture medium. The resulting slight drift in focus had to be manually compensated between each image acquisition. Also for optimal conditions for the uptake to occur, it is important to ensure sufficient particle–cell contact probability, while avoiding a large excess of particles. These are the elements that should be carefully taken into account, when systematic studies of drug particle cellular uptake are performed in real time.

5.2.3 Multimodal imaging of histological tissue sections with nanocrystals

In addition to imaging PP-NCs in cells, the capability of multimodal non-linear imaging was evaluated in the context of PP-NCs in more complex biological matrices. Here, unlabeled paraffin-embedded tissue sections of the rat i.m. PP-NC administration site at day 7 were visualized using CARS and SHG as well as un-labeled un-fixed frozen sections (Figure 21).[8]

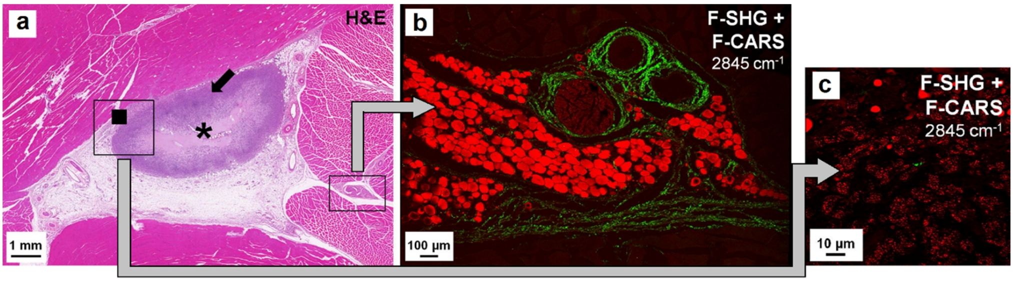

Figure 21. Multimodal imaging of histological sections with PP-NCs. a) BF micrograph of H&E-stained cross section of the PP-NC administration site 7 days after i.m. injection in rats. The depot formed by the PP-NC is indicated with (*). The black arrow indicates the macrophage infiltration (i.e. iatrogenic foreign body granuloma). b) F-CARS (2845 cm^{-1}; red) and F-SHG (green) merged micrographs of a detail of the adjacent unstained tissue section. c) Detail of F-CARS (2845 cm^{-1}; red) and F-SHG (green) merged micrograph of the adjacent unfixed cryosection showing intracellular PP-NCs. Adapted from publication (**II**) and reference[8] with permission. Copyright (2015) Elsevier.

Simultaneous detection of f-CARS signal at 2845 cm^{-1} and f-SHG signal could be used to visualize lipids in adipocytes and non-centrosymmetric structures, mainly collagen in unstained tissue section (Figure 21b). In addition, CARS microscopy could be used to visualize intracellular accumulation in the infiltrating macrophages at the injection site (Figure 21c). The PP-NC nanocrystal distribution was in accordance with that observed under polarized light microscopy.

5.2.4 Correlative CARS and electron microscopy of nanocrystal cellular uptake (III)

It was shown that label-free and chemically-specific CARS microscopy is a useful tool for detecting nanoparticles having dimensions larger than the optical lateral resolution of approximately 400 nm, in relation to the cellular framework in cell cultures as well as *ex vivo* in histological sections (**II**). However, in order to find out more detailed information about subcellular localization of internalized nanoparticles and the subtle cellular mechanisms of uptake, a combination of analysis techniques is helpful. Fluorescence microscopy can be used to study the uptake mechanisms of nanoparticles by using fluorescence stains to stain cellular organelles responsible for particle uptake. However, the data interpretation in such studies is based on colocalization of fluorescence signals of nanoparticles and cellular organelles, such as lysosomes or macropynosomes.[50,142] Despite the fact that superresolution microscopy holds potential in these kinds of studies and can be used to obtain more accurate information about colocalization than conventional diffraction-limited microscopy, electron microscopy still remains the only imaging technique that can be used to visualize whole cells in great detail, including different organelles and associated membranes. Therefore, EM can be used to study the intracellular fate of nanoparticles in great detail, but without chemically-specificity. As demonstrated in the earlier study, CARS offers chemically-specific imaging, but is still limited to diffraction-limited resolution (**II**). Therefore, the aim of the third study of this Thesis was to develop a correlative imaging platform by combining CARS microscopy and EM (**III**). This correlative coherent anti-Stokes Raman scattering and electron microscopy (C-CARS-EM) platform was used to study the cellular uptake of GLI-NCs in more detail by synergistically combining the inherent benefits of these two techniques.

GLI-NCs were prepared by wet media milling and stabilization by HPMC. First, GLI-NCs were characterized by dynamic light scattering (ZetaSizer Nano–ZS, Malvern Ltd., UK), EM and XRPD. By using these techniques it was confirmed that particle size reduction to the nanoscale upon milling was successful. Dynamic light scattering showed that the average particle size was 252 nm. Electron microscopy images revealed that coarse unmilled prismatic crystals had a particle size as big as 100 µm (Figure 22a), while the particle size was in the nano-range after milling (Figures 22B and C). X-ray diffraction confirmed the crystalline nature of the material after milling.

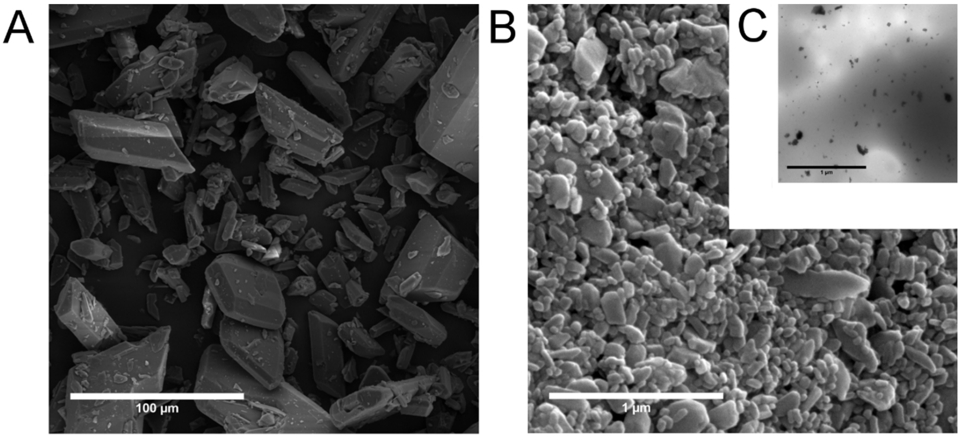

Figure 22. Electron microscopy images of GLI crystals. a) SEM image of unmilled crystals. b) SEM images of GLI-NCs. c). TEM image of GLI-NCs. Scale bars are a) 100 µm, b) 1 µm and c) 1 µm.

Raman and CARS spectra of coarse GLI crystals and GLI-NCs revealed peaks due to the CH_2 and CH_3 stretching at approximately 2850 cm^{-1} and 2900 cm^{-1} (symmetric CH_2 stretching),[234,235] and 2960 cm^{-1} (antisymmetric CH_3 stretching)[234] (Figure 23a). The peak at 3075 cm^{-1} is due to CH- stretching in the benzene ring,[236,237] This peak was chosen for chemically-specific imaging of GLI crystals with narrowband CARS microscopy (Figure 23B), since it is distinct from the CH_2 stretching signals of endogenous cellular lipids[238] and the stabilizer, hydroxypropylmethyl cellulose (HPMC) (Figure 23A).

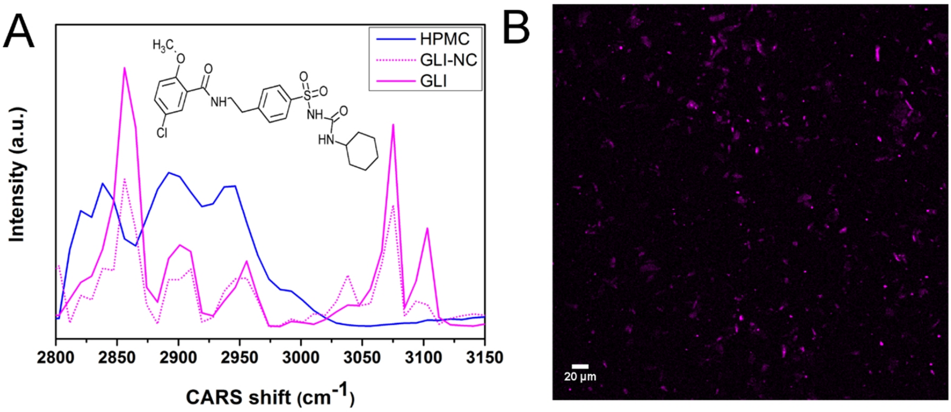

Figure 23. a) CARS spectra of unmilled GLI, GLI-NCs and suspension stabilizer HPMC and chemical structure of GLI. b) Chemically-specific CARS image of GLI-NCs (epi-CARS at 3075 cm^{-1}).

The same (RAW 264.7 macrophage) cells as in the previous study (**II**) were also used to study the cellular uptake of GLI-NCs (**III**). These cells were used because macrophage cells efficiently internalize particles with varied sizes and the cellular uptake of nanocrystals could be probed by using CARS microscopy as demonstrated in the previous study (**II**) therefore providing a suitable model for this proof-of-concept study. Cells were incubated with GLI-NCs in cell culturing medium for 6 h and cell membranes were stained with CellMask® Orange and fixed with 2% glutaraldehyde in 100 mM sodium cacodylate buffer. First, cells were imaged with BF microscopy, which was also used to visualize the grid markings on the Petri dishes so that the same cells could later be located and imaged with TEM. Epi-CARS imaging was subsequently performed to probe the GLI-NCs, while cell membranes were visualized with two-photon fluorescence (TPEF) using a 1064.5 nm laser (Stokes beam). Epi-CARS detection has the benefit that it efficiently rejects solvent signal and therefore allows highly sensitive imaging of small features such as intracellular organelles or drug nanocrystals in this case.[162,239] Therefore, epi-CARS imaging at 3075 cm^{-1} was used to chemically-specifically image GLI-NCs. In addition to CARS imaging, the same cells were imaged with TEM to combine its (sub)nanometer scale spatial resolution with CARS microscopy as depicted in the workflow chart in Figure 23A. Thus, a C-CARS-EM imaging platform, suitable for imaging of drug nanoparticle uptake mechanisms in more detail with both chemical-specificity and (sub)nanometer-scale spatial resolution, was developed (Figure 23B).

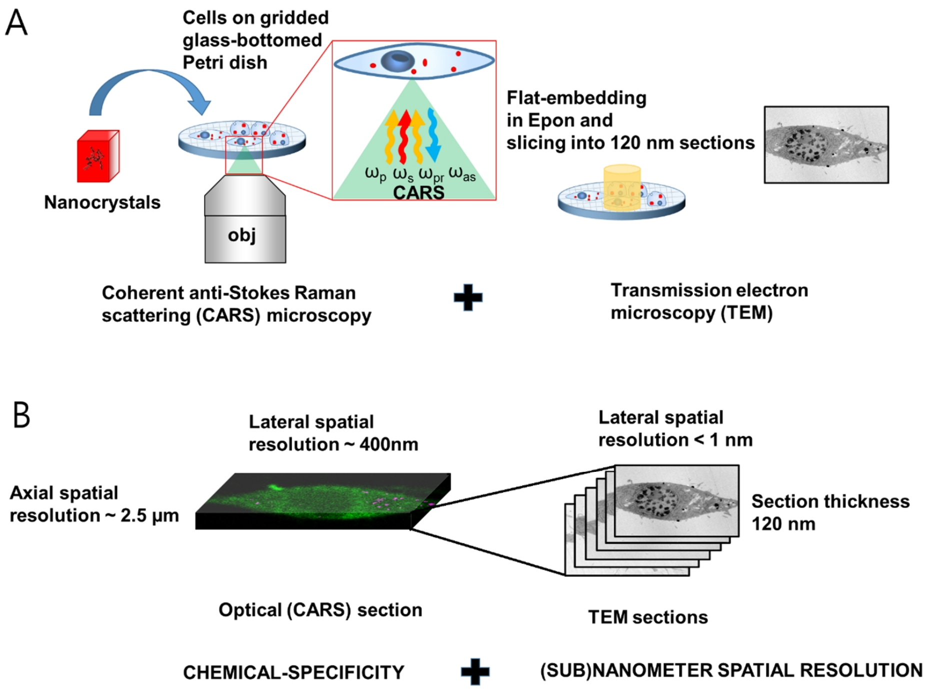

Figure 23. (A) Schematic presentation of the workflow of C-CARS-EM studies of cellular uptake of nanocrystals. Cells were cultured on gridded glass-bottomed Petri dishes allowing the same cells to be located and imaged with TEM after CARS imaging. TEM specimens were prepared while cells were still attached to the Petri dish and EM sections were prepared in the same orientation as CARS and BF imaging (flat-embedding). (B) Schematic illustration demonstrating the resolution of optical CARS imaging and TEM.

BF images revealed that GLI-NCs had accumulated in the vicinity of the cells after incubation (Figure 24A). Confocal TPEF/CARS images could, moreover, be used to confirm that GLI-NCs were inside the cells (Figures 24B and 25A). TEM images from the corresponding three cells revealed that the localization of dark electron-dense crystals in cells was in good correlation with the crystals imaged with CARS (Figures 23 C-E). Interpretation of the EM images of cells with nanoparticles is not always self-evident. Cells can also naturally contain electron-dense endogenous material that can make it difficult to distinguish nanoparticles from these endogenous structures. Here, C-CARS-EM imaging was used to find those cells and specific regions of the cells that had internalized GLI-NCs. Similar particles could not be found from other regions of these cells, nor in surrounding cells with no CARS signal, verifying that the dense particles seen in TEM images are indeed GLI-NCs. CARS spectroscopy could be further used to identify that the detected epi-CARS signal was due to the GLI. CARS spectra were measured from the inside of the cells, allowing spectral extraction from the CARS active regions (Figures 25A-B). Extracted spectra from CARS active regions exhibited similar features to the reference spectrum of GLI, most importantly the peak at 3075 cm^{-1}.

Higher magnification EM images could be further used to gain insights into the subcellular localization of nanocrystals (Figures 25C-E). Typically, this information is not available using Raman-based imaging alone, because of the diffraction-limited resolution. In some cases, if the studied nanostructure is strongly Raman active, Raman signal from particles even smaller than 100 nm could be detected.[55,88,119] Such strong Raman signals can usually be detected by using gold nanostructures as model nanoparticles, since they offer plasmon-induced signal enhancement. However, the smallest details can only be seen with EM, which is the only imaging technique that can truly visualize, for example, two biological membranes touching each other. It is also a method that allows visualization of the whole cell environment in great detail. This is beneficial because it allows, for example, the precise localization of drug nanoparticles to be visualized at a highly subcellular level, and therefore, it can provide access to information about drug uptake mechanism(s). Also, this information can be used to determine cell viability after drug treatment.

In order to develop more efficient and safe new nanomedicines, it is beneficial to get insights into nanoparticle cellular uptake mechanisms at the early pre-clinical stages of drug development. It is evident, that these mechanisms play an especially important role in cases where the biological target of the drug molecule is located intracellularly.[42] This information can be taken into account, when the drug formulation is further developed and tested with animals and finally humans. It is known that nanoparticles can enter into cells in many ways. During endocytosis, the cell actively transports molecules and other material into the cell. Endocytosis can be divided into four main categories; pinocytosis, macropinocytosis, phagocytosis and caveolae- and receptor-mediated endocytosis, but other pathways are also known.[42,240] In endocytosis, the cargo is first engulfed in primary endocytic vesicles. These then fuse to form early endosomes (EEs) and subsequently mature into late endosomes (LEs).[241] LEs subsequently fuse with lysosomes, acidify and form fusions called endolysosomes, where active degradation occurs. Endolysosomes are then finally converted to lysosomes. Larger particles (up to 500 nm) mainly enter cells by phagocytosis,[42,242] during which they are first engulfed by phagosomes, and then become accessible to EEs before undergoing maturation to LEs that fuse together and with lysosomes and phagolysosomes.

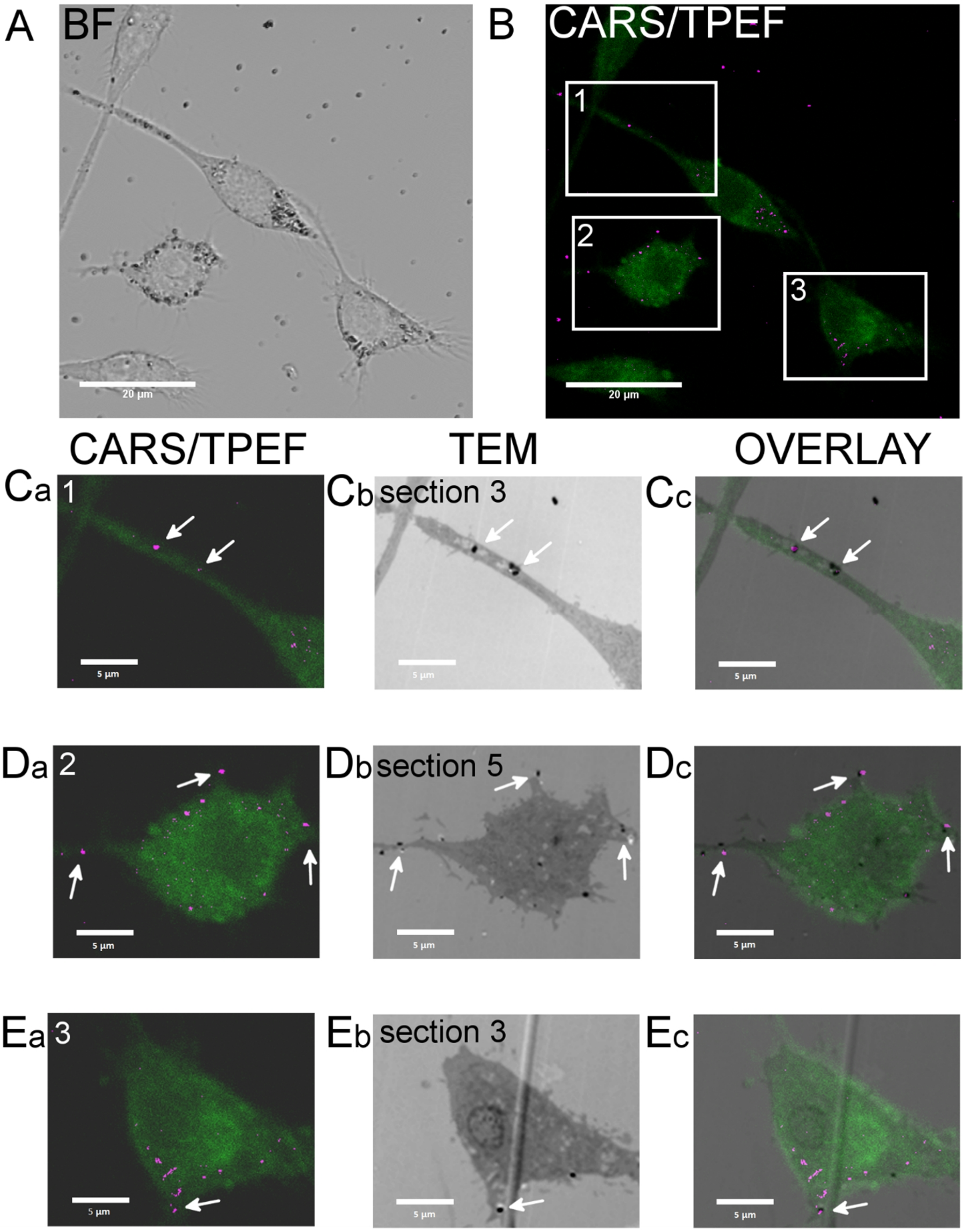

Figure 24. C-CARS-EM images of GLI-NCs in RAW 264.7 macrophages. (A) BF image and (B) corresponding CARS/TPEF image from the inside of the cell. The CARS shift at 3075 cm^{-1} was used to image GLI-NCs. TPEF originates from CellMask Orange® excited with the 1064.5 nm laser. (C-E) Correlative light microscopy (CARS/TPEF) and TEM images and overlays (from left to right) from three spots shown as boxes in image B (1-3). White arrows indicate crystals that were visualized with both techniques. Scale bars are (A-B) 20 µm and (C-E) 5 µm. The position of 120 nm TEM sections is also indicated as section numbers.

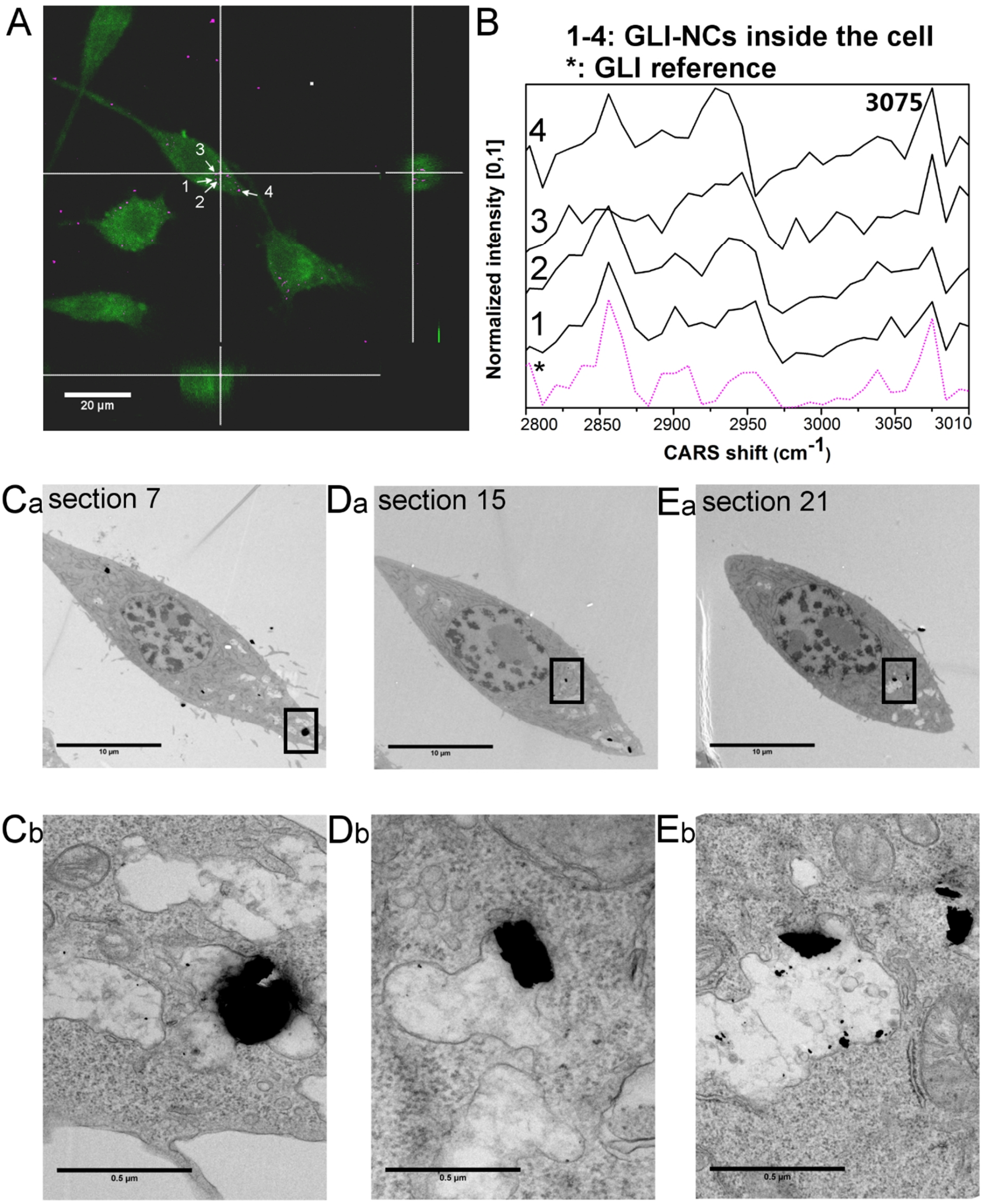

Figure 25. GLI-NC cellular uptake imaged with correlative CARS/TPEF microscopy and TEM. (A) Orthogonal projection image of GLI-NCs inside a RAW 264.7 macrophage. (B) CARS spectra extracted from four regions showing CARS signal at 3075 cm^{-1} from the inside of the cells as indicated by white arrows along with a reference spectrum of GLI-NCs in aqueous medium. (C-E) Correlative TEM images of the same cell imaged with CARS/TPEF. Images C_b–E_b are higher magnification images from the regions shown as black boxes in images C_a–E_a. The position of 120 nm TEM sections is also indicated as section numbers. The total number of 120 nm TEM sections was 44. Scale bars are: (A) 20 µm, (C_a–E_a) 10 µm and (C_b–E_b) 500 nm.

It was observed that after 6h of incubation, most of the internalized GLI-NCs were located in vesicles with multivesicular body (MVB)-like morphology associated with intraluminal vesicles (ILVs) (Figures 25C_b-E_b).[241] Based on these morphological analyses, the vesicles were identified as LEs and fused vesicles (endolysosomes and phagolysosomes). ILVs can be found to some extent in EEs. EEs maturate to LEs after a period of approximately 8-15 mins and many ILVs can be found in LEs.[241] In addition to the larger crystals visible in the CARS images, the TEM images also showed smaller dark electron-dense nano-sized (approximately 10-30 nm) particles, suggesting that the GLI-NCs may have started to dissolve or otherwise break apart in these vesicles. The (sub)nanometer scale spatial resolution of TEM could also be used to gain information about cell viability. After 6 h of incubating the cells with GLI-NCs, the cells started to show some morphological features that suggested cell damage with the fused vesicles starting to look misshapen and diluted. This cell viability information was not accessible with the conventional viability assay.

In conclusion, it was shown that chemically-specific and label-free CARS microscopy is a useful tool to probe nanoparticles in cells and tissues as was demonstrated with real drug formulation, drug nanocrystals, for the first time (**II-III**). Furthermore, correlative use of CARS with TEM could be used to reveal more details about nanoparticle cellular uptake by combining the inherent benefits of the two imaging methods: chemical-specificity of CARS and (sub)nanometer spatial resolution of TEM (**III**). This developed C-CARS-EM imaging method provides a platform to study the interactions between a wide range of nanoparticles and cells in detail. The information obtained from these studies can be used to gain in-depth knowledge about subtle mechanisms by which cells take up nanoparticles. A better understanding of these drug delivery processes can lead to improved and more efficient drug development, as nanoparticle fate in biological matrices can be visualized precisely in early drug development phases with cell models.

5.3 Multimodal non-linear imaging of solid-state forms on surfaces (IV)

As described in the literature review, it is important to have suitable analytical techniques to sensitively detect the solid-state form(s) of an API. Different solid-state forms behave differently, *e.g.* they have different dissolution kinetics. The disordered amorphous form has faster dissolution (for a given surface area). This can be exploited, since a common issue nowadays is that the majority of new drug molecules are poorly water-soluble (and hence can have insufficient dissolution). The challenge of having different solid-state forms of APIs (including the amorphous form) is their different thermodynamic and kinetic stabilities. Different solid-state forms have a tendency to convert to the most thermodynamically-stable form over time, *e.g.* the amorphous form tends to crystallize. Solid-state changes can occur at any stage during and after drug development and pose a challenge to the pharmaceutical industry. Manufacturing processes can trigger solid-state changes; for example, by inducing heat or mechanical stress in the drug product. Moreover, solid-state changes can occur during the storage of drug products. To ensure that drug has the desired solid-state form, suitable analysis techniques are required.

One of the most challenging tasks in solid-state analysis is the detection of subtle, but important transformations (e.g., crystallization) occurring on surfaces. Although the surface makes up a tiny fraction of the total mass of most solid drug particles and dosage forms (e.g., tablets), solid-state specific surface analysis is important due to (i) the different solid-state behavior of surfaces compared to the bulk and (ii) the crucial influence of the surface solid-state form on many critical quality attributes, such as processability, stability and dissolution.

For solid-state analysis, well-established techniques in pharmaceutics XRPD, DSC and Raman and IR spectroscopies have little or no surface sensitivity in the commonly used configurations for solid-state analysis. Against this background, the aim of this study was to investigate the potential of multimodal non-linear optical imaging for spatially resolved and solid-state specific analysis of pharmaceutical surfaces. This multimodality (in a single instrument) is beneficial, since simultaneous usage of two techniques relying on different physical phenomena can either be used as cross-validation and result in more reliable data interpretation or alternatively provide information not accessible with either technique alone. CARS would offer solid-state specific imaging with signal originating from molecular vibrations and SHG/SFG could be used to visualize non-centrosymmetric crystals.

For this study, indomethacin was used as a model drug. First, tablets made of amorphous, gamma and alpha indomethacin (1:1:1 w/w) were prepared and the feasibility of both hyperspectral and narrowband multimodal imaging approaches to image tablet surfaces in order to visualize different solid-state forms spatially and solid-state specifically was investigated. Further, the imaging was utilized to gain new insights into the crystallization behavior of amorphous indomethacin tablets stored at low and high humidities, and the results were compared with those from Raman and FTIR spectroscopies.

5.3.1 Characterization of indomethacin solid-state forms

The morphology of particles of amorphous, gamma and alpha indomethacin powders was first visualized by SEM and BF microscopy. Gamma indomethacin exhibited prismatic morphology with a particle size of approximately 1 µm or less, whereas the alpha crystals were needle-like with crystals up to 100 µm in length. The amorphous particles were prismatic, similar to that of gamma indomethacin, and sized between those of the gamma and alpha crystals.

In order to access the chemically-specific information and to confirm the purity of different solid-state forms of indomethacin, FTIR-ATR, Raman and CARS spectroscopy were performed. Also the SHG/SFG activity of pure powders was evaluated. The FTIR and Raman spectra of the gamma, alpha and amorphous forms of indomethacin are distinct in the carbonyl (C=O) stretching region between 1600 and 1750 cm^{-1} (Figure 26). The indomethacin molecule contains two carbonyl groups; these are contained in the benzoyl and carboxylic acid moieties.[243,244] The peaks are listed in table 4.

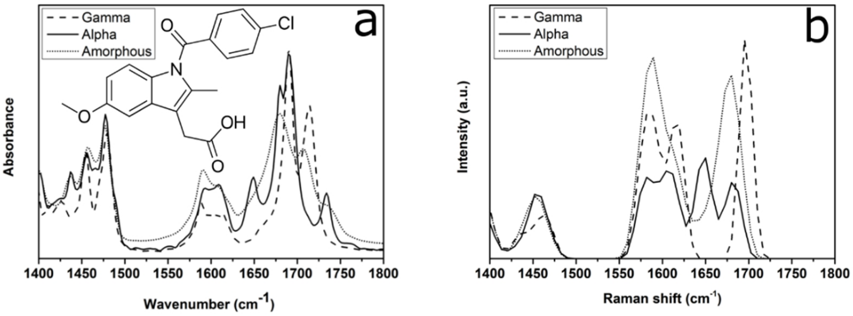

Figure 26. FTIR (a) and Raman (b) spectra of the different solid-state forms of indomethacin. Adapted from publication (**IV**) with permission. Copyright (2017) American Chemical Society.

Table 4. Carbonyl stretching peaks in the FTIR and Raman spectra of gamma, alpha and amorphous indomethacin.

Assignment	Gamma		Alpha		Amorphous	
	FTIR (cm^{-1})	Raman (cm^{-1})	FTIR (cm^{-1})	Raman (cm^{-1})	FTIR (cm^{-1})	Raman (cm^{-1})
Benzoyl stretching	1690	1695	1649, 1679	1654, 1680	1679	1680
Carbonyl acid stretching	1722		1689, 1733	1691	1706	

On the basis of the Raman and CARS spectroscopic analysis (Figure 27a), peaks at 1701 cm^{-1} for gamma indomethacin and 1676 cm^{-1} for amorphous indomethacin were selected for narrowband CARS imaging. All of the three solid-state forms resulted in strong CARS signals. The strongest CARS signal intensity at the highest peak was produced by the gamma form, followed by the amorphous and alpha forms, respectively. In addition, non-centrosymmetric alpha indomethacin crystals produced strong SHG/SFG signals (Figures 27b and e-f). No such signals were observed for the centrosymmetric gamma and amorphous forms. Solid-state specific CARS images of gamma and amorphous indomethacin powders are shown in Figures 27 c-d. No observable TPEF signal was detected when samples were illuminated with only one laser wavelength. Solid-state specific images of alpha indomethacin crystals based on SHG/SFG signals are shown in Figures 27 e-f. Two approaches were used to detect SHG/SFG signals. Figure 26e was a single image acquired by illuminating the sample with 901.3 nm and 1064.5 nm lasers and by detecting the region 465 ± 85 nm as illustrated in Figure 27b with a green bar. Figure 27f was a SFG image obtained from a second order non-linear spectrum that was measured with a 10 nm detection steps (region 400-700 nm). The spectrum is shown in Figure 27b and this 10 nm region used to form Figure 27f is shown as a yellow bar in the Figure 27b. The differences in vibrational spectra and SHG/SFG activity of different solid-state forms suggested that different solid-state forms could potentially be distinguished and this was further studied by analysing the surface of tablets made from mixtures of different solid-state forms.

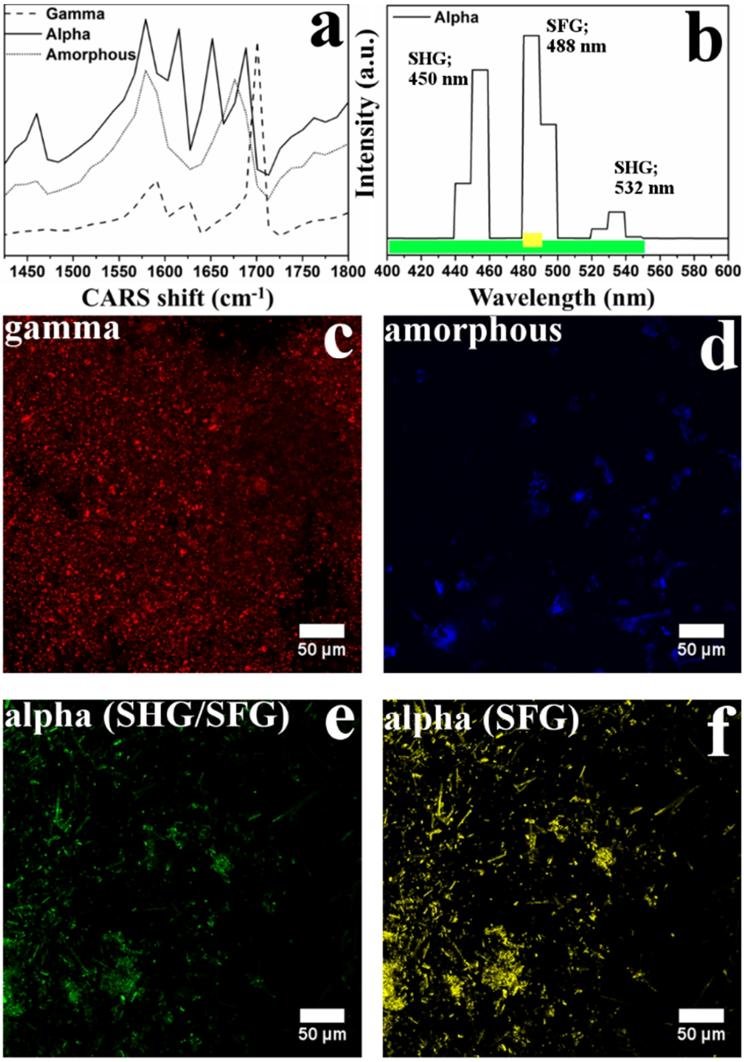

Figure 27. CARS spectra of different polymorphs (a) and second order non-linear emission spectrum of alpha indomethacin (b). CARS images (c, d) of gamma and amorphous indomethacin, an image of alpha indomethacin based on the combination signal of SHG/SFG detected at 465 ± 85 nm (green bar in spectrum b) (e) and SFG image of alpha indomethacin (f) detected between 480 and 490 nm from the spectral scan (yellow bar in spectrum b). Gamma indomethacin (c) was imaged using the CARS shift at 1701 cm^{-1} and amorphous indomethacin (d) at 1676 cm^{-1}. Reprinted from publication (**IV**) with permission. Copyright (2017) American Chemical Society.

5.3.2 Solid-state imaging with PCA based hyperspectral CARS and SFG

Surfaces of indomethacin tablets (1:1:1 w/w, amorphous, alpha, and gamma) were visualized using hyperspectral CARS and SFG imaging (Figure 28.) On a conceptual level, hyperspectral imaging means that the spectrum at each pixel is obtained and this spectral information is then used to form an image. This often requires multivariate data-analysis methods as described in the literature review. In this study, PCA was used to form an image based on the spectra at each pixel. PCA-based CARS images alone and combined with the SFG signal, are shown in Figures 28a and b. CARS spectra generated from differently colored regions are also depicted (Figures 28c–e) along with reference spectra of the pure materials.

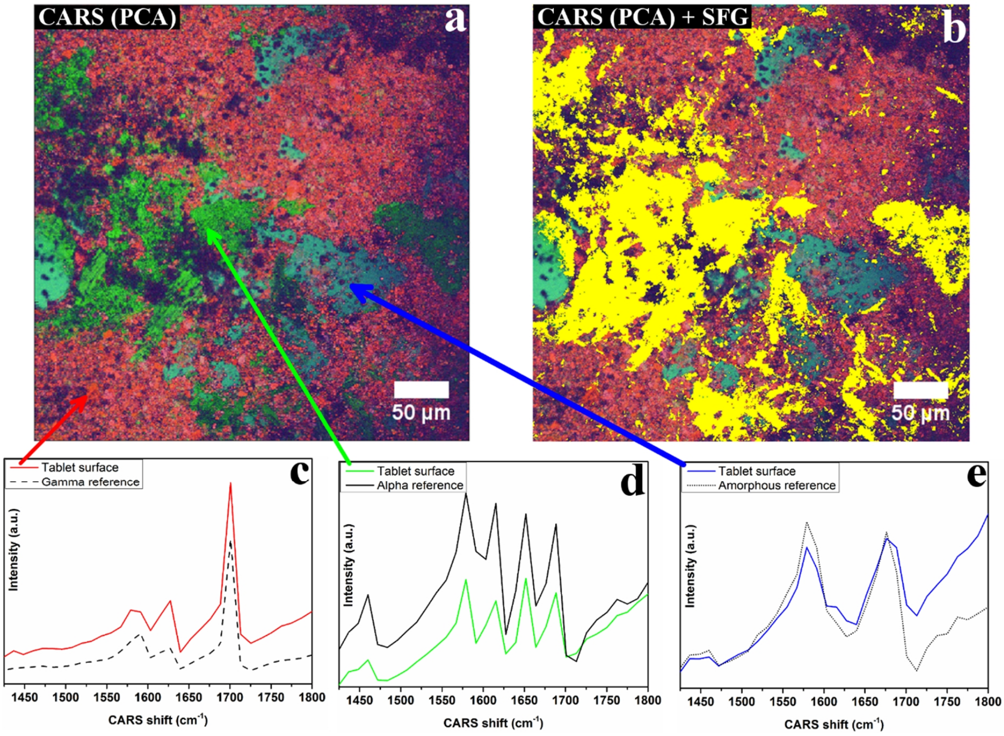

Figure 28. PCA-based CARS image (a) and overlaid RGB (CARS) image and SFG image (b) of the surface of a tablet containing equal ratios of gamma, alpha, and amorphous indomethacin. CARS spectra extracted from the red, green, and blue regions are shown as arrows (c–e). The reference spectra of the different solid-state forms of indomethacin in powdered forms are shown for comparison (c–e). The RGB image is generated from a CARS spectral scan in the region 1413–1800 cm^{-1}, using the score values of the first three PCs. The SFG image is obtained from pixels showing signal detected at 480–490 nm obtained from second order non-linear spectrum (yellow, b). Reprinted from publication (**IV**) with permission. Copyright (2017) American Chemical Society.

The different solid-state forms of indomethacin are clearly resolved (Figure 28) based on CARS microscopy. Red indicates gamma indomethacin, green is associated with alpha indomethacin, while blue-green corresponds to amorphous indomethacin. These assignments were based on the features observed in the PC loadings. Good correlation between SFG and CARS was observed for regions showing alpha crystals. Therefore, the two non-linear microscopy methods, relying on different mechanisms (detection of molecular vibrations (CARS) and SFG signal produced by non-centrosymmetric crystals) were synergistically combined to improve image interpretation confidence.

The applied hyperspectral imaging with multivariate data-analysis has certain benefits over the narrowband (single-shift) imaging. The image is based on data-rich spectral information and therefore holds potential for more complex samples with overlapping (unresolved) spectral features. PCA, as used in this study as processing hyperspectral datasets, has certain benefits as multivariate data-analysis method in image analysis. It is an unsupervised method, requiring no a priori spectral input. Therefore it can be more easily applied to samples for which the chemical composition is not known and the aim is to visualize the distribution of chemical components in the sample*, i.e.* PCA is a data visualization technique. [155–157,245] PCA reduces the dimensionality of the data, while still retaining most of the variations in the data set. Data reduction is achieved by using eigenvectors, principal components, which are aligned to the direction of the most variance in the data. The data, can be then visualized by using only a few principal components (PCs). PCA can be therefore applied to samples of unknown chemical composition, and false-color images, using a few selected PCs, can be constructed. These PC images visualize the distribution of chemical components by coloring the regions of same spectral profile the same color.

PCA has been used previously with CARS microscopy in biomedical applications.[133,134] However, one has to be also aware of the limitations and challenges with regard to PCA being used with CARS data. The challenges of using PCA with CARS data are due to the non-linear nature of the signal in CARS. Usually CARS spectral peaks are broader compared to Raman spectra, and there is always a non-resonant background. Therefore, especially in the cases where substantial mixing of signals could occur in much of the sample, it would be beneficial to use some other (supervised) multivariate data-analysis method or transform CARS spectra to linear Raman-like spectra by extracting the imaginary part.[158] This would, however, typically require a broadband CARS setup and controlling of the phase term.

One potential drawback of using hyperspectral imaging approach is that the data acquisition time becomes longer when a full spectrum is measured. This can be an issue when especially sensitive samples are analysed, since prolonged laser exposures can cause damage to the sample. Also, when considering the potential use of non-linear imaging in industry, sufficient imaging speed is a highly desired feature. In this study, hyperspectral CARS imaging with SFG imaging was also compared to narrowband (single-shift) CARS imaging with simultaneous detection of SHG/SFG signals at 465 ± 85 nm. In this approach, gamma indomethacin was imaged using a CARS shift at 1701 cm^{-1}, amorphous indomethacin at 1676 cm^{-1} and alpha indomethacin was visualized using SHG/SFG. Both methods, hyperspectral method and narrowband imaging, were able to visualize the distribution of amorphous, alpha and gamma indomethacin on tablet surfaces. The narrowband imaging offered rapid analysis with a pixel dwell time in this study of 1.2 µs. Therefore images of pixel sizes 512 × 512 or 1024 × 1024 could be captured in the short time of less than a second.

5.3.3 Multimodal non-linear imaging of surface crystallization

The feasibility of the multimodal non-linear imaging method in detecting solid-state changes during storage was also evaluated. Amorphous indomethacin tablets were prepared and stored at 30 °C/23%RH and 30 °C/75%RH. The tablets surfaces were visualized using CARS and SHG/SFG imaging on days 0, 1, 2, 5, 7 and 22 after preparation. The complementary techniques, SEM, FTIR-ATR and Raman spectroscopy, were also used to support the data interpretation and to compare the sensitivities of the techniques.

The tablets in the present study stored at 30 °C/23%RH changed color from the typical yellow of amorphous indomethacin to white, suggesting surface crystallization. The tablets stored at 30 °C/75%RH did not change their color so drastically, indicating a different crystallization rate or mechanism. SEM also indicated different solid-state behavior. The overall trend at 30 °C/23%RH was that small prismatic particles (typical for the gamma form) appeared and increased on the tablet surfaces. These particles were observed within 2 days of storage, and after 22 days large regions of such crystals were observed. On the tablets stored at 30 °C/75%RH, the visible surface structure changes were slower. However, after 22 days, regions of the tablet surface with needle-like particles exhibiting the typical morphology of alpha crystals were observed.

To obtain spatially resolved and solid-state specific information, CARS and SFG/SHG imaging was performed. Raman microscopy and FTIR-ATR spectroscopy were used for comparison. In general, it was observed that amorphous indomethacin crystallized to the gamma form at lower humidity and to the alpha form at higher humidity, which was generally in accordance with previous studies.[246,247] The crystallization started within the first 1-2 days (Figure 29). However, it was observed that the crystallization was not exclusive to one form. The non-linear SHG/SFG imaging revealed, small SFG/SHG active regions among the inactive amorphous and gamma regions at 30 °C/23%RH. These regions were still visible on day 22. As the gamma polymorph is SFG/SHG inactive, this activity was most likely to be due to either (i) small amounts of the alpha form or (ii) small amounts of some other SFG/SHG active form. Extracted CARS spectra from these regions suggested the alpha form (Figure 29, spot 9). Similarly, with the tablets stored at 30 °C/75%RH, some regions generated a CARS signal at 1701 cm^{-1} (attributed to the gamma form).

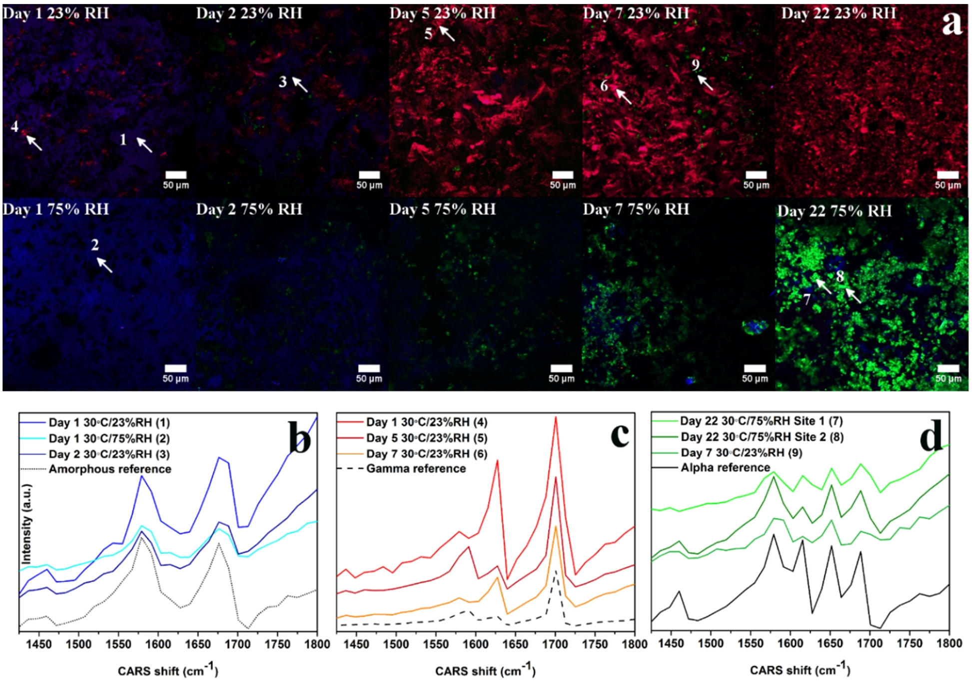

Figure 29. Multimodal narrowband (single-shift) CARS and SFG/SHG images of amorphous indomethacin tablets during storage at 30 °C/23%RH (top) and 30 °C/75%RH (bottom) (a). Images are overlaid CARS signal detected at 1701 cm^{-1} for gamma indomethacin (red), 1676 cm^{-1} for amorphous indomethacin (blue), and SFG/SHG signals for alpha indomethacin (green). CARS spectra extracted from the red, green, and blue regions are indicated by arrows and numbers 1–9 (b–d). Reference spectra of the different solid-state forms of indomethacin are shown for comparison in black (b–d). The spectra are offset for clarity. Reprinted from publication (**IV**) with permission. Copyright (2017) American Chemical Society.

FTIR-ATR spectroscopy and Raman microscopy were also performed on the same tablets. Gamma indomethacin was confirmed by FTIR-ATR spectroscopy after 5 days' storage at 30 °C/23%RH. This method also confirmed alpha indomethacin at 30 °C/75% RH after 22 days of storage with a peak associated with the alpha form (1650 cm^{-1}) appearing in the IR spectra. Gamma indomethacin was also observed on the surfaces of tablets stored at 30 °C/23%RH using Raman microscopy with the gamma peak at 1701 cm^{-1} visible after 5 days. However, alpha indomethacin was not clearly observed with Raman microscopy on the tablets stored at 30 °C/75%RH. Instead, the Raman spectra, supported by their PCA scores plot, resembled that of amorphous indomethacin.

The observations suggest that SFG/SHG imaging is more sensitive than Raman microscopy in detecting small amounts of (alpha form) crystallinity on tablet surfaces. This is likely to be due to the different spatial (axial and lateral) resolutions (SFG/SHG imaging having higher resolution) of the two techniques and high sensitivity of SFG/SHG imaging to non-centrosymmetric crystals,[198] combined with the small size (nanometer scale width), needle-like morphology, growth patterns, and limited tablet surface coverage of the alpha indomethacin crystals, as also evidenced by SEM analysis. Furthermore, SHG/SFG imaging could reveal crystallization earlier than FTIR-ATR and Raman microscopy.

In conclusion it was shown that multimodal CARS and SHG/SFG imaging is a sensitive method for detecting surface crystallization. This study demonstrated the feasibility and potential benefits of such multimodal non-linear imaging method in visualizing multiple solid-state forms of an API on surfaces and monitoring subtle but potentially important solid-state changes during storage. The combination of these methodologies is especially beneficial, since SFG/SHG imaging was very sensitive to non-centrosymmetric crystals on tablet surfaces, and CARS imaging, with detection based on molecular vibrations, was successfully used to distinguish the solid-state forms of the API that could not be resolved using SFG/SHG imaging. In addition, imaging has the inherent benefit of allowing direct visualization of the distribution of even small regions of chemical components in the sample. Further improvement in the SFG/SHG sensitivity and in the speed of CARS spectral imaging could be obtained by using ultrashort, broadband excitation pulses. This comes, however, at a cost of added complexity in the imaging setup. With the increasing availability of (fully integrated) non-linear optical imaging setups, these methodologies have potential for widespread characterization and optimization of solid-state forms of drugs and dosage forms in the pharmaceutical industry. Since the imaging methods are also nondestructive, the same imaged samples may then be subjected to subsequent pharmaceutical testing. This would allow the relationship between surface characteristics and critical quality attributes (e.g., dissolution) to be better understood, optimized, and controlled.

6 Conclusions

In this Thesis, the capabilities of non-linear optical imaging, especially coherent anti-Stokes Raman scattering (CARS) and second harmonic- and sum-frequency generation (SHG/SFG) microscopies in pharmaceutical applications were evaluated. Studies included live cell imaging of Caco-2 cell cultures on membrane inserts, nanocrystal cellular uptake and solid-state analysis in pharmaceutics.

In the first study it was shown that label-free and chemically-specific CARS microscopy is a suitable technique to image live cell cultures on membrane inserts suitable for routine drug permeation studies. The most suitable insert material for imaging was found to be PTFE. Live Caco-2 cell cultures on PTFE inserts were imaged in HBSS-HEPES buffer for the first time using CARS microscopy. Using this technique, lipid droplets in cell cultures could be non-invasively probed by exploiting the vibrational resonance of symmetric CH_2 stretching of lipids. It was found that the number and size of the lipid droplets increased substantially over a 21-day culturing period, which is important in the context of drug permeation studies, since the lipid content in Caco-2 cell cultures and potentially other cells can influence drug permeation.

In the next two studies, the potential of non-linear optical imaging to analyze unlabeled nanoparticle cellular uptake was investigated. First, it was shown that CARS microscopy is a suitable tool for detecting unlabeled nanocrystals in biological matrices as demonstrated with drug nanocrystals. By exploiting the CH stretching modes, CARS microscopy as a label-free, chemically-specific and inherently confocal technique, was successfully used to visualize non-fluorescent PP-NCs having dimensions larger than the optical lateral resolution of approximately 400 nm, in relation to the cellular framework in cell cultures, as well as *ex vivo* in histological sections. Nanoparticle cellular uptake was further studied by developing a correlative imaging technique combining CARS microscopy and electron microscopy. In this way, a correlative coherent anti-Stokes Raman scattering and electron microscopy (C-CARS-EM) platform was developed. This method combines the inherent benefits of two of the techniques: chemical-specificity of CARS and (sub)nanometer spatial resolution of EM. The cellular uptake of GLI-NCs was visualized using this method so that exactly the same cells could be imaged with both imaging modalities. CARS microscopy with spectroscopy was successfully used to identify GLI-NCs inside the cells in a chemically-specific way and the subcellular localization of nanocrystals inside the cells could be probed using EM. Based on the morphological analysis, nanocrystals were located in the vesicles expressing multivesicular body (MVB)-like morphology typical for late endosomes (LEs), endolysosomes and phagolysosomes. Therefore, as demonstrated with drug nanocrystals, this correlative imaging technique is well applicable for studying the interactions between nanoparticles and cells in detail. The information obtained from these studies can be used to gain in-depth knowledge about subtle mechanisms by which cells take up nanoparticles, which should facilitate the development of successful and safe nanomedicines.

In the fourth study, the potential of multimodal non-linear optical imaging to visualize pharmaceutical multiple solid-state forms on surfaces was investigated. Two non-linear imaging modalities were used simultaneously and successfully to visualize the distribution of amorphous, gamma and alpha indomethacin on tablet surfaces with two different approaches: hyperspectral imaging and narrowband (single-shift) imaging. Furthermore, the imaging approach was utilized to visualize surface crystallization of indomethacin with high sensitivity and solid-state specificity. The synergistic use of two non-linear optical microscopy methods relying on different mechanisms (detection of molecular vibrations (CARS) and SFG signal produced by non-centrosymmetric crystals) improves the image interpretation confidence. It was found that SFG/SHG imaging was very sensitive to non-centrosymmetric crystals on tablet surfaces, and CARS imaging, with detection based on molecular vibrations, was successfully used to distinguish solid states of the API that could not be resolved using SFG/SHG imaging.

Overall, non-linear optical imaging has great potential in pharmaceutical applications that the industry, academia and regulatory authorities can benefit from during drug development. Non-linear microscopes, especially coherent Raman microscopes capable of SRS and/or CARS, are being actively developed, with a focus on imaging speed and spatial and spectral resolution. At the moment, most of the developed instruments are still lab-built, but commercialization is expected to increase, especially as more applications are demonstrated. As demonstrated in this Thesis, these imaging techniques can already be used in pharmaceutically important applications including imaging of live cells, nanoparticle cellular uptake and solid-state form analysis on surfaces. It can be foreseen that these imaging modalities will be widely available and used in the pharmaceutical industry in the near future.

References

(1) Paul, S. M.; Mytelka, D. S.; Dunwiddie, C. T.; Persinger, C. C.; Munos, B. H.; Lindborg, S. R.; Schacht, A. L. How to Improve R&D Productivity: The Pharmaceutical Industry's Grand Challenge. *Nat. Rev. Drug Discov.* **2010**, *9*, 203–214.

(2) Dickson, M.; Gagnon, J. P. Key Factors in the Rising Cost of New Drug Discovery and Development. *Nat. Rev. Drug Discov.* **2004**, *3*, 417–429.

(3) Desai, P. P.; Date, A. A.; Patravale, V. B. Overcoming Poor Oral Bioavailability Using Nanoparticle Formulations - Opportunities and Limitations. *Drug Discov. Today Technol.* **2012**, *9*, 87–95.

(4) Chieng, N.; Rades, T.; Aaltonen, J. An Overview of Recent Studies on the Analysis of Pharmaceutical Polymorphs. *J. Pharm. Biomed. Anal.* **2011**, *55*, 618–644.

(5) Tuomela, A.; Saarinen, J.; Strachan, C. J.; Hirvonen, J.; Peltonen, L. Production, Applications and in Vivo Fate of Drug Nanocrystals. *J. Drug Deliv. Sci. Technol.* **2016**, *34*, 1–11.

(6) He, Y.; Xia, D.; Li, Q.; Tao, J.; Gan, Y.; Wang, C. Enhancement of Cellular Uptake, Transport and Oral Absorption of Protease Inhibitor Saquinavir by Nanocrystal Formulation. *Acta Pharmacol. Sin.* **2015**, *36*, 1151–1160.

(7) Florence, A. T. The Oral Absorption of Micro- and Nanoparticulates: Neither Exceptional Nor Unusual. *Pharm. Res.* **1997**, *14*, 259–266.

(8) Darville, N.; Van Heerden, M.; Vynckier, A.; De Meulder, M.; Sterkens, P.; Annaert, P.; Van Den Mooter, G. Intramuscular Administration of Paliperidone Palmitate Extended-Release Injectable Microsuspension Induces a Subclinical Inflammatory Reaction Modulating the Pharmacokinetics in Rats. *J. Pharm. Sci.* **2014**, *103*, 2072–2087.

(9) Hu, X.; Fan, W.; Yu, Z.; Lu, Y.; Qi, J.; Zhang, J.; Dong, X.; Zhao, W.; Wu, W. Evidence Does Not Support Absorption of Intact Solid Lipid Nanoparticles via Oral Delivery. *Nanoscale* **2016**, *8*, 7024–7035.

(10) Santos, H. A.; Mäkilä, E.; Airaksinen, A. J.; Bimbo, L. M.; Hirvonen, J. Porous Silicon Nanoparticles for Nanomedicine: Preparation and Biomedical Applications. *Nanomedicine* **2014**, *9*, 535–554.

(11) Banik, B. L.; Fattahi, P.; Brown, J. L. Polymeric Nanoparticles: The Future of Nanomedicine. *Wiley Interdiscip. Rev. Nanomedicine Nanobiotechnology* **2016**, *8*, 271–299.

(12) Daraee, H.; Etemadi, A.; Kouhi, M.; Alimirzalu, S.; Akbarzadeh, A. Application of Liposomes in Medicine and Drug Delivery. *Artif. Cells, Nanomedicine, Biotechnol.* **2014**, *1401*, 1–11.

(13) Vader, P.; Mol, E. A.; Pasterkamp, G.; Schiffelers, R. M. Extracellular Vesicles for Drug Delivery. *Adv. Drug Deliv. Rev.* **2016**, *106*, 148–156.

(14) McCarthy, C. A.; Ahern, R. J.; Dontireddy, R.; Ryan, K. B.; Crean, A. M. Mesoporous Silica Formulation Strategies for Drug Dissolution Enhancement: A Review. *Expert Opin. Drug Deliv.* **2016**, *13*, 93–108.

(15) Fontana, F.; Liu, D.; Hirvonen, J.; Santos, H. A. Delivery of Therapeutics with Nanoparticles: What's New in Cancer Immunotherapy? *Wiley Interdiscip. Rev. Nanomedicine Nanobiotechnology* **2017**, *9*, 1–26.

(16) Bae, Y. H.; Park, K. Targeted Drug Delivery to Tumors: Myths, Reality and Possibility. *J. Control. Release* **2011**, *153*, 198–205.

(17) Datta, S.; Grant, D. J. W. Crystal Structures of Drugs: Advances in Determination, Prediction and Engineering. *Nat. Rev. Drug Discov.* **2004**, *3*, 42–57.

(18) Chemburkar, S. R.; Bauer, J.; Deming, K.; Spiwek, H.; Patel, K.; Morris, J.; Henry, R.; Spanton, S.; Dziki, W.; Porter, W.; *et al.* Dealing with the Impact of Ritonavir Polymorphs on the Late Stages of Bulk Drug Process Development. *Org. Process Res. Dev.* **2000**, *4*, 413–417.

(19) Gilmore, C. J. X-Ray Diffraction. In *Solid State Characterization of Pharmaceuticals*; Storey, R. A.; Ymén, I., Eds.; John Wiley & Sons, 2011; pp. 35–70.

(20) Gabbott, P. A Practical Introduction to Differential Scanning Calorimetry. In *Principles*

and Applications of Thermal Analysis; Gabbot, P., Ed.; Blackwell Publishing Ltd, 2008; pp. 1–50.

(21) Qi, S. Thermal Analysis of Pharmaceuticals. In *Analytical Techniques in the Pharmaceutical Sciences*; Müllertz, A.; Perrie, Y.; Rades, T., Eds.; Springer, 2016; pp. 363–388.

(22) Oldenbourg, R. Polarized Light Microscopy: Principles and Practice. *Cold Spring Harb. Protoc.* **2013**, 1023–1036.

(23) Bunjes, H.; Kuntsche, J. Light and Electron Microscopy. In *Analytical Techniques in the Pharmaceutical Sciences*; Müllertz, A.; Perrie, Y.; Rades, T., Eds.; Springer, 2016; pp. 491–522.

(24) Fraser-Miller, S. J.; Saarinen, J.; Strachan, C. J. Vibrational Spectroscopic Imaging. In *Analytical Techniques in the Pharmaceutical Sciences*; Müllertz, A.; Perrie, Y.; Rades, T., Eds.; Springer, 2016; pp. 523–589.

(25) Heinz, A.; Strachan, C. J.; Gordon, K. C.; Rades, T. Analysis of Solid-State Transformations of Pharmaceutical Compounds Using Vibrational Spectroscopy. *J. Pharm. Pharmacol.* **2009**, *61*, 971–988.

(26) Evanko, D.; Heinrichs, A.; Rosenthal, C. K. Milestones in Optical Microscopy. *Nat. Cell Biol.* **2009**, *11*, S6–S22.

(27) Minsky, M. Microscopy Apparatus. US Patent 3,013,467, 1961.

(28) Lichtman, J. W.; Conchello, J.-A. Fluorescence Microscopy. *Nat. Methods* **2005**, *2*, 910–919.

(29) Coons, A. H.; Creech, H. J.; Jones, R. N. Immunological Properties of an Antibody Containing a Fluorescent Group. *Exp. Biol. Med.* **1941**, *47*, 200–202.

(30) Coons, A. H. Creech, H. J., Jones, N. and Berliner, E. The Demonstration of Pneumococcal Antigen in Tissues by the Use of Fluorescent Antibody. *J. Immunol.* **1942**, *45*, 159–170.

(31) Ehrhardt, D. GFP Technology for Live Cell Imaging. *Curr. Opin. Plant Biol.* **2003**, *6*, 622–628.

(32) Chalfie, M.; Tu, Y.; Euskirchen, G.; Ward, W. W.; Prashert, D. C. Green Fluorescent Protein as a Marker for Gene Expression. *Science.* **1994**, *263*, 802–805.

(33) Prasher, D. C.; Eckenrode, V. K.; Ward, W. W.; Prendergast, F. G.; Cormier, M. J. Primary Structure of the Aequorea Victoria Green-Fluorescent Protein. *Gene* **1992**, *111*, 229–233.

(34) Murray, J. M. *Basic Methods in Microscopy, Protocols and Concepts from Cells: A Laboratory Manual*; Spector, D. L.; Goldman, R. D., Eds.; Cold Spring Harbor Laboratory Press, 2006.

(35) Basuki, J. S.; Duong, H. T. T.; Macmillan, A.; Erlich, R. B.; Esser, L.; Akerfeldt, M. C.; Whan, R. M.; Kavallaris, M.; Boyer, C.; Davis, T. P. Using Fluorescence Lifetime Imaging Microscopy to Monitor Theranostic Nanoparticle Uptake and Intracellular Doxorubicin Release. *ACS Nano* **2013**, *7*, 10175–10189.

(36) Ji, X.; Peng, F.; Zhong, Y.; Su, Y.; Jiang, X.; Song, C.; Yang, L.; Chu, B.; Lee, S. T.; He, Y. Highly Fluorescent, Photostable, and Ultrasmall Silicon Drug Nanocarriers for Long-Term Tumor Cell Tracking and in-Vivo Cancer Therapy. *Adv. Mater.* **2015**, *27*, 1029–1034.

(37) Chuah, L. H.; Roberts, C. J.; Billa, N.; Abdullah, S.; Rosli, R. Cellular Uptake and Anticancer Effects of Mucoadhesive Curcumin-Containing Chitosan Nanoparticles. *Colloids Surfaces B Biointerfaces* **2014**, *116*, 228–236.

(38) Zhao, R.; Hollis, C. P.; Zhang, H.; Sun, L.; Gemeinhart, R. A.; Li, T. Hybrid Nanocrystals: Achieving Concurrent Therapeutic and Bioimaging Functionalities toward Solid Tumors. *Mol. Pharm.* **2011**, *8*, 1985–1991.

(39) Mahmoud, K. A.; Mena, J. A.; Male, K. B.; Hrapovic, S.; Kamen, A.; Luong, J. H. T. Effect of Surface Charge on the Cellular Uptake and Cytotoxicity of Fluorescent Labeled Cellulose Nanocrystals. *ACS Appl. Mater. Interfaces* **2010**, *2*, 2924–2932.

(40) Huang, M.; Ma, Z.; Khor, E.; Lim, L. Y. Uptake of FITC-Chitosan Nanoparticles by A549 Cells. *Pharm. Res.* **2002**, *19*, 1488–1494.

(41) Andar, A. U.; Hood, R. R.; Vreeland, W. N.; Devoe, D. L.; Swaan, P. W. Microfluidic

Preparation of Liposomes to Determine Particle Size Influence on Cellular Uptake Mechanisms. *Pharm. Res.* **2014**, *31*, 401–413.

(42) Hillaireau, H.; Couvreur, P. Nanocarriers' Entry into the Cell: Relevance to Drug Delivery. *Cell. Mol. Life Sci.* **2009**, *66*, 2873–2896.

(43) Chen, Y.; Li, T. Cellular Uptake Mechanism of Paclitaxel Nanocrystals Determined by Confocal Imaging and Kinetic Measurement. *AAPS J.* **2015**, *17*, 1126–1134.

(44) Born, M.; Wolf, E. *Principles of Optics: Electromagnetic Theory of Propagation, Interference and Diffraction of Light*; Born, M.; Wolf, E., Eds.; Cambridge University Press, 2002.

(45) Hell, S. W.; Dyba, M.; Jakobs, S. Concepts for Nanoscale Resolution in Fluorescence Microscopy. *Curr. Opin. Neurobiol.* **2004**, *14*, 599–609.

(46) Klar, T. A.; Jakobs, S.; Dyba, M.; Egner, A.; Hell, S. W. Fluorescence Microscopy with Diffraction Resolution Barrier Broken by Stimulated Emission. *Proc. Natl. Acad. Sci.* **2000**, *97*, 8206–8210.

(47) Betzig, E.; Patterson, G. H.; Sougrat, R.; Lindwasser, O. W.; Olenych, S.; Bonifacino, J. S.; Davidson, M. W.; Lippincott-Schwartz, J.; Hess, H. F. Imaging Intracellular Fluorescent Proteins at Nanometer Resolution. *Science.* **2006**, *313*, 1642–1645.

(48) Rust, M. J.; Bates, M.; Zhuang, X. Sub-Diffraction-Limit Imaging by Stochastic Optical Reconstruction Microscopy (STORM). *Nat. Methods* **2006**, *3*, 793–796.

(49) Kamiyama, D.; Huang, B. Development in the STORM. *Dev. Cell* **2012**, *23*, 1103–1110.

(50) Van Der Zwaag, D.; Vanparijs, N.; Wijnands, S.; De Rycke, R.; De Geest, B. G.; Albertazzi, L. Super Resolution Imaging of Nanoparticles Cellular Uptake and Trafficking. *ACS Appl. Mater. Interfaces* **2016**, *8*, 6391–6399.

(51) Koster, A. J.; Klumperman, J. Electron Microscopy in Cell Biology: Integrating Structure and Function. *Nat. Rev. Mol. Cell Biol.* **2003**, *Suppl*, SS6-10.

(52) Schirra, R. T.; Zhang, P. Correlative Fluorescence and Electron Microscopy. *Curr. Protoc. Cytom.* **2014**, 12.36.1-12.36.10.

(53) Tenuta, T.; Monopoli, M. P.; Kim, J.; Salvati, A.; Dawson, K. A.; Sandin, P.; Lynch, I. Elution of Labile Fluorescent Dye from Nanoparticles during Biological Use. *PLoS One* **2011**, *6*, e25556.

(54) Fernández-Suárez, M.; Ting, A. Y. Fluorescent Probes for Super-Resolution Imaging in Living Cells. *Nat Rev Mol Cell Biol* **2008**, *9*, 929–943.

(55) Pope, I.; Payne, L.; Zoriniants, G.; Thomas, E.; Williams, O.; Watson, P.; Langbein, W.; Borri, P. Coherent Anti-Stokes Raman Scattering Microscopy of Single Nanodiamonds. *Nat. Nanotechnol.* **2014**, *9*, 940–946.

(56) Smith, E.; Dent, G. *Modern Raman Spectroscopy, A Practical Approach*; Smith, E.; Dent, G., Eds.; John Wiley & Sons, 2005.

(57) Colthup, N. B.; Daly, L. H.; Wiberley, S. E. *Introduction to Infrared and Raman Spectroscopy*; Colthup, N. B.; Daly, L. H.; Wiberley, S. E., Eds.; 3rd edition.; Academic Press, 1990.

(58) Raman, C. V.; Krishnan, K. S. A New Type of Secondary Radiation. *Nature* **1928**, *121*, 501–502.

(59) Raman, C. V. A New Radiation. *Indian J. Phys.* **1928**, *2*, 387–398.

(60) Boyd, R. W. *Nonlinear Optics*; Boyd, R. W., Ed.; 3rd edition.; Academic Press, 2008.

(61) Chase, D. B. Fourier Transform Raman Spectroscopy. *J. Am. Chem. Soc.* **1986**, *108*, 7485–7488.

(62) Gordon, K. C.; McGoverin, C. M. Raman Mapping of Pharmaceuticals. *Int. J. Pharm.* **2011**, *417*, 151–162.

(63) Hedegaard, M.; Matthäus, C.; Hassing, S.; Krafft, C.; Diem, M.; Popp, J. Spectral Unmixing and Clustering Algorithms for Assessment of Single Cells by Raman Microscopic Imaging. *Theor. Chem. Acc.* **2011**, *130*, 1249–1260.

(64) Butler, H. J.; Ashton, L.; Bird, B.; Cinque, G.; Curtis, K.; Dorney, J.; Esmonde-White, K.; Fullwood, N. J.; Gardner, B.; Martin-Hirsch, P. L.; *et al.* Using Raman Spectroscopy to Characterize Biological Materials. *Nat. Protoc.* **2016**, *11*, 664–687.

(65) Majzner, K.; Kaczor, A.; Kachamakova-Trojanowska, N.; Fedorowicz, A.; Chlopicki, S.; Baranska, M. 3D Confocal Raman Imaging of Endothelial Cells and Vascular Wall:

Perspectives in Analytical Spectroscopy of Biomedical Research. *Analyst* **2013**, *138*, 603–610.

(66) Kallepitis, C.; Bergholt, M. S.; Mazo, M. M.; Leonardo, V.; Skaalure, S. C.; Maynard, S. A.; Stevens, M. M. Quantitative Volumetric Raman Imaging of Three Dimensional Cell Cultures. *Nat. Commun.* **2017**, *8*, 14843.

(67) Puppels, G. J.; de Mul, F. F.; Otto, C.; Greve, J.; Robert-Nicoud, M.; Arndt-Jovin, D. J.; Jovin, T. M. Studying Single Living Cells and Chromosomes by Confocal Raman Microspectroscopy. *Nature* **1990**, *347*, 301–303.

(68) Kann, B.; Offerhaus, H. L.; Windbergs, M.; Otto, C. Raman Microscopy for Cellular Investigations - From Single Cell Imaging to Drug Carrier Uptake Visualization. *Adv. Drug Deliv. Rev.* **2015**, *89*, 71–90.

(69) El-Mashtoly, S. F.; Petersen, D.; Yosef, H. K.; Mosig, A.; Reinacher-Schick, A.; Kötting, C.; Gerwert, K. Label-Free Imaging of Drug Distribution and Metabolism in Colon Cancer Cells by Raman Microscopy. *Analyst* **2014**, *139*, 1155–1161.

(70) Tipping, W. J.; Lee, M.; Serrels, A.; Brunton, V. G.; Hulme, A. N. Stimulated Raman Scattering Microscopy: An Emerging Tool for Drug Discovery. *Chem. Soc. Rev.* **2016**, *45*, 2075–2089.

(71) Yamakoshi, H.; Dodo, K.; Palonpon, A.; Ando, J.; Fujita, K.; Kawata, S.; Sodeoka, M. Alkyne-Tag Raman Imaging for Visualization of Mobile Small Molecules in Live Cells. *J. Am. Chem. Soc.* **2012**, *134*, 20681–20689.

(72) Yamakoshi, H.; Dodo, K.; Okada, M.; Ando, J.; Palonpon, A.; Fujita, K.; Kawata, S.; Sodeoka, M. Imaging of EdU, an Alkyne-Tagged Cell Proliferation Probe, by Raman Microscopy. *J. Am. Chem. Soc.* **2011**, *133*, 6102–6105.

(73) Hong, S.; Chen, T.; Zhu, Y.; Li, A.; Huang, Y.; Chen, X. Live-Cell Stimulated Raman Scattering Imaging of Alkyne-Tagged Biomolecules. *Angew. Chemie - Int. Ed.* **2014**, *53*, 5827–5831.

(74) Palonpon, A. F.; Ando, J.; Yamakoshi, H.; Dodo, K.; Sodeoka, M.; Kawata, S.; Fujita, K. Raman and SERS Microscopy for Molecular Imaging of Live Cells. *Nat. Protoc.* **2013**, *8*, 677–692.

(75) Widjaja, E.; Seah, R. K. H. Application of Raman Microscopy and Band-Target Entropy Minimization to Identify Minor Components in Model Pharmaceutical Tablets. *J. Pharm. Biomed. Anal.* **2008**, *46*, 274–281.

(76) Vajna, B.; Farkas, I.; Szabó, A.; Zsigmond, Z.; Marosi, G. Raman Microscopic Evaluation of Technology Dependent Structural Differences in Tablets Containing Imipramine Model Drug. *J. Pharm. Biomed. Anal.* **2010**, *51*, 30–38.

(77) Vajna, B.; Pataki, H.; Nagy, Z.; Farkas, I.; Marosi, G. Characterization of Melt Extruded and Conventional Isoptin Formulations Using Raman Chemical Imaging and Chemometrics. *Int. J. Pharm.* **2011**, *419*, 107–113.

(78) Nakamoto, K.; Urasaki, T.; Hondo, S.; Murahashi, N.; Yonemochi, E.; Terada, K. Evaluation of the Crystalline and Amorphous States of Drug Products by Nanothermal Analysis and Raman Imaging. *J. Pharm. Biomed. Anal.* **2013**, *75*, 105–111.

(79) Vajna, B.; Farkas, I.; Farkas, A.; Pataki, H.; Nagy, Z.; Madarász, J.; Marosi, G. Characterization of Drug-Cyclodextrin Formulations Using Raman Mapping and Multivariate Curve Resolution. *J. Pharm. Biomed. Anal.* **2011**, *56*, 38–44.

(80) Fujimaki, Y.; Matsubara, T.; Sakamoto, T.; Sasakura, D.; Miura, T.; Takekawa, M.; Hiyama, Y. Distribution of Ethenzamide and Other Ingredients on Granule Surfaces Studied by Raman Microspectroscopy and Mapping. *Pharmazie* **2009**, *64*, 316–322.

(81) Šašić, S.; Harding, L. Global Illumination Raman Chemical Imaging of a Combination of Two Drug Molecules in a Dry Powder Inhaler Formulation. *Anal. Methods* **2010**, *2*, 1528–1535.

(82) Schoenherr, C.; Haefele, T.; Paulus, K.; Francese, G. Confocal Raman Microscopy to Probe Content Uniformity of a Lipid Based Powder for Inhalation: A Quality by Design Approach. *Eur. J. Pharm. Sci.* **2009**, *38*, 47–54.

(83) Steele, D. F.; Young, P. M.; Price, R.; Smith, T.; Edge, S.; Lewis, D. The Potential Use of Raman Mapping to Investigate in Vitro Deposition of Combination Pressurized Metered-Dose Inhalers. *AAPS J.* **2004**, *6*, e32.

(84) Furuyama, N.; Hasegawa, S.; Hamaura, T.; Yada, S.; Nakagami, H.; Yonemochi, E.; Terada, K. Evaluation of Solid Dispersions on a Molecular Level by the Raman Mapping Technique. *Int. J. Pharm.* **2008**, *361*, 12–18.

(85) Sakamoto, T.; Matsubara, T.; Sasakura, D.; Takada, Y.; Fujimaki, Y.; Aida, K.; Miura, T.; Terahara, T.; Higo, N. Chemical Mapping of Tulobuterol in Transdermal Tapes Using Microscopic Laser Raman Spectroscopy. *Pharmazie* **2009**, *64*, 166–171.

(86) Edinger, M.; Bar-Shalom, D.; Rantanen, J.; Genina, N. Visualization and Non-Destructive Quantification of Inkjet-Printed Pharmaceuticals on Different Substrates Using Raman Spectroscopy and Raman Chemical Imaging. *Pharm. Res.* **2017**, *34*, 1023–1036.

(87) Haaser, M.; Windbergs, M.; McGoverin, C. M.; Kleinebudde, P.; Rades, T.; Gordon, K. C.; Strachan, C. J. Analysis of Matrix Dosage Forms during Dissolution Testing Using Raman Microscopy. *J. Pharm. Sci.* **2011**, *100*, 4452–4459.

(88) Pissuwan, D.; Hobro, A. J.; Pavillon, N.; Smith, N. I. Distribution of Label Free Cationic Polymer-Coated Gold Nanorods in Live Macrophage Cells Reveals Formation of Groups of Intracellular SERS Signals of Probe Nanoparticles. *RSC Adv.* **2014**, *4*, 5536–5541.

(89) Lahr, R. H.; Vikesland, P. J. Surface-Enhanced Raman Spectroscopy (SERS) Cellular Imaging of Intracellulary Biosynthesized Gold Nanoparticles. *ACS Sustain. Chem. Eng.* **2014**, *2*, 1599–1608.

(90) Baik, J.; Rosania, G. R. Molecular Imaging of Intracellular Drug-Membrane Aggregate Formation. *Mol. Pharm.* **2011**, *8*, 1742–1749.

(91) Heidari Torkabadi, H.; Bethel, C. R.; Papp-Wallace, K. M.; De Boer, P. A. J.; Bonomo, R. A.; Carey, P. R. Following Drug Uptake and Reactions inside Escherichia Coli Cells by Raman Microspectroscopy. *Biochemistry* **2014**, *53*, 4113–4121.

(92) Lin, W.; Jiang, J.; Yang, H.; Ozaki, Y.; Shen, G.; Yu, R. Characterization of Chloramphenicol Palmitate Drug Polymorphs by Raman Mapping with Multivariate Image Segmentation Using a Spatial. *Anal. Chem.* **2006**, *78*, 6003–6011.

(93) Armstrong, C. L.; Edwards, H. G. M.; Farwell, D. W.; Williams, A. C. Fourier Transform Raman Microscopic Study of Drug Distribution in a Transdermal Drug Delivery Device. *Vib. Spectrosc.* **1996**, *11*, 105–113.

(94) Bell, S. E. J.; Dennis, A. C.; Fido, L. A.; Malcolm, R. K.; Sirimuthu, N. M. S.; Toner, C. F.; Woolfson, A. D. Characterization of Silicone Elastomer Vaginal Rings Containing HIV Microbicide TMC120 by Raman Spectroscopy. *J. Pharm. Pharmacol.* **2007**, *59*, 203–207.

(95) Docoslis, A.; Huszarik, K. L.; Papageorgiou, G. Z.; Bikiaris, D.; Stergiou, D.; Georgarakis, E. Characterization of the Distribution, Polymorphism, and Stability of Nimodipine in Its Solid Dispersions in Polyethylene Glycol by Micro-Raman Spectroscopy and Powder X-Ray Diffraction. *AAPS J.* **2007**, *9*, E361–E370.

(96) Widjaja, E.; Kanaujia, P.; Lau, G.; Ng, W. K.; Garland, M.; Saal, C.; Hanefeld, A.; Fischbach, M.; Maio, M.; Tan, R. B. H. Detection of Trace Crystallinity in an Amorphous System Using Raman Microscopy and Chemometric Analysis. *Eur. J. Pharm. Sci.* **2011**, *42*, 45–54.

(97) Doub, W. H.; Adams, W. P.; Spencer, J. A.; Buhse, L. F.; Nelson, M. P.; Treado, P. J. Raman Chemical Imaging for Ingredient-Specific Particle Size Characterization of Aqueous Suspension Nasal Spray Formulations: A Progress Report. *Pharm. Res.* **2007**, *24*, 934–945.

(98) Kane, K. M.; Ashvar, C. S.; Albrecht, M.; Smith, P. A.; Mele, P. A. Thermal Inkjet Application in the Preparation of Oral Dosage Forms : Dispensing of Prednisolone Solutions and Polymorphic Characterization by Solid-State Spectroscopic Techniques. *J. Pharm. Sci.* **2008**, *97*, 2619–2636.

(99) Min, W.; Freudiger, C. W.; Lu, S.; Xie, X. S. Coherent Nonlinear Optical Imaging: Beyond Fluorescence Microscopy. *Annu. Rev. Phys. Chem.* **2011**, *62*, 507–530.

(100) Evans, C. L.; Xie, X. S. Coherent Anti-Stokes Raman Scattering Microscopy: Chemical Imaging for Biology and Medicine. *Annu. Rev. Anal. Chem.* **2008**, *1*, 883–909.

(101) Franken, P. A.; Hill, A. E.; Peters, C. W.; Weinreich, G. Generation of Optical Harmonics. *Phys. Rev. Lett.* **1961**, *7*, 118–119.

(102) Bass, M.; Franken, P. A.; Hill, A. E.; Peters, C. W.; Weinreich, G. Optical Mixing. *Phys. Rev. Lett.* **1962**, *8*, 18.

(103) Zipfel, W. R.; Williams, R. M.; Webb, W. W. Nonlinear Magic: Multiphoton Microscopy in the Biosciences. *Nat. Biotechnol.* **2003**, *21*, 1369–1377.

(104) Denk, W.; Strickler, J. H.; Webb, W. W. Two-Photon Laser Scanning Fluorescence Microscopy. *Science*. **1990**, *248*, 73–76.

(105) Helmchen, F.; Denk, W. Deep Tissue Two-Photon Microscopy. *Nat. Methods* **2005**, *2*, 932–940.

(106) Rodriguez, L. G.; Lockett, S. J.; Holtom, G. R. Coherent Anti-Stokes Raman Scattering Microscopy: A Biological Review. *Cytometry. A* **2006**, *69*, 779–791.

(107) Strachan, C. J.; Windbergs, M.; Offerhaus, H. L. Pharmaceutical Applications of Non-Linear Imaging. *Int. J. Pharm.* **2011**, *417*, 163–172.

(108) Garrett, N. L.; Lalatsa, A.; Uchegbu, I.; Schätzlein, A.; Moger, J. Exploring Uptake Mechanisms of Oral Nanomedicines Using Multimodal Nonlinear Optical Microscopy. *J. Biophotonics* **2012**, *5*, 458–468.

(109) Cheng, J.-X.; Xie, X. S. Coherent Anti-Stokes Raman Scattering Microscopy: Instrumentation, Theory, and Applications. *J. Phys. Chem. B* **2004**, *108*, 827–840.

(110) Maker, P. D.; Terhune, R. W. Study of Optical Effects Due to an Induced Polarization Third Order in the Electric Field Strength. *Phys. Rev.* **1965**, *137*, A801–A818.

(111) Duncan, M. D.; Reintjes, J.; Manuccia, T. J. Scanning Coherent Anti-Stokes Raman Microscope. *Opt. Lett.* **1982**, *7*, 350–352.

(112) Zumbusch, A.; Holtom, G.; Xie, X. S. Three-Dimensional Vibrational Imaging by Coherent Anti-Stokes Raman Scattering. *Phys. Rev. Lett.* **1999**, *82*, 4142–4145.

(113) Cheng, J.-X.; Volkmer, A.; Xie, X. S. Theoretical and Experimental Characterization of Coherent Anti-Stokes Raman Scattering Microscopy. *J. Opt. Soc. Am. B* **2002**, *19*, 1363.

(114) Camp Jr, C. H.; Cicerone, M. T. Chemically Sensitive Bioimaging with Coherent Raman Scattering. *Nat. Photonics* **2015**, *9*, 295–305.

(115) Day, J. P. R.; Domke, K. F.; Rago, G.; Kano, H.; Hamaguchi, H.; Vartiainen, E. M.; Bonn, M. Quantitative Coherent Anti-Stokes Raman Scattering (CARS) Microscopy. *J. Phys. Chem. B* **2011**, *115*, 7713–7725.

(116) Hartshorn, C. M.; Lee, Y. J.; Camp, C. H.; Liu, Z.; Heddleston, J.; Canfield, N.; Rhodes, T. A.; Hight Walker, A. R.; Marsac, P. J.; Cicerone, M. T. Multicomponent Chemical Imaging of Pharmaceutical Solid Dosage Forms with Broadband CARS Microscopy. *Anal. Chem.* **2013**, *85*, 8102–8111.

(117) Evans, C. L.; Potma, E. O.; Puoris'haag, M.; Côté, D.; Lin, C. P.; Xie, X. S. Chemical Imaging of Tissue in Vivo with Video-Rate Coherent Anti-Stokes Raman Scattering Microscopy. *Proc. Natl. Acad. Sci. U. S. A.* **2005**, *102*, 16807–16812.

(118) Wong, C. S. Y.; Robinson, I.; Ochsenk, M. A.; Arlt, J.; Hossack, W. J.; Crain, J. Changes to Lipid Droplet Configuration in mCMV-Infected Fibroblasts : Live Cell Imaging with Simultaneous CARS and Two-Photon Fluorescence Microscopy. *Biomed. Opt. express* **2011**, *2*, 2504–2516.

(119) Garrett, N.; Whiteman, M.; Moger, J. Imaging the Uptake of Gold Nanoshells in Live Cells Using Plasmon Resonance Enhanced Four Wave Mixing Microscopy. *Opt. Express* **2011**, *19*, 17563–17574.

(120) Fu, Y.; Wang, H.; Shi, R.; Cheng, J. Characterization of Photodamage in Coherent Anti-Stokes Raman Scattering Microscopy. *Opt. Express* **2006**, *14*, 3942–3951.

(121) Cheng, J.-X.; Volkmer, A.; Book, L. D.; Xie, X. S. Multiplex Coherent Anti-Stokes Raman Scattering Microspectroscopy and Study of Lipid Vesicles. *J. Phys. Chem. B* **2002**, *106*, 8493–8498.

(122) Nan, X.; Cheng, J.-X.; Xie, X. S. Vibrational Imaging of Lipid Droplets in Live Fibroblast Cells with Coherent Anti-Stokes Raman Scattering Microscopy. *J. Lipid Res.* **2003**, *44*, 2202–2208.

(123) Wurpel, G. W. H.; Schins, J. M.; Müller, M. Chemical Specificity in Three-Dimensional Imaging with Multiplex Coherent Anti-Stokes Raman Scattering Microscopy. *Opt. Lett.* **2002**, *27*, 1093–1095.

(124) Müller, M.; Schins, J. M. Imaging the Thermodynamic State of Lipid Membranes with

Multiplex CARS Microscopy. *J. Phys. Chem. B* **2002**, *106*, 3715–3723.

(125) Kee, T. W.; Cicerone, M. T. Simple Approach to One-Laser , Broadband Coherent Anti-Stokes Raman Scattering Microscopy. *Opt. Lett.* **2004**, *29*, 2701–2703.

(126) Müller, M.; Schins, J. M. Imaging the Thermodynamic State of Lipid Membranes with Multiplex CARS Microscopy. *J. Phys. Chem. B* **2002**, *106*, 3715–3723.

(127) Lee, Y. J.; Cicerone, M. T. Vibrational Dephasing Time Imaging by Time-Resolved Broadband Coherent Anti-Stokes Raman Scattering Microscopy. *Appl. Phys. Lett.* **2008**, *92*.

(128) Parekh, S. H.; Lee, Y. J.; Aamer, K. A.; Cicerone, M. T. Label-Free Cellular Imaging by Broadband Coherent Anti-Stokes Raman Scattering Microscopy. *Biophys. J.* **2010**, *99*, 2695–2704.

(129) Lee, Y. J.; Parekh, S. H.; Kim, Y. H.; Cicerone, M. T. Optimized Continuum from a Photonic Crystal Fiber for Broadband Time-Resolved Coherent Anti-Stokes Raman Scattering. *Opt. Express* **2010**, *18*, 4371–4379.

(130) Hashimoto, K.; Takahashi, M.; Ideguchi, T.; Goda, K. Broadband Coherent Raman Spectroscopy Running at 24 , 000 Spectra per Second. *Sci. Rep* **2016**, 21036.

(131) Camp Jr, C. H.; Lee, Y. J.; Heddleston, J. M.; Hartshorn, C. M.; Walker, A. R. H.; Rich, J. N.; Lathia, J. D.; Cicerone, M. T. High-Speed Coherent Raman Fingerprint Imaging of Biological Tissues. *Nat. Photonics* **2014**, *8*, 627–634.

(132) Garbacik, E. T.; Herek, J. L.; Otto, C.; Offerhaus, H. L. Rapid Identification of Heterogeneous Mixture Components with Hyperspectral Coherent Anti-Stokes Raman Scattering Imaging. *J. Raman Spectrosc.* **2012**, *43*, 651–655.

(133) Lin, C.-Y.; Suhalim, J. L.; Nien, C. L.; Miljković, M. D.; Diem, M.; Jester, J. V; Potma, E. O. Picosecond Spectral Coherent Anti-Stokes Raman Scattering Imaging with Principal Component Analysis of Meibomian Glands. *J. Biomed. Opt.* **2011**, *16*, 021104-1-021104–021108.

(134) Lim, R. S.; Suhalim, J. L.; Miyazaki-Anzai, S.; Miyazaki, M.; Levi, M.; Potma, E. O.; Tromberg, B. J. Identification of Cholesterol Crystals in Plaques of Atherosclerotic Mice Using Hyperspectral CARS Imaging. *J. Lipid Res.* **2011**, *52*, 2177–2186.

(135) Freudiger, C. W.; Yang, W.; Holtom, G. R.; Peyghambarian, N.; Xie, X. S.; Kieu, K. Q. Stimulated Raman Scattering Microscopy with a Robust Fibre Laser Source. *Nat. Photonics* **2014**, *8*, 153–159.

(136) Berto, P.; Andresen, E. R.; Rigneault, H. Background-Free Stimulated Raman Spectroscopy and Microscopy. *Phys. Rev. Lett.* **2014**, *112*, 1–5.

(137) Prince, R. C.; Frontiera, R. R.; Potma, E. O. Stimulated Raman Scattering: From Bulk to Nano. *Chem. Rev.* **2017**, *117*, 5070–5094.

(138) Lu, F. K.; Calligaris, D.; Olubiyi, O. I.; Norton, I.; Yang, W.; Santagata, S.; Xie, X. S.; Golby, A. J.; Agar, N. Y. R. Label-Free Neurosurgical Pathology with Stimulated Raman Imaging. *Cancer Res.* **2016**, *76*, 3451–3462.

(139) Kong, L.; Ji, M.; Holtom, G. R.; Fu, D.; Freudiger, C. W.; Xie, X. S. Multicolor Stimulated Raman Scattering Microscopy with a Rapidly Tunable Optical Parametric Oscillator. *Opt. Lett.* **2013**, *38*, 145.

(140) Lu, F.-K.; Ji, M.; Fu, D.; Ni, X.; Freudiger, C. W.; Holtom, G.; Xie, X. S. Multicolor Stimulated Raman Scattering Microscopy. *Mol. Phys.* **2012**, *110*, 1927–1932.

(141) Ploetz, E.; Laimgruber, S.; Berner, S.; Zinth, W.; Gilch, P. Femtosecond Stimulated Raman Microscopy. *Appl. Phys. B Lasers Opt.* **2007**, *87*, 389–393.

(142) Fu, D.; Zhou, J.; Zhu, W. S.; Manley, P. W.; Wang, Y. K.; Hood, T.; Wylie, A.; Xie, X. S. Imaging the Intracellular Distribution of Tyrosine Kinase Inhibitors in Living Cells with Quantitative Hyperspectral Stimulated Raman Scattering. *Nat. Chem.* **2014**, *6*, 614–622.

(143) Wang, Y.; Lin, C.-Y.; Nikolaenko, A.; Raghunathan, V.; Potma, E. O. Four-Wave Mixing Microscopy of Nanostructures. *Adv. Opt. Photonics* **2011**, *3*, 1–52.

(144) Kachynski, A. V; Kuzmin, A. N.; Nyk, M.; Roy, I.; Prasad, P. N. Zinc Oxide Nanocrystals for Non-Resonant Nonlinear Optical Microscopy in Biology and Medicine. *J. Phys. Chem. C. Nanomater. Interfaces* **2008**, *112*, 10721–10724.

(145) Jung, Y.; Tong, L.; Tanaudommongkon, A.; Cheng, J.-X.; Yang, C. In Vitro and in Vivo

Nonlinear Optical Imaging of Silicon Nanowires. *Nano Lett.* **2009**, *9*, 2440–2444.

(146) Mah, P. T.; Novakovic, D.; Saarinen, J.; Van Landeghem, S.; Peltonen, L.; Laaksonen, T.; Isomäki, A.; Strachan, C. J. Elucidation of Compression-Induced Surface Crystallization in Amorphous Tablets Using Sum Frequency Generation (SFG) Microscopy. *Pharm. Res.* **2017**, *34*, 957–970.

(147) Kestur, U. S.; Wanapun, D.; Toth, S. J.; Wegiel, L. A.; Simpson, G. J.; Taylor, L. S. Nonlinear Optical Imaging for Sensitive Detection of Crystals in Bulk Amorphous Powders. *J. Pharm. Sci.* **2012**, *101*, 4201–4213.

(148) Gauderon, R.; Lukins, P. B.; Sheppard, G. J. R. Three-Dimensional Second-Harmonic Generation Imaging with Femtosecond Laser Pulses. *Opt. Lett.* **1998**, *23*, 1209–1211.

(149) Schmitt, P. D.; Trasi, N. S.; Taylor, L. S.; Simpson, G. J. Finding the Needle in the Haystack: Characterization of Trace Crystallinity in a Commercial Formulation of Paclitaxel Protein-Bound Particles by Raman Spectroscopy Enabled by Second Harmonic Generation Microscopy. *Mol. Pharm.* **2015**, *12*, 2378–2383.

(150) Wampler, R. D.; Kissick, D. J.; Dehen, C. J.; Gualtieri, E. J.; Grey, J. L.; Wang, H.-F.; Thompson, D. H.; Cheng, J.-X.; Simpson, G. J. Selective Detection of Protein Crystals by Second Harmonic Microscopy. Supporting Information. *J. Am. Chem. Soc.* **2008**, *130*, 14076–14077.

(151) Schenke-Layland, K.; Riemann, I.; Damour, O.; Stock, U. A.; König, K. Two-Photon Microscopes and in Vivo Multiphoton Tomographs--Powerful Diagnostic Tools for Tissue Engineering and Drug Delivery. *Adv. Drug Deliv. Rev.* **2006**, *58*, 878–896.

(152) Campagnola, P. J.; Loew, L. M. Second-Harmonic Imaging Microscopy for Visualizing Biomolecular Arrays in Cells, Tissues and Organisms. *Nat. Biotechnol.* **2003**, *21*, 1356–1360.

(153) Pirhonen, J.; Arola, J.; Sädevirta, S.; Luukkonen, P.; Karppinen, S. M.; Pihlajaniemi, T.; Isomäki, A.; Hukkanen, M.; Yki-Järvinen, H.; Ikonen, E. Continuous Grading of Early Fibrosis in NAFLD Using Label-Free Imaging: A Proof-of-Concept Study. *PLoS One* **2016**, *11*, 1–14.

(154) Kim, H.; Kim, D.-Y.; Joo, K.-I.; Kim, J.-H.; Jeong, S. M.; Lee, E. S.; Hahm, J.-H.; Kim, K.; Moon, D. W. Coherent Raman Imaging of Live Muscle Sarcomeres Assisted by SFG Microscopy. *Sci. Rep* **2017**, *7*, 9211.

(155) Shinzawa, H.; Awa, K.; Kanematsu, W.; Ozaki, Y. Multivariate Data Analysis for Raman Spectroscopic Imaging. *J. Raman Spectrosc.* **2009**, *40*, 1720–1725.

(156) Rajalahti, T.; Kvalheim, O. M. Multivariate Data Analysis in Pharmaceutics: A Tutorial Review. *Int. J. Pharm.* **2011**, *417*, 280–290.

(157) Ringnér, M. What Is Principal Component Analysis? *Nat. Biotechnol.* **2008**, *26*, 303–304.

(158) Pohling, C.; Buckup, T.; Motzkus, M. Hyperspectral Data Processing for Chemoselective Multiplex Coherent Anti-Stokes Raman Scattering Microscopy of Unknown Samples. *J Biomed Opt* **2011**, *16*, 021105-1-021105–021109.

(159) Winterhalder, M. J.; Zumbusch, A. Beyond the Borders - Biomedical Applications of Non-Linear Raman Microscopy. *Adv. Drug Deliv. Rev.* **2015**, *89*, 135–144.

(160) Alfonso-García, A.; Mittal, R.; Lee, E. S.; Potma, E. O. Biological Imaging with Coherent Raman Scattering Microscopy : A Tutorial Biological Imaging with Coherent Raman Scattering Microscopy : A Tutorial. *J. Biomed. Opt.* **2014**, *19*, 071407-1-071407–071413.

(161) Nan, X.; Potma, E. O.; Xie, X. S. Nonperturbative Chemical Imaging of Organelle Transport in Living Cells with Coherent Anti-Stokes Raman Scattering Microscopy. *Biophys. J.* **2006**, *91*, 728–735.

(162) Cheng, J.-X.; Jia, Y. K.; Zheng, G.; Xie, X. S. Laser-Scanning Coherent Anti-Stokes Raman Scattering Microscopy and Applications to Cell Biology. *Biophys. J.* **2002**, *83*, 502–509.

(163) Bonn, M.; Müller, M.; Rinia, H. A.; Burger, K. N. J. Imaging of Chemical and Physical State of Individual Cellular Lipid Droplets Using Multiplex CARS Microscopy. *J. Raman Spectrosc.* **2009**, *40*, 763–769.

(164) Zumbusch, A.; Langbein, W.; Borri, P. Nonlinear Vibrational Microscopy Applied to

Lipid Biology. *Prog. Lipid Res.* **2013**, *52*, 615–632.

(165) Kiskis, J.; Fink, H.; Nyberg, L.; Thyr, J.; Li, J.-Y.; Enejder, A. Plaque-Associated Lipids in Alzheimer's Diseased Brain Tissue Visualized by Nonlinear Microscopy. *Sci. Rep* **2015**, *5*, 13489.

(166) Cheng, J.-X.; Jia, Y. K.; Zheng, G.; Xie, X. S. Laser-Scanning Coherent Anti-Stokes Raman Scattering Microscopy and Applications to Cell Biology. *Biophys. J.* **2002**, *83*, 502–509.

(167) Hellerer, T.; Axäng, C.; Brackmann, C.; Hillertz, P.; Pilon, M.; Enejder, A. Monitoring of Lipid Storage in Caenorhabditis Elegans Using Coherent Anti-Stokes Raman Scattering (CARS) Microscopy. *Proc. Natl. Acad. Sci.* **2007**, *104*, 14658–14663.

(168) Pliss, A.; Kuzmin, A. N.; Kachynski, A. V.; Prasad, P. N. Biophotonic Probing of Macromolecular Transformations during Apoptosis. *Proc. Natl. Acad. Sci.* **2010**, *107*, 12771–12776.

(169) Pegoraro, A. F.; Slepkov, A. D.; Ridsdale, A.; Moffatt, D. J.; Stolow, A. Hyperspectral Multimodal CARS Microscopy in the Fingerprint Region. *J. Biophotonics* **2014**, *7*, 49–58.

(170) Lee, Y. J.; Vega, S. L.; Patel, P. J.; Aamer, K. A.; Moghe, P. V; Cicerone, M. T. Quantitative, Label-Free Characterization of Stem Cell Differentiation at the Single-Cell Level by Broadband Coherent Anti-Stokes Raman Scattering Microscopy. *Tissue Eng. Part C. Methods* **2014**, *20*, 562–569.

(171) Zhang, X.; Roeffaers, M. B. J.; Basu, S.; Daniele, J. R.; Fu, D.; Freudiger, C. W.; Holtom, G. R.; Xie, X. S. Label-Free Live-Cell Imaging of Nucleic Acids Using Stimulated Raman Scattering Microscopy. *ChemPhysChem* **2012**, *13*, 1054–1059.

(172) Garrett, N. L.; Lalatsa, A.; Begley, D.; Mihoreanu, L.; Uchegbu, I. F.; Schätzlein, A. G.; Moger, J. Label-Free Imaging of Polymeric Nanomedicines Using Coherent Anti-Stokes Raman Scattering Microscopy. *J. Raman Spectrosc.* **2012**, *43*, 681–688.

(173) Wei, L.; Hu, F.; Chen, Z.; Shen, Y.; Zhang, L.; Min, W. Live-Cell Bioorthogonal Chemical Imaging: Stimulated Raman Scattering Microscopy of Vibrational Probes. *Acc. Chem. Res.* **2016**, *49*, 1494–1502.

(174) Hu, F.; Chen, Z.; Zhang, L.; Shen, Y.; Wei, L.; Min, W. Vibrational Imaging of Glucose Uptake Activity in Live Cells and Tissues by Stimulated Raman Scattering. *Angew. Chemie - Int. Ed.* **2015**, *54*, 9821–9825.

(175) Wei, L.; Hu, F.; Shen, Y.; Chen, Z.; Yu, Y.; Lin, C.-C.; Wang, M. C.; Min, W. Live-Cell Imaging of Alkyne-Tagged Small Biomolecules by Stimulated Raman Scattering. *Nat. Methods* **2014**, *11*, 410–412.

(176) Chen, Z.; Paley, D. W.; Wei, L.; Weisman, A. L.; Friesner, R. A.; Nuckolls, C.; Min, W. Multicolor Live-Cell Chemical Imaging by Isotopically Edited Alkyne Vibrational Palette. *J. Am. Chem. Soc.* **2014**, *136*, 8027–8033.

(177) Wei, L.; Chen, Z.; Shi, L.; Long, R.; Anzalone, A. V.; Zhang, L.; Hu, F.; Yuste, R.; Cornish, V. W.; Min, W. Super-Multiplex Vibrational Imaging. *Nature* **2017**, *544*, 465–470.

(178) Fussell, A. L.; Grasmeijer, F.; Frijlink, H. W.; de Boer, A. H.; Offerhaus, H. L. CARS Microscopy as a Tool for Studying the Distribution of Micronised Drugs in Adhesive Mixtures for Inhalation. *J. Raman Spectrosc.* **2014**, *45*, 495–500.

(179) Christophersen, P. C.; Birch, D.; Saarinen, J.; Isomäki, A.; Nielsen, H. M.; Yang, M.; Strachan, C. J.; Mu, H. Investigation of Protein Distribution in Solid Lipid Particles and Its Impact on Protein Release Using Coherent Anti-Stokes Raman Scattering Microscopy. *J. Control. Release* **2015**, *197*, 111–120.

(180) Windbergs, M.; Jurna, M.; Offerhaus, H. L.; Herek, J. L.; Kleinebudde, P.; Strachan, C. J. Chemical Imaging of Oral Solid Dosage Forms and Changes upon Dissolution Using Coherent Anti-Stokes Raman Scattering Microscopy. *Anal. Chem.* **2009**, *81*, 2085–2091.

(181) Fussell, A.; Garbacik, E.; Offerhaus, H.; Kleinebudde, P.; Strachan, C. J. In Situ Dissolution Analysis Using Coherent Anti-Stokes Raman Scattering (CARS) and Hyperspectral CARS Microscopy. *Eur. J. Pharm. Biopharm.* **2013**, *85*, 1141–1147.

(182) Kang, E.; Robinson, J.; Park, K.; Cheng, J.-X. Paclitaxel Distribution in Poly(ethylene Glycol)/poly(lactide-Co-Glycolic Acid) Blends and Its Release Visualized by Coherent

Anti-Stokes Raman Scattering Microscopy. *J. Control. Release* **2007**, *122*, 261–268.

(183) Strachan, C. J.; Lee, C. J.; Rades, T. Partial Characterization of Different Mixtures of Solids by Measuring the Optical Nonlinear Response. *J. Pharm. Sci.* **2004**, *93*, 733–742.

(184) Kissick, D. J.; Gualtieri, E. J.; Simpson, G. J.; Cherezov, V. Nonlinear Optical Imaging of Integral Membrane Protein Crystals in Lipidic Mesophases. *Anal. Chem.* **2010**, *82*, 491–497.

(185) Chowdhury, A. U.; Ye, D. H.; Song, Z.; Zhang, S.; Hedderich, H. G.; Mallick, B.; Thirunahari, S.; Ramakrishnan, S.; Sengupta, A.; Gualtieri, E. J.; *et al.* Second Harmonic Generation Guided Raman Spectroscopy for Sensitive Detection of Polymorph Transitions. *Anal. Chem.* **2017**, *89*, 5958–5965.

(186) Jüngst, C.; Klein, M.; Zumbusch, A. Long-Term Live Cell Microscopy Studies of Lipid Droplet Fusion Dynamics in Adipocytes. *J. Lipid Res.* **2013**, *54*, 3419–3429.

(187) Segawa, H.; Okuno, M.; Kano, H.; Leproux, P.; Couderc, V.; Hamaguchi, H.-O. Label-Free Tetra-Modal Molecular Imaging of Living Cells with CARS, SHG, THG and TSFG (Coherent Anti-Stokes Raman Scattering, Second Harmonic Generation, Third Harmonic Generation and Third-Order Sum Frequency Generation). *Opt. Express* **2012**, *20*, 9551–9557.

(188) El-Mashtoly, S. F.; Niedieker, D.; Petersen, D.; Krauss, S. D.; Freier, E.; Maghnouj, A.; Mosig, A.; Hahn, S.; Kötting, C.; Gerwert, K. Automated Identification of Subcellular Organelles by Coherent Anti-Stokes Raman Scattering. *Biophys. J.* **2014**, *106*, 1910–1920.

(189) Lee, Y. J.; Vega, S. L.; Patel, P. J.; Aamer, K. A.; Moghe, P. V; Cicerone, M. T. Quantitative , Label-Free Characterization of Stem Cell Differentiation at the Single-Cell Level by Broadband Coherent Anti-Stokes Raman Scattering Microscopy. *Tissue Eng. Part C. Methods* **2014**, *20*, 562–569.

(190) Yang, W.; Li, A.; Suo, Y.; Lu, F. K.; Xie, X. S. Simultaneous Two-Color Stimulated Raman Scattering Microscopy by Adding a Fiber Amplifier to a 2 Ps OPO-Based SRS Microscope. *Opt Lett* **2017**, *42*, 523–526.

(191) Evans, C. L.; Xu, X.; Kesari, S.; Xie, X. S.; Wong, S. T. C.; Young, G. S. Chemically-Selective Imaging of Brain Structures with CARS Microscopy. *Opt. Express* **2007**, *15*, 12076–12087.

(192) Wang, H.; Fu, Y.; Zickmund, P.; Shi, R.; Cheng, J.-X. Coherent Anti-Stokes Raman Scattering Imaging of Axonal Myelin in Live Spinal Tissues. *Biophys. J.* **2005**, *89*, 581–591.

(193) Lei, T. C.; Ammar, D. A.; Masihzadeh, O.; Gibson, E. A.; Kahook, M. Y. Label-Free Imaging of Trabecular Meshwork Cells Using Coherent Anti-Stokes Raman Scattering (CARS) Microscopy. *Mol. Vis.* **2011**, *17*, 2628–2633.

(194) Kang, E.; Wang, H.; Kwon, I.; Robinson, J.; Park, K.; Cheng, J.-X. In Situ Visualization of Paclitaxel Distribution and Release by Coherent Anti-Stokes Raman Scattering Microscopy. *Anal. Chem.* **2006**, *78*, 8036–8043.

(195) Fussell, A.; Garbacik, E.; Offerhaus, H.; Kleinebudde, P.; Strachan, C. J. In Situ Dissolution Analysis Using Coherent Anti-Stokes Raman Scattering (CARS) and Hyperspectral CARS Microscopy. *Eur. J. Pharm. Biopharm*, 2013, *85*, 1141–1147.

(196) Jurna, M.; Windbergs, M.; Strachan, C. J.; Hartsuiker, L.; Otto, C.; Kleinebudde, P.; Herek, J. L.; Offerhaus, H. L. Coherent Anti-Stokes Raman Scattering Microscopy To Monitor Drug Dissolution in Different Oral Pharmaceutical Tablets. *J. Innov. Opt. Health Sci.* **2009**, *2*, 37–43.

(197) Fussell, A. L.; Mah, P. T.; Offerhaus, H.; Niemi, S.-M.; Salonen, J.; Santos, H. A.; Strachan, C. J. Coherent Anti-Stokes Raman Scattering Microscopy Driving the Future of Loaded Mesoporous Silica Imaging. *Acta Biomater.* **2014**, *10*, 4870–4877.

(198) Wanapun, D.; Kestur, U. S.; Taylor, L. S.; Simpson, G. J. Single Particle Nonlinear Optical Imaging of Trace Crystallinity. *Anal. Chem.* **2011**, *83*, 4745–4751.

(199) Alshaykh, M. S.; Liao, C.-S.; Sandoval, O. E.; Gitzinger, G.; Forget, N.; Leaird, D. E.; Cheng, J.-X.; Weiner, A. M. High-Speed Stimulated Hyperspectral Raman Imaging Using Rapid Acousto-Optic Delay Lines. *Opt. Lett.* **2017**, *42*, 1548.

(200) Czerwinski, L.; Nixdorf, J.; Florio, G. Di; Gilch, P. Broadband Stimulated Raman Microscopy with 0.1 Ms Pixel Acquisition Time. *Opt. Lett.* **2016**, *41*, 3021–3024.

(201) Cleff, C.; Gasecka, A.; Ferrand, P.; Rigneault, H.; Brasselet, S.; Duboisset, J. Direct Imaging of Molecular Symmetry by Coherent Anti-Stokes Raman Scattering. *Nat. Commun.* **2016**, *7*, 11562.

(202) Camp, C. H.; Lee, Y. J.; Cicerone, M. T. Quantitative, Comparable Coherent Anti-Stokes Raman Scattering (CARS) Spectroscopy: Correcting Errors in Phase Retrieval. *J. Raman Spectrosc.* **2016**, *47*, 408–415.

(203) Wang, P.; Liu, B.; Zhang, D.; Belew, M. Y.; Tissenbaum, H. A.; Cheng, J. X. Imaging Lipid Metabolism in Live Caenorhabditis Elegans Using Fingerprint Vibrations. *Angew. Chemie - Int. Ed.* **2014**, *53*, 11787–11792.

(204) Andreana, M.; Houle, M.-A.; Moffatt, D. J.; Ridsdale, A.; Buettner, E.; Légaré, F.; Stolow, A. Amplitude and Polarization Modulated Hyperspectral Stimulated Raman Scattering Microscopy. *Opt. Express* **2015**, *23*, 28119.

(205) Raghunathan, V.; Potma, E. O. Multiplicative and Subtractive Focal Volume Engineering in Coherent Raman Microscopy. *J. Opt. Soc. Am. A* **2010**, *27*, 2365–2374.

(206) Hajek, K. M.; Littleton, B.; Turk, D.; McIntyre, T. J.; Rubinsztein-Dunlop, H. A Method for Achieving Super-Resolved Widefield CARS Microscopy. *Opt. Express* **2010**, *18*, 19263–19272.

(207) Kim, H.; Bryant, G. W.; Stranick, S. J. Superresolution Four-Wave Mixing Microscopy. *Opt. Express* **2012**, *20*, 6042.

(208) Gong, L.; Wang, H. Suppression of Stimulated Raman Scattering by an Electromagnetically-Induced-Transparency-like Scheme and Its Application for Super-Resolution Microscopy. *Phys. Rev. A* **2015**, *92*, 023828-1-023828–8.

(209) Zhang, Y.; Zhen, Y.-R.; Neumann, O.; Day, J. K.; Nordlander, P.; Halas, N. J. Coherent Anti-Stokes Raman Scattering with Single-Molecule Sensitivity Using a Plasmonic Fano Resonance. *Nat. Commun.* **2014**, *5*, 1–7.

(210) Yampolsky, S.; Fishman, D. A.; Dey, S.; Hulkko, E.; Banik, M.; Potma, E. O.; Apkarian, V. A. Seeing a Single Molecule Vibrate through Time-Resolved Coherent Anti-Stokes Raman Scattering. *Nat. Photonics* **2014**, *8*, 650–656.

(211) Henderson, R.; Baldwin, J. M.; Ceska, T. A.; Zemlin, F.; Beckmann, E.; Downing, K. H. Model for the Structure of Bacteriorhodopsin Based on High-Resolution ElectronCryo-Microscopy. *J. Mol. Biol.* **1990**, *213*, 899–929.

(212) Kaneniwa, N.; Otsuka, M.; Hayashi, T. Physicochemical Characterization of Indomethacin Polymorphs and the Transformation Kinetics in Ethanol. *Chem. Pharm. Bull. (Tokyo).* **1985**, *33*, 3447–3455.

(213) Seemann, J.; Jokitalo, E. J.; Warren, G. The Role of the Tethering Proteins p115 and GM130 in Transport through the Golgi Apparatus in Vivo. *Mol. Biol. Cell* **2000**, *11*, 635–645.

(214) Belevich, I.; Joensuu, M.; Kumar, D.; Vihinen, H.; Jokitalo, E. Microscopy Image Browser: A Platform for Segmentation and Analysis of Multidimensional Datasets. *PLoS Biol.* **2016**, *14*, 1–13.

(215) Artursson, P.; Palm, K.; Luthman, K. Caco-2 Monolayers in Experimental and Theoretical Predictions of Drug Transport. *Adv. Drug Deliv. Rev.* **2001**, *46*, 27–43.

(216) Hubatsch, I.; Ragnarsson, E. G. E.; Artursson, P. Determination of Drug Permeability and Prediction of Drug Absorption in Caco-2 Monolayers. *Nat. Protoc.* **2007**, *2*, 2111–2119.

(217) Artursson, P. E. R. Epithelial Transport of Drugs in Cell Culture . I : A Model for Studying the Passive Diffusion of Drugs over Intestinal. *J. Pharm. Sci.* **1990**, *79*, 476–482.

(218) Donna, A. V. Variability in Caco-2 and MDCK Cell-Based Intestinal Permeability Assays. *J. Pharm. Sci.* **2008**, *97*, 712–725.

(219) Galli, R.; Uckermann, O.; Andresen, E. F.; Geiger, K. D.; Koch, E.; Schackert, G.; Steiner, G.; Kirsch, M. Intrinsic Indicator of Photodamage during Label-Free Multiphoton Microscopy of Cells and Tissues. *PLoS One* **2014**, *9*, e110295.

(220) Vogel, A.; Noack, J.; Hüttman, G.; Paltauf, G. Mechanisms of Femtosecond Laser

Nanosurgery of Cells and Tissues. *Appl. Phys. B* **2005**, *81*, 1015–1047.
(221) Thiam, A. R.; Farese, R. V; Walther, T. C. The Biophysics and Cell Biology of Lipid Droplets. *Nat. Rev. Mol. Cell Biol.* **2013**, *14*, 775–786.
(222) Murphy, D. The Biogenesis and Functions of Lipid Bodies in Animals, Plants and Microorganisms. *Prog. Lipid Res.* **2001**, *40*, 325–438.
(223) Martin, S.; Parton, R. G. Lipid Droplets: A Unified View of a Dynamic Organelle. *Nat. Rev. Mol. Cell Biol.* **2006**, *7*, 373–378.
(224) van Meer, G. Caveolin, Cholesterol, and Lipid Droplets? *J. Cell Biol.* **2001**, *152*, 29–34.
(225) Salo, V. T.; Belevich, I.; Li, S.; Karhinen, L.; Vihinen, H.; Vigouroux, C.; Magré, J.; Thiele, C.; Hölttä-Vuori, M.; Jokitalo, E.; *et al.* Seipin Regulates ER-Lipid Droplet Contacts and Cargo Delivery. *EMBO J.* **2016**, e201695170.
(226) Ducharme, N. A.; Bickel, P. E. Lipid Droplets in Lipogenesis and Lipolysis. *Endocrinology* **2008**, *149*, 942–949.
(227) Accioly, M. T.; Pacheco, P.; Maya-Monteiro, C. M.; Carrossini, N.; Robbs, B. K.; Oliveira, S. S.; Kaufmann, C.; Morgado-Diaz, J. a; Bozza, P. T.; Viola, J. P. B. Lipid Bodies Are Reservoirs of Cyclooxygenase-2 and Sites of Prostaglandin-E2 Synthesis in Colon Cancer Cells. *Cancer Res.* **2008**, *68*, 1732–1740.
(228) Scalfi-Happ, C.; Udart, M.; Hauser, C.; Rück, A. Investigation of Lipid Bodies in a Colon Carcinoma Cell Line by Confocal Raman Microscopy. *Med. Laser Appl.* **2011**, *26*, 152–157.
(229) Moreno, L.; Pearson, A. D. J. How Can Attrition Rates Be Reduced in Cancer Drug Discovery? *Expert Opin. Drug Discov.* **2013**, *8*, 363–368.
(230) Kola, I.; Landis, J. Can the Pharmaceutical Industry Reduce Attrition Rates? *Nat. Rev. Drug Discov.* **2004**, *3*, 1–5.
(231) Ocana, A.; Pandiella, A.; Siu, L. L.; Tannock, I. F. Preclinical Development of Molecular-Targeted Agents for Cancer. *Nat. Rev. Clin. Oncol.* **2010**, *8*, 200–209.
(232) Cheng, J.-X.; Xie, X. S. Vibrational Spectroscopic Imaging of Living Systems: An Emerging Platform for Biology and Medicine. *Science.* **2015**, *350*, aaa8870-1-aaa8870-9.
(233) Verma, S. P.; Wallach, D. F. H. Raman Spectra of Some Saturated, Unsaturated and Deuterated C18 Fatty Acids in the HCH-Deformation and CH-Stretching Regions. *Biochim. Biophys. Acta* **1977**, *486*, 217–227.
(234) Potcoava, M. C.; Futia, G. L.; Aughenbaugh, J.; Schlaepfer, I. R.; Gibson, E. A. Raman and Coherent Anti-Stokes Raman Scattering Microscopy Studies of Changes in Lipid Content and Composition in Hormone-Treated Breast and Prostate Cancer Cells. *J. Biomed. Opt.* **2014**, *19*, 111605.
(235) Di Napoli, C.; Pope, I.; Masia, F.; Watson, P.; Langbein, W.; Borri, P. Hyperspectral and Differential CARS Microscopy for Quantitative Chemical Imaging in Human Adipocytes. *Biomed. Opt. Express* **2014**, *5*, 1378–1390.
(236) Ayala, A. P.; Caetano, M. W. C.; Honorato, S. B.; Mendes Filho, J.; Siesler, H. W.; Faudone, S. N.; Cuffini, S. L.; Martins, F. T.; Da Silva, C. C. P.; Ellena, J. Conformational Polymorphism of the Antidiabetic Drug Chlorpropamide. *J. Raman Spectrosc.* **2012**, *43*, 263–272.
(237) Green, J. H. S. Vibrational Spectra of Benzene Derivatives-III. Anisole, Ethylbenzene, Phenetole Methyl Phenyl Sulphide and Ethyl Phenyl Sulphide. *Spectrochim. Acta* **1962**, *18*, 39–50.
(238) Saarinen, J.; Sözeri, E.; Fraser-Miller, S. J.; Peltonen, L.; Santos, H. A.; Isomäki, A.; Strachan, C. J. Insights into Caco-2 Cell Culture Structure Using Coherent Anti-Stokes Raman Scattering (CARS) Microscopy. *Int. J. Pharm.* **2017**, *523*, 270–280.
(239) Volkmer, A.; Cheng, J.-X.; Xie, X. S. Vibrational Imaging with High Sensitivity via Epidetected Coherent Anti-Stokes Raman Scattering Microscopy. *Phys. Rev. Lett.* **2001**, *87*, 023901-1-023901–023904.
(240) Lim, J. P.; Gleeson, P. A. Macropinocytosis: An Endocytic Pathway for Internalising Large Gulps. *Immunol. Cell Biol.* **2011**, *89*, 836–843.
(241) Huotari, J.; Helenius, A. Endosome Maturation. *EMBO J.* **2011**, *30*, 3481–3500.
(242) Aderem, A.; Underhill, D. M. Mechanisms of Phagocytosis in Macrophages. *Annu. Rev.*

Immunol. **1999**, *17*, 593–623.
(243) Taylor, L. S.; Zografi, G. Spectroscopic Characterization of Interactions between PVP and Indomethacin in Amorphous Molecular Dispersions. *Pharm. Res* 1997, *14*, 1691–1698.
(244) Surwase, S. A.; Boetker, J. P.; Saville, D.; Boyd, B. J.; Gordon, K. C.; Peltonen, L.; Strachan, C. J. Indomethacin: New Polymorphs of an Old Drug. *Mol. Pharm.* **2013**, *10*, 4472–4480.
(245) Zhang, L.; Henson, M. J.; Sekulic, S. S. Multivariate Data Analysis for Raman Imaging of a Model Pharmaceutical Tablet. *Anal. Chim. Acta* **2005**, *545*, 262–278.
(246) Priemel, P. A.; Grohganz, H.; Gordon, K. C.; Rades, T.; Strachan, C. J. The Impact of Surface- and Nano-Crystallisation on the Detected Amorphous Content and the Dissolution Behaviour of Amorphous Indomethacin. *Eur. J. Pharm. Biopharm.* **2012**, *82*, 187–193.
(247) Andronis, V.; Yoshioka, M.; Zografi, G. Effects of Sorbed Water on the Crystallization of Indomethacin from the Amorphous State. *J. Pharm. Sci.* **1997**, *86*, 346–357.